UNIVERSITY OF MANITOBA

THE EFFECT OF PRIOR DEFORMATION ON THE AGING CHARACTERISTICS OF A CO-NI BASE SUPERALLOY

BY

G. MITCHELL OMICHINSKI

A THESIS SUBMITTED TO THE FACULTY OF GRADUATE STUDIES
IN PARTIAL FULFILLMENT OF THE REQUIREMENTS FOR
THE DEGREE OF MASTER OF SCIENCE OF MECHANICAL ENGINEERING

DEPARTMENT OF MECHANICAL ENGINEERING

WINNIPEG, MANITOBA

FEBRUARY, 1977.

"THE EFFECT OF PRIOR DEFORMATION ON THE AGING CHARACTERISTICS OF A CO-NI BASE SUPERALLOY"

by

G. MITCHELL OMICHINSKI

A dissertation submitted to the Faculty of Graduate Studies of the University of Manitoba in partial fulfillment of the requirements of the degree of

MASTER OF SCIENCE

ABSTRACT

The effects of room temperature prior deformation on the precipitation of a Co-Ni based alloy (40% Co, 38% Ni, 17% Cr, 5% Nb) were investigated. The mechanical properties and microstructures for light (5%), moderate (30%), and heavy (60%) deformations were compared with the solution treated condition. Aging was carried out at 800° C for times up to 150 hours. Cold work results in deformation twinning of the matrix. The main precipitate phase on aging is plate-shaped Ni_3Nb orthorhombic. In general, deformation accelerates this precipitation with matrix-twin interfaces acting as nucleation sites. Prior heavy deformation and aging results in partial recrystallization of the matrix. The new recrystallizing grain boundaries act as nucleation sites for discontinuous precipitation of Ni_3Nb orthorhombic in the shape of distorted spheres. The space group symmetry for both particle shapes was identified as Pma2. Improvements in tensile properties on aging the solution treated condition were more significant than those observed for deformed-aged conditions.

ACKNOWLEDGEMENTS

I would like to express my thanks to my supervisor, Dr. M. C. Chaturvedi for his support and avice. Also, I would like to thank Dr. Nabil Ibrahim and Dr. David Tseng for their helpful discussions. Finally, I am eternally grateful to my parents.

TABLE OF CONTENTS

Page

LIST OF FIGURES

CHAPTER 1 INTRODUCTION

Superalloy is the term used to describe an alloy maintaining high strength and corrosion resistance in high temperature application. These alloys have a base element of nickel, chromium, cobalt, iron, or iron-nickel. Since the first patented use of Co-Cr (20-33%) and Co-Cr type alloys by G. Tamman[1] in 1909, Co-base alloys have become increasingly important in superalloy application. The property characteristics that make Co-base alloys attractive include excellent thermal fatigue resistance, high strength above 900°F, relatively high melting point, and good resistance to hot environment of lead and sulphur compounds.[2]

The major alloying constituent of Co-base alloys has been Ni which increases the strength and stabilizes an FCC matrix. Pure Cobalt is allotropic in nature, existing as an FCC structure at high temperature and close-packed hexagonal at room temperature.[3] The transformation is martensitic with an Ms temperature of 417°C. Alloy addition of 30% Ni stabilizes the FCC structure by lowering the Ms temperature to below room temperature.[4] Corrosion resistance is provided by addition of chromium, usually in amounts of 15-22%.

Much work[5,6,7,8,9,10,11] has been done in the past decade in precipitation strengthening these alloys with smaller additions (1-10%) of such elements as Ti, Mo, Al, and Nb. One such alloy developed at the University of Manitoba has the nominal composition of 40% Co, 38% Ni, 17% Co, 5% Nb. The precipitation and aging kinetics of this system on the solution treated condition has already been studied.[5] However, the effect of prior

deformation on aging was not considered. It was the intent of this thesis to study these effects on the mechanical properties and microstructure. Such a study is important if thermo-mechanical treatments are considered as a way of improving the properties of this alloy. It includes the three phenomena of plastic deformation, precipitation, recrystallization, and their mutual influence on each other.

The specific approach taken was to study the effects of light (5%), moderate (30%), and heavy (60%) prior deformations on the microstructure and mechanical properties in the pre and post aged conditions. X-ray and electron microscopy techniques were employed to study precipitation and recrystallization behavior, while Vickers pyramid hardness and tensile testing was used to study changes in mechanical properties.

CHAPTER 2 LITERATURE SURVEY

2.1 PLASTIC DEFORMATION

2.1.1 Dislocations and Mechanical Properties

Plastic deformation of a metal at a temperature which is low relative to its melting point (< 0.5 Tm) is called cold working. The energy expended during deformation mostly appears as heat, but a small fraction is stored in the metal in the form of lattice defects (Fig. 1). These are point defects such as vacancies and interstitial atoms, and line defects called dislocations. The majority of the strain energy is stored in the latter. Dislocation densities are expressed in total length of dislocation line per unit volume of material. The density increases progressively with cold work from an initial well annealed value of $10^{6}cm^{-2}$ to 10^{11} - $10^{13}cm^{-2}$ with plastic strains of 100%.

It has long been established[12,13] that increasing dislocation density is accompanied by an increasing strength and hardness of the metal and a decreasing ductility. These property changes are due to work-hardening mechanisms involving dislocation generation, multiplication, and mutual interaction.

High strength materials can also be produced theoretically, by reducing the dislocation density to zero, in which case all materials would have the theoretical strength ≈ G/30.[14] However this is only virtually obtainable in nearly perfect single crystals called whiskers.[15] In real materials, unavoidable dislocations are introduced during solidification, during thermal contraction on cooling, and as a result of phase transformation.

Dislocations are actually fortunate, for they provide the property of ductility needed for the fabrication processes of engineering materials.

2.1.2 Dislocation Arrangement in the Annealed State

In the annealed state, metal crystals typically have a dislocation density of about $10^6 cm^{-2}$. The arrangement of these dislocations has been revealed to be of two basic types: a) three dimensional networks called the Frank nets[16] (Fig. 2); b) planar dislocation networks called tilt and twist boundaries[17,18] (Fig. 3). From elementary dislocation theory, it is known that a dislocation cannot end in a crystal. It must end at the surface of the crystal, form a closed loop, or branch into other dislocations. The latter possibility leads to the formation of nodes, which are points where three or more dislocations meet on the condition that the sum of their Burgers vectors is zero. Such dislocations networks form Frank nets which are believed to have high thermal stability.

The formation of planar dislocation networks arises out of the presence of an excess of dislocations of one sign. Edge dislocations give rise to formation of pure tilt boundaries, and screw dislocations form twist boundaries. Both climb and cross slip are necessary for dislocations to arrange themselves in such configurations which are called low angle boundaries. Regions of the crystal separated by such boundaries differ in orientation by less than 5°.

The driving force for the formation of low angle boundaries is the reduction of strain energy. Long range internal stresses of the dislocations are eliminated by their mutual interaction. However, short range stress fields always remain.

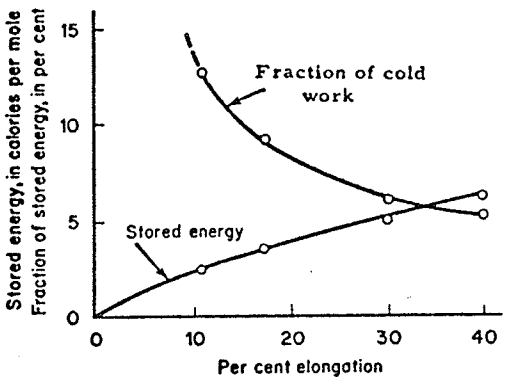

Fig. 1 Stored energy and fraction to total deformation energy stored with elongation of high purity copper, [118].

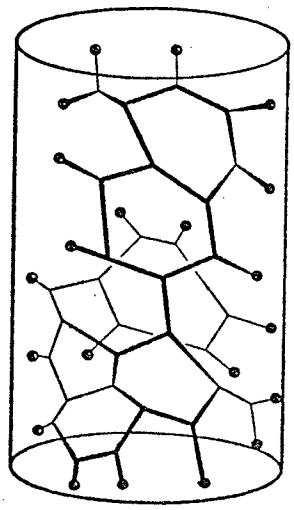

Fig. 2 Arrangement of dislocation in a well annealed crystal; the Frank net, [119].

Solute atoms in a solvent metal manifest their effect on dislocation arrangements through the stacking fault energy of the metal. The addition of solute atoms can lower the stacking fault energy (SFE), resulting in a tendency for a dislocation to dissociate into partial dislocations with a faulted region in between. The strain energy of a dislocation is proportional to b^2 through the general strain energy relation of:

$$E = \alpha G b^2$$

where $\alpha \simeq 0.5 - 1.0$, and G is the shear modulas. According to Frank's rule, if b_1, b_2, and b_3 are permissible Burgers vectors in a particular crystal lattice, a dislocation with the Burgers vectors b_3 will split up into the dislocation b_1 and b_2 if $b_3^2 < b_1^2 + b_2^2$. In FCC metals and alloys, such dissociations can take place on the slip plane {111} and the resultant reaction is described as:

$$a/2\ [110] \rightarrow a/6\ [211] + a/6\ [12\bar{1}]$$

where 'a' is the lattice parameter.

The partial dislocations have components of the same sign and will repel each other, forming a ribbon of stacking fault between them, which has a characteristic energy called the stacking fault energy (ergs/cm^2). This energy provides a force tending to pull the dislocation together. Metals of high stacking fault energy will have whole dislocations, while those of relatively low SFE (< 30 ergs/cm^2) tend to have extended dislocations.

The geometry of the Frank net associated with metals of low SFE has been described by Whelan[20] and is shown in Figure 4. The partial dislocations are constricted at nodal junctions while extended along their free length. Partial dislocations by themselves cannot cross slip or climb. They must be constricted to form a whole dislocation of some finite length before these mechanisms of dislocation movement can operate. Therefore,

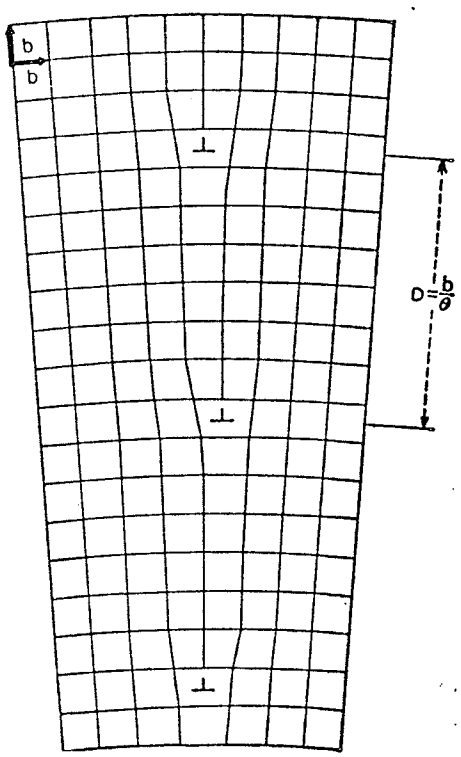

Fig. 3 Subgrain tilt boundary formed by edge dislocations, [120].

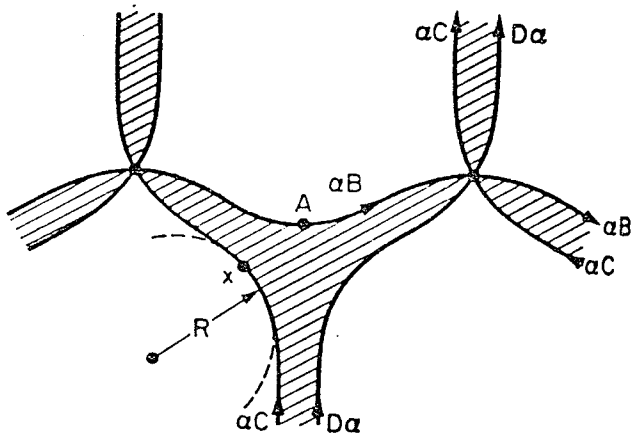

Fig. 4 Geometry of node formation in FCC materials of low SFE. Shaded areas are stacking fault, [25].

lowering the stacking fault energy by solute atoms hinders the formation of low angle boundaries. This is an observation made in many alloy systems (Cu-Al)[21,22], (Cu-Zn, Al, Ge, Sn, or Si)[23], (Ag- Zn, or Al and Ni-Co).[24]

2.1.3 Dislocation Arrangement in Polycrystals Deformed at Room Temperature

The plastic deformation of annealed metals and alloys causes an increase in flow stress, and the phenomenon is called strain hardening. It is the result of rapid dislocation multiplication and their interaction with one another and with obstacles, such as precipitates, in the slip planes. The dislocation arrangements are generally similar between materials of different crystal structures, and depend mainly on one material variable, the SFE.[25]

In materials that have SFE > 30 ergs/cm^2, the process of cross slip and climb are relatively easy. Initially, up to strains of approximately 10%, multiplication mechanisms result in formation of tangles of dislocations which eventually link up to form well defined cell structure. The cell interiors are relatively free from dislocations and the cell walls tend to lie along certain crystallographic planes.[26] The cell walls are called tangles because of their jagged, twisted, and irregular array nature. Further deformation increases the density of dislocation and sharpness of the cell wall, resulting in an irregular misorientation between the cells of up to 5°.[27] There is little tendency towards refinement of the cell size with greater deformation. However cold rolling tends to elongate the cells in the direction of rolling, often exhibiting a preferred orientation.

When the SFE is less than 30 ergs/cm^2, the process of extended dislocation changes the appearance of dislocation arrangement. There is little

tendency to form cellular structure even at high strains. Cross slip is inhibited, forcing dislocations to remain on their slip planes, resulting in pile ups at obstacles such as grain boundaries. At low strain, the prominent features are bands of extended dislocations (stacking faults) and planar pile up arrays. At high strain there is some tendency to form a very ragged tangled cellular structure.[26] When solute atoms lower the SFE of a metal, the extended dislocation structure is promoted. Different alloys of the same SFE have similar dislocation arrangements, independent of the species of alloying elements. This has been summarized for Cu and Ag alloy by Swann[26] in Figure 5.

2.1.4 Deformation Twinning

2.1.4.1 General Characteristics

Twinning and slip are modes of plastic deformation and both result in a net shear of the lattice. The basic difference in lattice translation between the two is illustrated in Figure 6. In slip, deformation occurs on relatively few discreet lattice planes for a given volume. It has a two dimensional character, and within a volume the majority of atoms remain fixed with respect to each other. In deformation twinning, the total shear is uniformly distributed throughout the volume by a co-operative movement of atoms in which individual atoms move a fraction of the interatomic spacing relative to each other. The resulting lattice of twin volume is a mirror image of the parent lattice across the plane separating the two. This symmetry plane, usually of low indices is called the twinning plane and is illustrated in Figure 7.

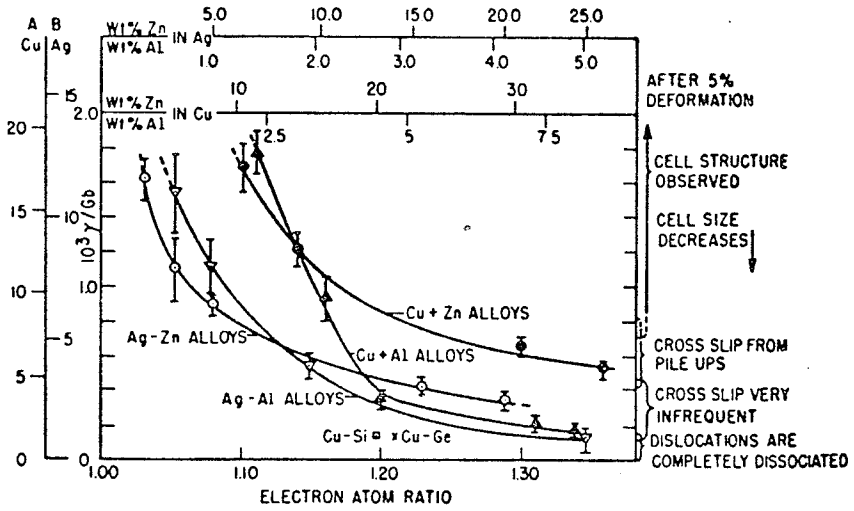

Fig. 5 The approximate stacking fault energies of copper and silver alloys are given by columns A and B. The relationship with dislocation distribution is described in the column on the right, [26].

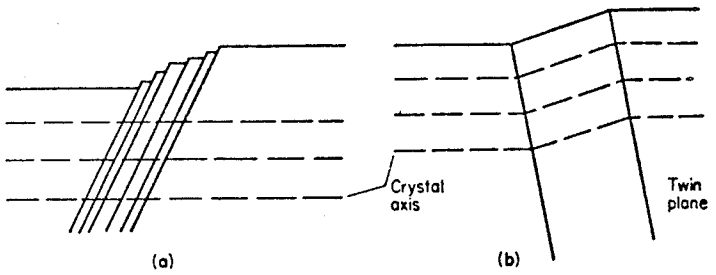

Fig. 6 The difference between (a) slip and (b) twinning, [121].

The process of twinning is frequently a catastrophic event resulting in a sharp load drop and serrated yielding in a tension test. The large energy release can sometimes result in an audible sound such as the "cry" of tin in deformation. Twinning is an important mode of deformation in metals where possible slip systems are limited such as BCC and CPH crystal structures. If a crystal is in an unfavourable orientation for slip, twinning may occur to align the possible slip systems more favourably.

In FCC metals, which have many slip systems, twinning is not considered a dominant mode of deformation. It occurs only under a highly resolved shear stress of a work hardened state, which can be obtained at low temperatures of deformation.[28] It also can be found to occur more readily in metals and alloys which possess a low SFE, in which case slip would be inhibited. Venables[29] has plotted results for Cu alloys which demonstrate a tendency for a lowering of twinning stress with decreasing SFE (Fig. 8). He argues that a transition occurs in twinning between high and low SFE materials, the latter twin profusely on a fine scale without noticable load drop. He contends that twin nucleation is easier for low stacking fault materials, where propagation of twins through forest dislocations is difficult. With high SFE, twin nucleation is the critical step, giving rise to the catastrophic load drop and Lüders band growth in a tension test.

Also in this review[29], Venables concludes that there is little definite orientation or temperature variation of the twin stress in FCC metals. Composition of the alloy is thought to be important because of variation in SFE.

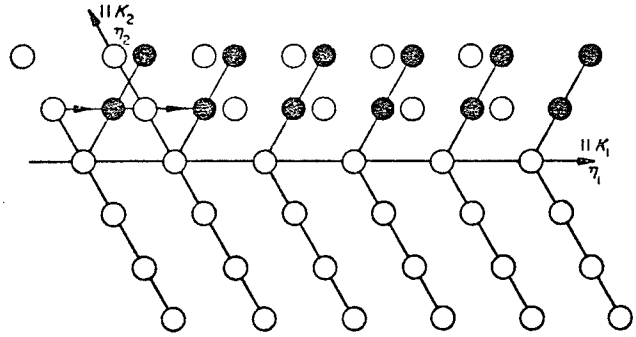

Fig. 7 A twinning transformation, [121].

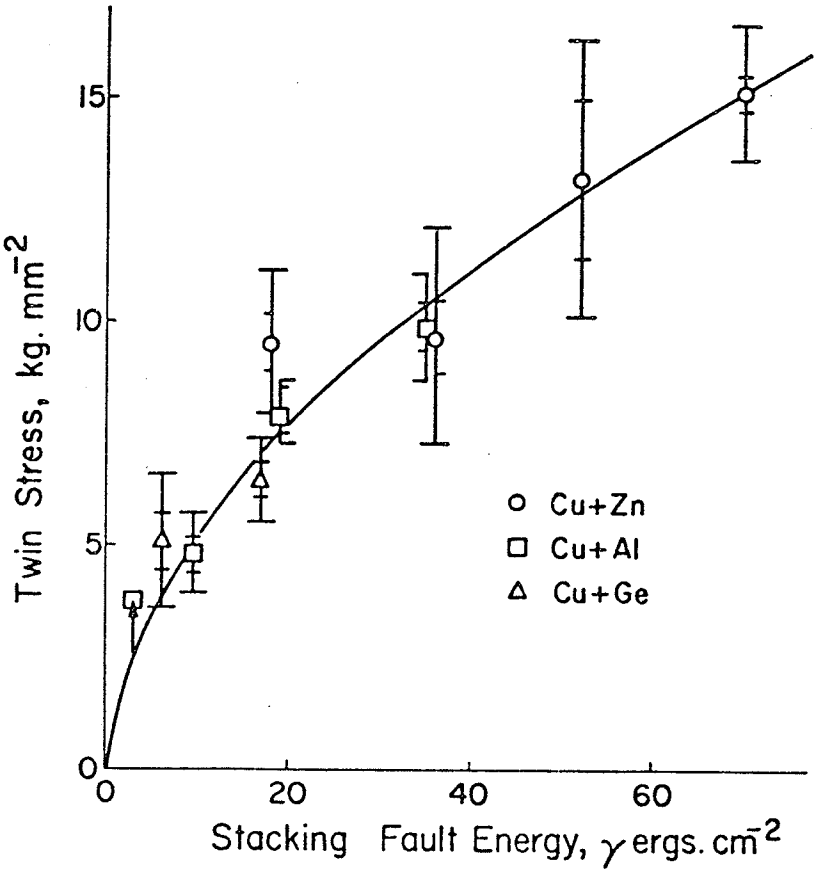

Fig. 8 Twin stress versus stacking fault energy for copper base alloys, [29].

2.1.4.2 Twinning Mechanism for FCC Metals

The characteristic stacking sequence of (111) planes in FCC structure is:

A B C A B C A B C

The atomic arrangement of the atoms in a (111) plane is shown in Figure 9 with the atomic positions of the planes immediately above and below indicated. The stacking sequence of close-packed planes encountering a twin boundary is given by:

A B C A B A C B A

As with slip, deformation twinning takes place at stresses far below the theoretical shear strength for a perfect crystal. It follows that twinning must occur by a continuous growth of the twinned material on an atomic scale and not by the simultaneous movement of all atoms involved. Slip occurs on {111} planes in <110> directions and is the result of numerous whole dislocations passing over few slip planes. The amount of shear dislplacement for one dislocation and shear direction is illustrated by vector b_1 of Figure 9. Twinning, on the other hand, is the result of homogeneous shear and is equivalent to the passage of partial dislocation on successive planes. The shear displacement and direction on each plane is represented by the vector b_1 or b_2 in Figure 9. Dislocation models to account for this shear in deformation twinning can do so in one of two ways.[30] These are the initiation of identical partial dislocations in every lattice plane, as described by the homogeneous twin nucleation model, or the passage of a simple partial dislocation moving from one plane to the next, as described by the pole mechanism.

The homogeneous nucleation of stable twin nuclei, although no application of it to FCC metals could be found, is outlined here for the sake of completeness. It was first considered by Orowan,[31] who concluded that twin nuclei would arise at stress concentrators which could increase the locally applied stress to the theoretical twinning stress. Studies on Zinc[32] concluded that the piling up of slip dislocations against a suitable obstacle was a sufficient stress concentrator. Acceptance of this model requires that one accepts the creation of partial dislocations out of a perfect lattice. A stable nucleus could propagate by their motion, but increasing thickness of the twin would require repetitive nucleation of twinning dislocations at the twin-matrix interface. Experimental verification of this model has been found in several studies.[33,34,35]

The pole mechanism of deformation twinning can be applied to any crystal structure and carries with it the concepts of SFE, partial dislocation, and dislocation interaction. For FCC structures, stacking fault areas are bounded by Shockley a/6 <211> type partials. These areas can be regarded as a layer of twinned material, which, depending on the nature of the fault, has the following sequence:

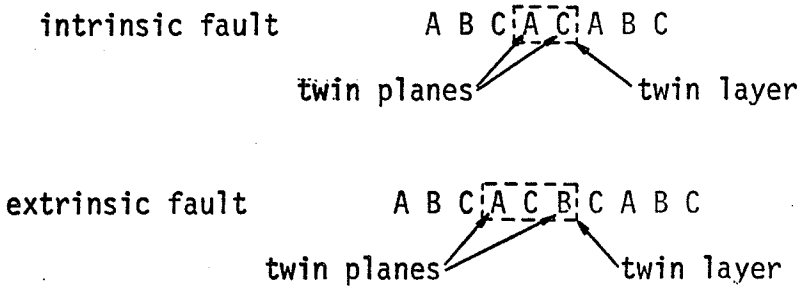

The pole mechanism model requires a partial (twinning) dislocation to rotate about a pole dislocation whose screw component is perpendicular to the twin plane and the Burgers vector of which is equal to the spacing of these planes ($a/3 < 111 >$). In this way, a sweeping twin dislocation can generate a stacking fault on every plane producing a final twin structure of finite thickness. By such a mechanism, a twin can be produced very quickly in the absence of diffusion and without the need of a separate dislocation source on every successive plane.

The first detailed mechanism using this concept, as applied to FCC metals, was given by Cottrell and Bilby.[36] However, they considered the twin dislocation to go no further than a single revolution forming a single layer of twin, which explained the non-observation of the thick twins at the time. With the unambiguous demonstration of deformation twins in FCC metals by Blewitt et al[28], Venables[29] described a modified version of the original model, maintaining the pole concept. A detailed description of this mechanism is not presented here but is obtainable from reference. The net result is a lens shaped twin whose incoherent boundary is an array of piled up partial dislocations (Fig. 10). Growth of the twin results from a glissile movement of the dislocation array.

2.2 PRECIPITATION HARDENING

2.2.1 General Concepts

Strengthening of metal alloys by precipitation hardening has been dealt with in many publications[37,38,39,40] and the principles governing the phenomena are now quite well established. The main criteria is that there be a decreasing solid solubility of a second phase with decreasing temperature (Fig. 11). The basic steps are to form a solid solution at

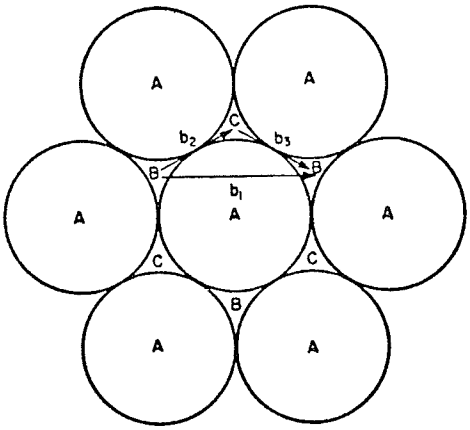

Fig. 9 Slip in FCC crystals, [122].

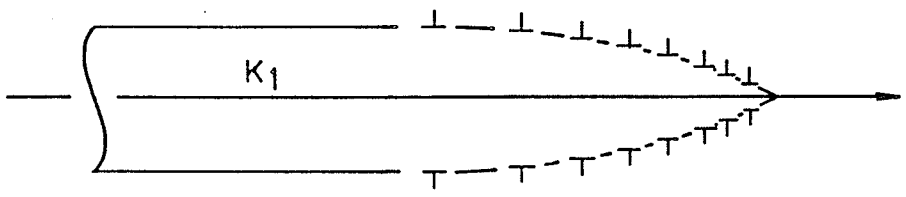

Fig. 10 Twinning dislocation arrangement at twin interface, [106].

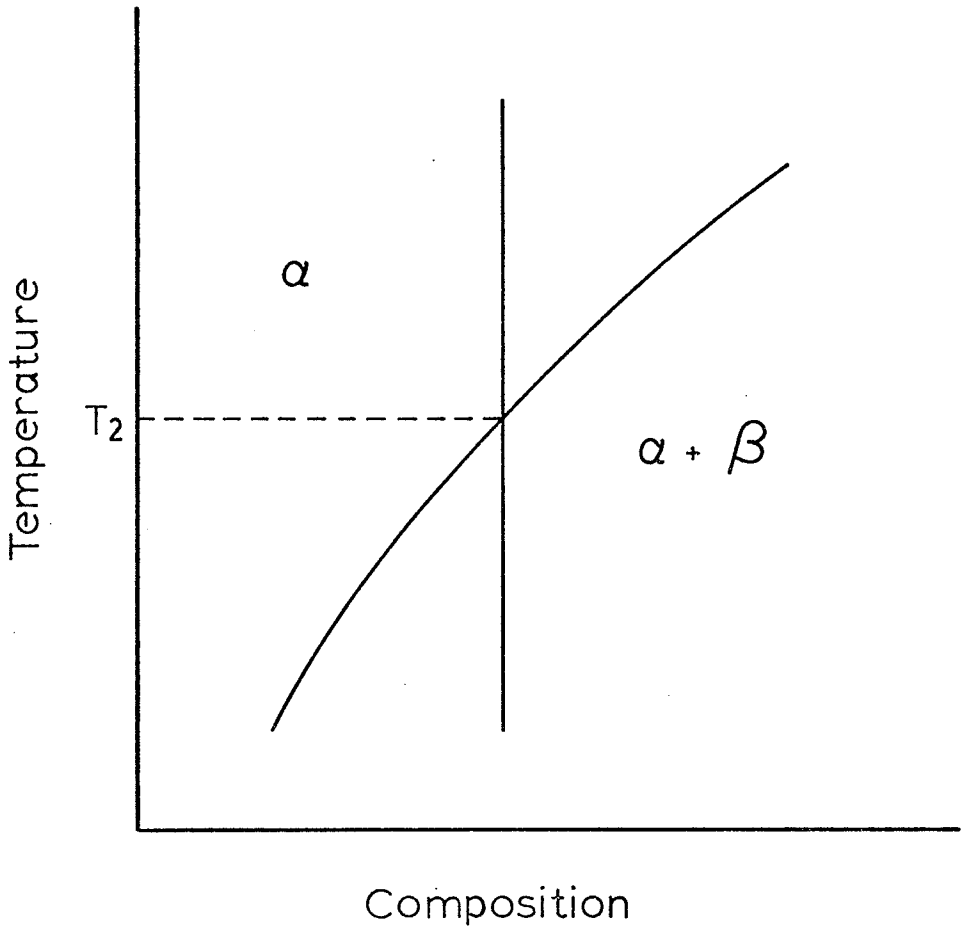

Fig. 11 Decreasing solubility of α and β with decreasing temperature.

some high temperature, quench to form a supersaturated solid solution, then by suitable heat treatment or aging, cause the excess solute to precipitate out as a second phase. Consequent interaction of glide dislocations with these precipitates upon deformation will usually lead to strengthening of the material. The extent of this strengthening is strongly dependent on the precipitate shape, nature (hard or soft), size, and nature of interface with the matrix.

The latter property is used to classify the various stages of precipitate formation. A coherent interface is characterized by continuity of atomic planes through the interface (Fig. 12). This only arises when the atomic spacing of the matrix and particle crystal structures are closely similar and the misfit between the two can be accomodated by elastic strains, usually of the matrix. These strains are termed coherency strains and are dependent on the degree of misfit.

If the surface area of a coherent interface with a certain misfit becomes large, the total strain energy may be reduced by the introduction of structural dislocations lying in the interface. The area between the dislocations remains fully coherent and the interface as a whole is described as quasi-coherent (Fig. 12b). In an incoherent interface, the structural dislocations have become so closely spaced together that they cannot be considered separate defects (Fig. 12c).

The aging of a supersaturated solid solution usually involves a decomposition in several stages or metaphases. A typical sequence is the following: supersaturated solution → zones → intermediate precipitate → equilibrium precipitate. The formation of zones involves the clustering of solute atoms into small aggregates. These are completely

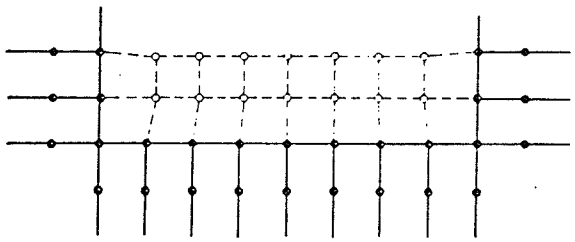

(a)

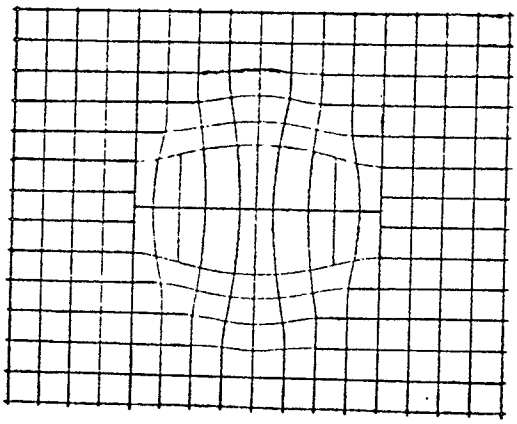

(b)

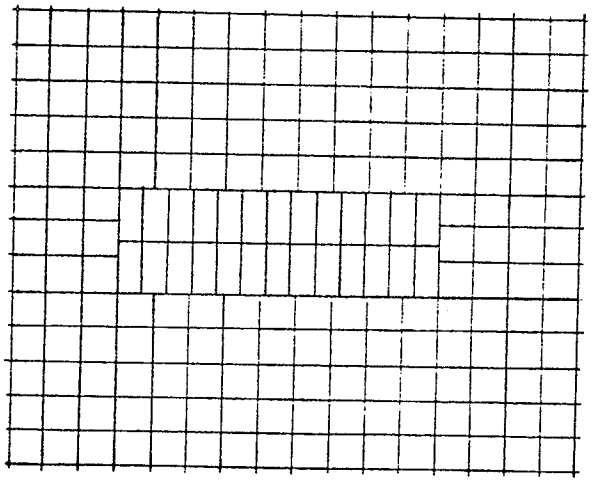

(c)

Fig. 12 Types of interfaces between two crystal structures (a) coherent, (b) quasi-coherent, (c) incoherent, [40] .

coherent with the matrix and as they form, the alloy usually becomes harder due to coherency strains. If there is no atomic misfit, the shape of the zones are spherical. Otherwise, they may take the form of plates, rods, or cubes.

The intermediate precipitate may or may not involve a partial loss in coherency. A fully coherent precipitate is one in which all interfaces are coherent and the lattice structure of matrix and particle are identical, if allowance is made for the difference in atomic spacing.[41] A partially coherent precipitate has at least one interface with the matrix coherent. Both types always have a particular orientational relationship with the matrix. The shape is governed by the relative values of elastic constants, the degree of misfit, and the anisotropy of surface energies. If the strain energy associated with the precipitate is small, the shape is dictated by the minimum surface area to volume ratio. Generally, spheres are formed where the atomic misfit is 3%, and discs when the misfit is 5%.[42]

The equilibrium precipitate is usually incoherent; that is, none of its interfaces with the matrix are coherent. The shape is governed only by the elastic strain energy of the matrix. Nabarro [43] showed that the minimum energy shape for a highly strained precipitate (hard matrix) is a disc. This has a high surface area volume ratio, and is unfavourable from the point of view of surface energy. In a softer matrix, the actual shape is an oblate spheroid, a compromise between the two opposing factors.

To account for the different stages of precipitation, it is necessary to consider the driving force for the decomposition of a supersaturated alloy; that is, the negative free energy change. Figure 11 is the phase diagram of a typical precipitation hardenable alloy. The precipitation of β phase at temperature T_2 constitutes a phase change. Gibbs[44] showed that two types of phase change exist: (a) spinodal (b) nucleation and growth. The distinction between these types of phase transformations is shown in Figure 13. Figure 13a is a hypothetical binary equilibrium diagram in which two solid solutions of identical lattice structure are formed on cooling. Figure 13b is the free energy composition curve for temperature T_1. For composition pure A to p and from q to pure B, the lowest free energy state is that of a single solid solution. For composition between p and q, the free energy is minimized by the co-existence of two phases p and q. These are determined by the common tangent touching the free energy curve. The interaction of this tangent with a composition line within p and q represents the lowest free energy state of the composition.

Consider an alloy of composition c_1, with initial free energy F_1, decomposing into a mixture of p and q. If an early stage of the transformation is represented by p' and q', the average free energy F_1' is lower than F_1. This process can clearly continue with a progressive fall in average free energy until the phases p and q exist. Such transformation in which there is a continuous fall in free energy is called spinodal transformation.

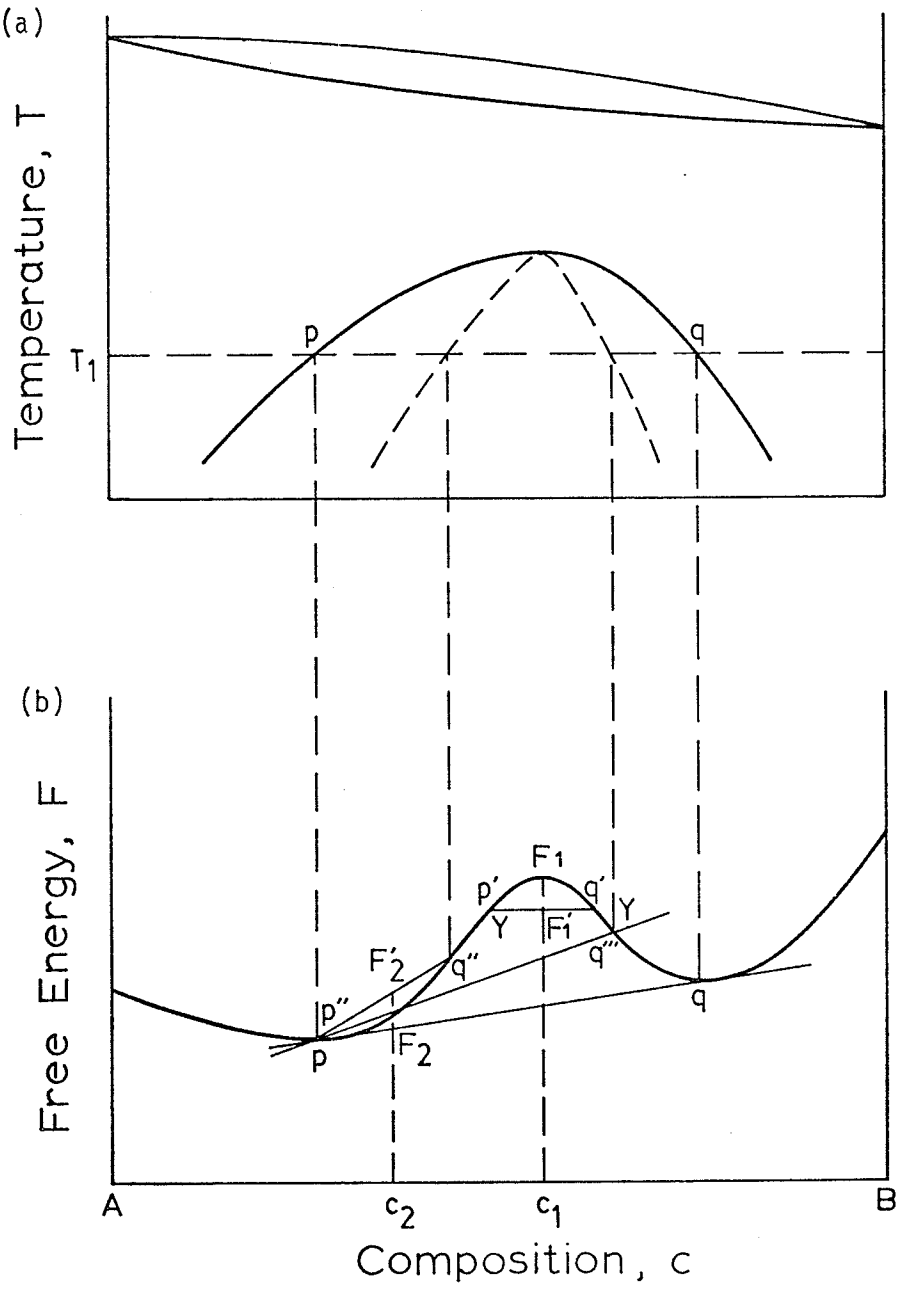

Fig. 13 (a) Hypothetical binary equilibrium diagram

(b) Free energy composition curve for temperature T_1, for elements A & B, [40].

If the alloy composition is c_2, with free energy F_2, a similar decomposition to p and q is favourable. However, an early stage in the transformation might be p" and q", with average free energy F_2'. This is higher than F_2 and represents a free energy barrier (activation energy) that must be overcome before transformation can proceed. Compositional fluctuations in the material must reach the value of q''' before the free energy can be minimized. This effect accounts for the conventional nucleation and growth behavior encountered in most precipitating systems.

The points of inflection (Y) in the free energy composition curve divide the ranges in which the two types of phase transformations occur. The locus of these points on the phase diagram (Fig. 13a) is shown by a solid line. Between the points, spinodal decomposition occurs, while areas outside the points represent nucleation and growth transformation.

If there are a number of different ways for a metastable alloy to transform, the precipitation path followed is one of minimum activation energy, rather than maximum change of free energy. The formation of the equilibrium precipitate represents the greatest change in free energy. However, the activation energy to form a metastable phase might be less. If the work to form a β nucleus is W and that of β' is W', the condition for β' to form in preference to β is $W' < W$ (Fig. 14). Alloy systems in which such transformations are likely are those in which the stable precipitate is very unlike the matrix in structure and composition so that any form of coherency is not possible.[45]

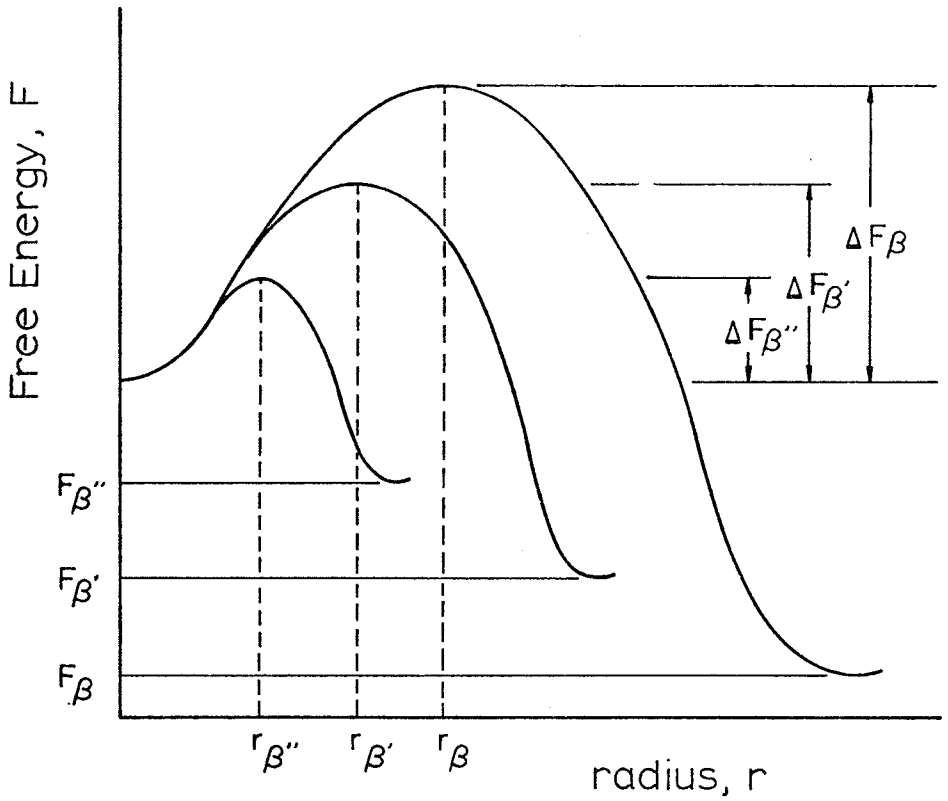

(a) Free energy vs radius of precipitate

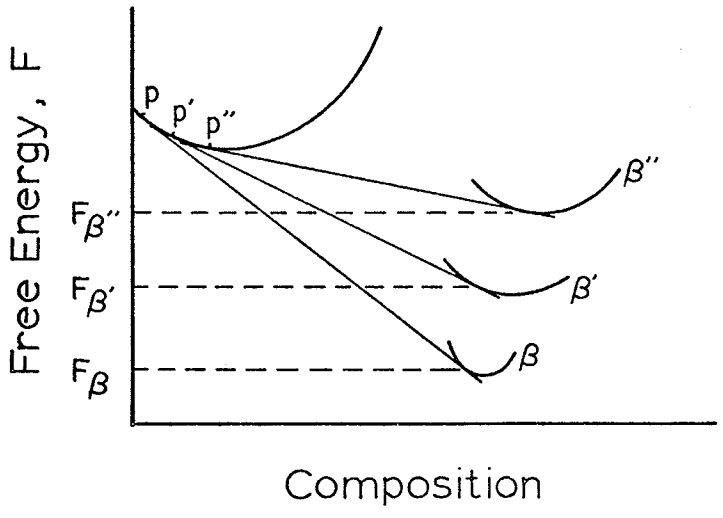

(b) Free energy vs composition

Fig. 14 Activation energies of formations $\Delta F_{\beta''}$/ $\Delta F_{\beta'}$/ ΔF_β of metastable precipitates β" and β' and equilibrium precipitate β respectively, [40].

The activation energy in the formation of a nucleus is the summation of three energy changes:

$$\Delta F = -\Delta V + \Delta S + \Delta E$$

where ΔV is the volume free energy change, ΔS is the surface free energy change, and ΔE is the strain energy associated with precipitate formation. From Figure 14a, it is implicit that the volume free energy change of the equilibrium coherent precipitate (ΔV_β) will be greater than that of the coherent precipitate ($\Delta V_\beta'$); that is, ($r_\beta > r_\beta'$, where r is the radius of nucleus). However, nucleation of a coherent precipitate will involve a smaller ΔS term. Provided this more than compensates for the smaller ΔV term and larger ΔE term, $\Delta F_\beta'$ will be less than ΔF_β and a metastable coherent phase will result. Some general rules involving the formation of metastable phase are as follows:[46]

(1) As a supersaturation of the alloy decreases, the number of intermediate stages decreases.

(2) The formation of a more stable product results in the resolution of less stable phases formed in earlier stages or insitu transformation of unstable phase to a more stable phase.

Nucleation that occurs completely at random in a system is termed homogeneous. Every small volume element of the supersaturated state must be structurally, chemically, and energetically identical for homogeneous nucleation. In real alloy systems imperfections such as surfaces, grain boundaries, dislocations, stacking faults, and impurities exist and are energetically favourable sites for nucleation. Such preferred nucleation is termed inhomogeneous. Complete homogeneous nucleation normally does not occur in practice but the concepts are the same in each.

The classical theory of nucleation was originated by Volmers and Weber[47] and Becker and Doring[48], and the basic concept is as follows. The formation of a nucleus, as mentioned above, involves the summation of three energy terms. The negative change in volume free energy (ΔV) tends to induce the transformation, while the increase in surface energy (ΔS) and elastic strain energy (ΔE) tend to oppose it. Initially the latter two terms dominate such that:

$$\Delta V < \Delta S + \Delta E$$

until a critical radius of r_c is attained (Fig. 15). Aggregates of solute atoms less than this size are termed embryos and are metastable, decomposing back into solid solution. Once an embryo reaches the critical size by statistical fluctuation, it is called a nucleus. Beyond this point:

$$\Delta V > \Delta S + \Delta E$$

there is a fall in free energy and transformation proceeds by growth. The greater the supersaturation by lowering the aging temperature (Fig. 15) or increasing the solute content, the smaller the critical radius. This results in a finer precipitate dispersion and size.

2.2.2 Effects of Prestrain in Precipitation Characteristics

The formation of zones in a precipitation hardenable alloy faces no effective nucleation barrier, and the process takes place by competitive growth rate.[49] This rate is dependent on the vacancy concentration and the activation energy for the migration of a vacancy solute atom pair. Rapidly quenched specimens contain an excess concentration of vacancies which decays away on aging. Cold work prior to aging increases the vacancy concentration but also introduces dislocations which act as vacancy sinks,

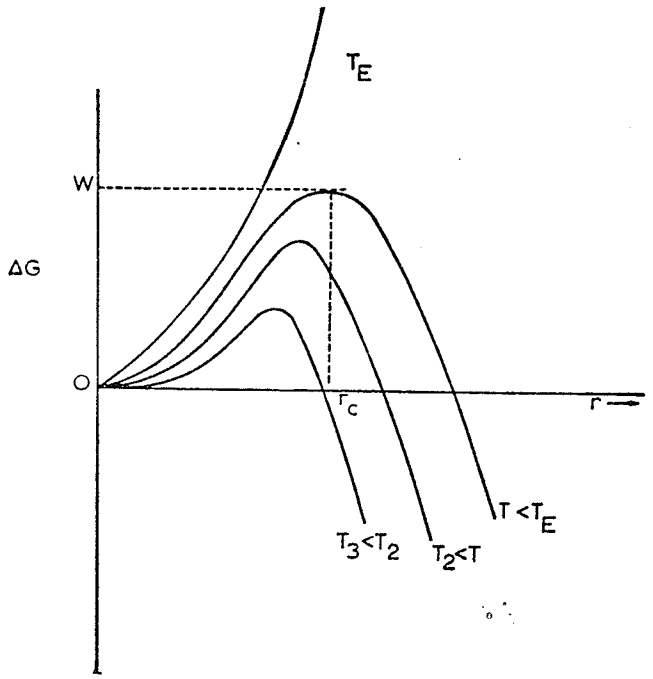

Fig. 15 The free energy of formation of spherical embryos as a function of radius for a series of temperatures, [123].

resulting in a net increase in the rate of vacancy decay on aging. This has no effect on the initial rate of aging, but reduces the final zone size. Slowly cooled specimens frequently have only temporary vacancy sinks such as vacancy clusters. In this case, cold work redistributes the vacancies, increasing the initial aging rate. However, the increased dislocation density, acting as sinks, imposes a limit on zone size. Cold work can only effect the kinetics of zone formation, with no evidence that dislocations act as preferred sites for nucleation of zones.

Nucleation of the intermediate precipitate, however, is increased by cold work prior to aging. This has been observed in many alloy systems.[50,51,52,53,54] Dislocations and dislocation debris (prismatic loops) produced by cold work may serve as nucleation sites or channels for more rapid diffusion of the elements participating in the aging reaction. The thermodynamic relationships involved with precipitation at dislocations was first described by Cahn.[55] In general, the activation energy for precipitation is smaller at a dislocation since the lattice misfit of the precipitate can be partly or wholly accomodated by the dislocation line. It has been recognized that a given dislocation does not offer an equal nucleation site for each of the Widmanstatten habits of a particular coherent precipitate phase. As an empirical rule, it has been found that the habits that nucleate are those in which the principal misfit of the phase is more nearly parallel to the Burgers vector of the dislocation.[56] Increasing the dislocation density by cold work increases the rate of heterogeneous nucleation and results in a finer dispersion of precipitate particles.

If the alloy has a dilute composition, the increased dislocation density with cold work may be sufficient to cause most of the solute atoms to form atmospheres. This will reduce the supersaturation of the matrix and the rate of nucleation. As an example, this phenomenon has been observed by Singhal[57] during the formation of sigma phase involving Ti atoms in an austenitic stainless steel. In this case, the phase did not form until recrystallization had reduced the dislocation density and freed Ti atoms for the aging process.

2.3 POST DEFORMATION ANNEALING

Returning a deformed metal to its prior condition of microstructure and mechanical properties requires certain processes that must be thermally activated in heat treatments called annealing. The phenomenon has been extensively studied[58,59,60] and can be classed into six groups according to the temperature ranges of heat treatment:

(1) Low temperature recovery

(2) Intermediate temperature recovery

(3) High temperature recovery

(4) Recrystallization

(5) Grain growth

(6) Secondary recrystallization

These can be discussed under the more general terms of recovery, recrystallization and grain growth. The former involves a redistribution of structural defects, while the latter two lead to a marked reduction of such defects. There is associated a peak release in stored strain energy due to cold work, during recrystallization and grain growth.

2.3.1 Recovery

In the recovery stage of annealing, the physical and mechanical properties that suffered changes as a result of cold work tend to recover to their original values. During low temperature recovery, elimination of deformation induced point defects takes place by the recombination of vacancies to dislocations.[61] This latter process can result in strain aging of BCC materials, by locking glide dislocations.

During the intermediate stage of recovery, dislocation cell wall structures are thickened and the ragged nature is reduced. Dislocation density is reduced through annihilation involving glide, climb, and cross slip mechanisms. In high temperature recovery, these same mechanisms allow large scale dislocation rearrangements into low energy configurations. This is called polygonization and results in the formation of tilt and twist boundaries. The former is associated with an initial excess of positive edge dislocation in the slip planes of a bent crystal (Fig. 16a). With thermal activation, the dislocations can lower their total strain energy by aligning into rows. General lattice curvature is removed (Fig. 16b) and the crystal segment between a pair of low angle tilt boundaries approaches the state of a strain free crystal with flat uncurved planes.[62] These segments are called subgrains and usually have an orientational difference of about 1°. Twist boundaries are similar low energy configuration for screw dislocation. The final stage of polygonization is the coalescense of two or more sub-boundaries into one, increasing the angle of rotation across the boundary. The driving force is the progressive reduction of the boundary energy per dislocation in the boundary.

In low SFE materials, climb and cross slip are inhibited by the extended nature of the dislocation. Frequently recovery is suppressed and recrystallization is the first major process to operate in annealing.[63] The temperature at which this takes place is lower than expected since no rearrangement or reduction in dislocation density would provide a higher driving force.

2.3.2 Recrystallization

Recrystallization is generally considered to be the result of two processes: 1) formation of recrystallization nuclei or grains; 2) growth of these grains into the deformed crystal. The mechanisms of these processes are fundamentally different. Nucleation involves the creation of high angle misorientation grain boundaries, while growth is the migration of these boundaries into the unrecrystallized matrix transforming it into strain free matrix.

Much information concerning recrystallization from over fifty years of study can be summarized into seven laws:[64]

(1) A minimum deformation is necessary to initiate recrystallization.

(2) The smaller the degree of deformation, the higher the temperature to initiate recrystallization.

(3) Increasing the annealing time decreases the temperature required for recrystallization.

(4) The larger the original grain size, the greater the amount of deformation required to give equivalent recrystallization temperature and time.

(5) Final grain size depends chiefly upon the degree of deformation and lesser upon the annealing temperature.

(6) For a given degree of deformation, increasing the working temperature results in a higher recrystallization temperature and coarser grain size.

(7) Recrystallized grains do not grow into deformed grains of identical or lightly deviating orientation.

Recrystallization kinetics show that a certain incubation period exists before recrystallization becomes detectable (Fig. 17). This is due to nucleation being a thermally activated process. Higher temperatures increase the probability of forming a nucleus, thus reducing the incubation period or minimum deformation required to initiate nucleation. This minimum deformation corresponds to an amount just capable of forming few nuclei.

The rate at which a metal recrystallizes depends on the rate at which nuclei form and the rate at which they grow. The recrystallized grain size depends upon the balance or ratio between nucleation and growth rates. Assuming that both are constant or represent some average value during an isothermal recrystallization process, a high ratio will result in many nuclei and a fine grain size. A low ratio means a slow nucleation rate compared to the growth rate resulting in a coarse grain size (Fig. 18).

Various mechanisms for nucleation of recrystallized grains have been proposed.[65] However, any one model must be consistent with the following observations:[66]

(a) Nuclei grains form in regions of large strain gradient. Pile ups of dislocation behind an obstacle (grain boundary, inclusion, and other dislocations) cause local curvature of the lattice and act as sites for recrystallizing nuclei. Generally, local lattice misorientation is a necessary and sufficient precondition for nucleation in a cold worked metal.

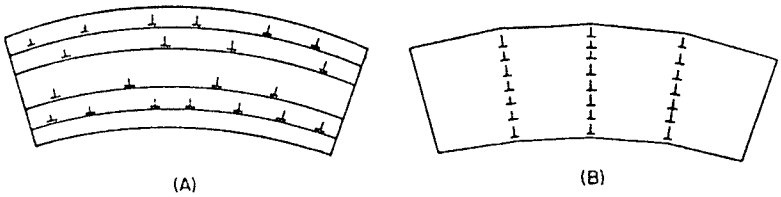

Fig. 16 Realignment of edge dislocations during polygonization; (A) before (B) after, [124].

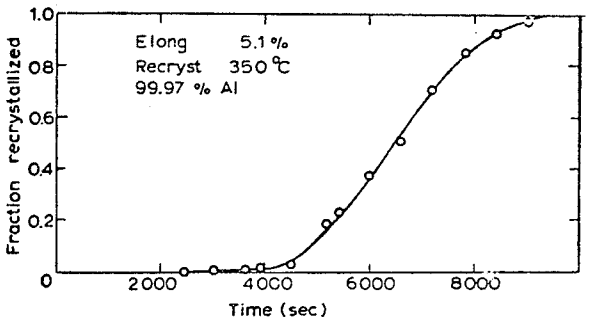

Fig. 17 Recrystallization kinetics for Al deformed 50% and annealed at 350° C, [64].

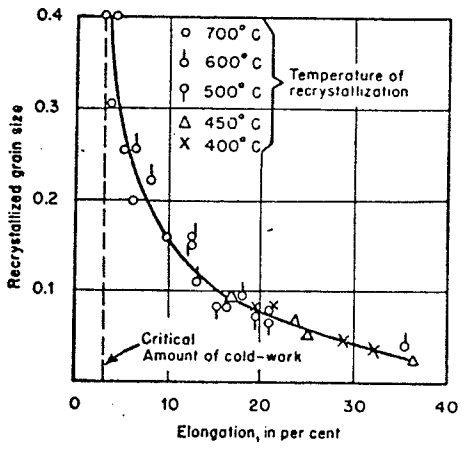

Fig. 18 Effect of prior cold work on recrystallized grain size of alpha-brass, [125].

(b) Increasing strain leads to larger misorientation and more sites for nucleation. Some materials exhibit deformation bands when cold worked. These can be thought of as pseudo-grain boundaries created by deformation in an originally strain free grain. They are sites of very high strain gradients and as such are preferrential sites for nuclei formation.[67]

(c) For two phase alloys, a fine dispersion of the second phase inhibits nucleation and growth, raising the recrystallizing temperature. Coarse dispersion aid nucleation without much affecting growth, thus lowering the recrystallizing temperature.

Three principal models of nucleation satisfy the above conditions and the following is a brief outline of each.

(1) Classical nucleation was first proposed by Burke and Turnbull.[68] Fluctuations in the positions of a group of atoms will occasionally by chance generate a strain free nucleus of new orientation, sufficiently large such that the release of strain energy will outweigh the surface energy of the matrix-nucleus interface. The model accounts for the existence of substantial incubation periods. However, since low angle boundaries would have low interfacial energy, nuclei with orientation not differing too much from the matrix would be expected. The opposite is, in fact, observed; that is, recrystallized grains of high angle boundaries.

(2) A subgrain growth model was first introduced by Cahn[69] with latter modification by Cottrell[70] (Fig. 19). In regions of high strain gradient or misorientation, polygonization is the first step to occur. Those subgrains which by chance have a relatively high misorientation will initially grow freely into their subboundaries. Growth slows down when the misorientation approaches a few degrees, and the sub-boundary dislocations begin to lose their identity. Somewhere near this point, the boundary changes from a sweeper up of dislocations to a destroyer of dislocations, and change in free energy across the boundary rises sharply,

again increasing the boundary mobility. It grows at a disproportionally rapid rate compared to its neighbours. Finally it becomes recognized as a new strain free crystal with an orientation distinctly different from its surrounding due to its large boundary angle.

Alternately, Hu[71] has shown that instead of sub-boundary migration to form high angle boundaries, subgrain coalescence takes place. His work[72] was with silicon iron crystals and has demonstrated that for certain orientations, cold work form deformation bands with the large misorientation between two bands divided into smaller steps of microband segments. These segments are the first to polygonize and subsequent growth of the sub-grains takes place by coalescence. This requires dislocation movement by climb and glide, away from a common subgrain boundary, and a rotation of the lattice by gross volume diffusion. The model is schematically shown in Figure 20. Subgrains A, B, C, and D undergo coalescence by elimination of their common sub-boundaries. As a result, the angle of misfit of the connecting boundaries around the rotating subgrain becomes higher. If the misfit across boundary is larger than some critical value, the boundary has a high mobility and moves into the polygonized matrix. Further co-alescence takes place at the low angle interface until a fully developed recrystallized grain surrounded entirely by high angle boundaries is formed. This period of time corresponds to the incubation period for re-crystallization.

(3) The third model of nucleation is strain induced boundary migration, first introduced by Beck and Sperry[73] and shown in Figure 21. A strain free nuclei is formed when one of the existing grain boundaries moves into a neighbouring grain leaving a recrystallized region behind. There is a

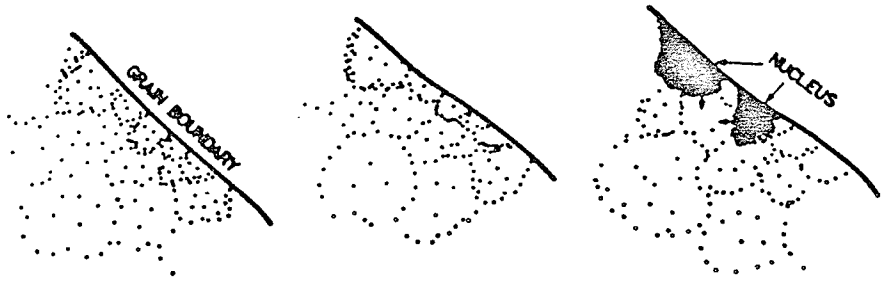

Fig. 19 Nucleation by subgrain growth. Subgrain boundaries thickly populated by dislocations (dots) have a high misorientation angle, and are the most likely to migrate, [66].

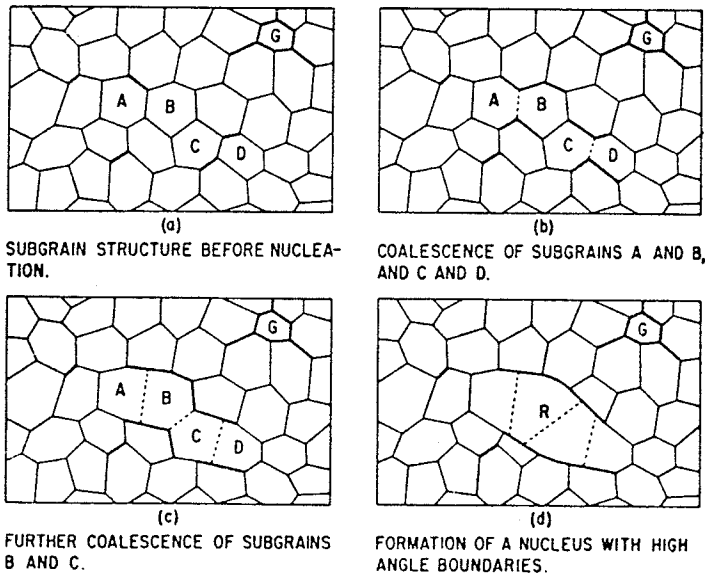

Fig. 20 Schematic representation for the formation of a recrystallized grain by the coalescence of subgrains, [67].

sharp discontinuity in dislocation density across the "bulging" grain boundary. The driving force for this migration is the negative total free energy change due to the strain energy release of dislocation removal, which more than compensates the interface energy increase accompanying the grain boundary bulge.

The migration of high angle grain boundaries form strain free crystal volume. The growth or migration rate is dependent on the volume free energy difference across the boundary due to the density of random dislocation and subgrain boundaries. Migration is a thermally activated process and an elementary conception of a grain boundary in an energy-distance diagram is shown in Figure 22.

The mobility represents a property of the grain and it is affected by several factors. The amount of strain energy in the matrix decreases with annealing time due to recovery, and mobility will depend on the rate of recovery. Experimental factors are temperature, impurity concentration, relative orientation of two grains, and orientation of the boundary itself. These are dealt with in a complex model by S. Hofmann and F. Haessner.[74]

2.3.3 Recrystallization of Two Phase Alloys

A special consideration of recrystallization relevant to this thesis is that involving two phase alloys. In general, solute atoms in solid solution can influence recrystallization in the following ways:[75]

(1) The stacking fault energy is lowered, promoting extended dislocations. This lowers the driving force for recrystallization and changes the internal stress distribution.

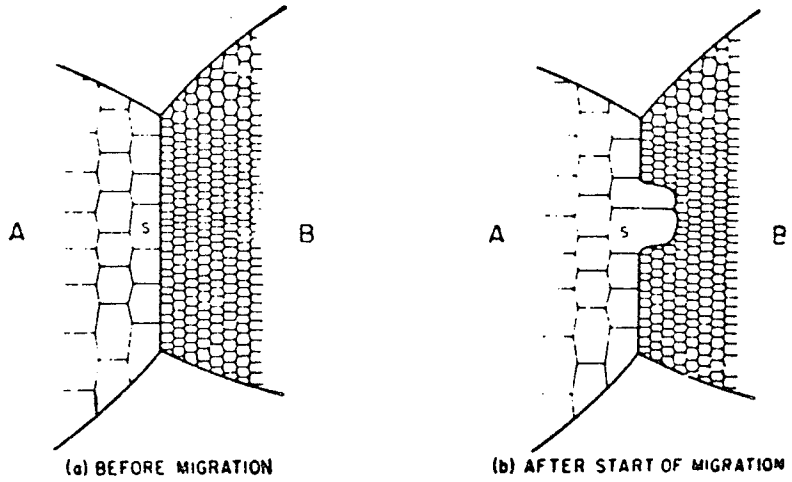

Fig. 21 Model for strain-induced boundary migration, [66].

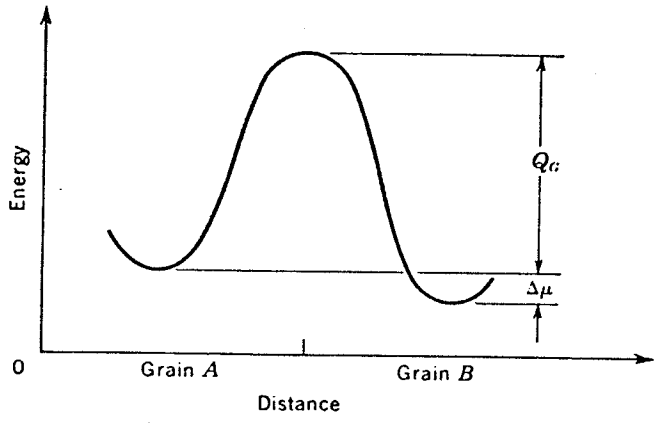

Fig. 22 Potential barrier involved in moving an atom across a grain boundary, [126].

(2) Segregation of atoms to dislocations promotes a retardation in dislocation rearrangements and subsequent delay in the start of recrystallization. The activation energy for nucleation is increased by an amount equivalent to the interaction between dislocation and foreign atoms.

(3) Segregation to grain boundaries reduces grain boundary mobility.

Recrystallization of supersaturated solutions may also occur simultaneously with precipitation and the two phenomena have a mutual influence. This has been extensively surveyed by Köster.[76] The following is a brief consideration of the possible reactions.

Assuming a constant size of nuclei formation, the temperature dependence for the start of recrystallization follows an Arrhenius type of equation:

$$t_r = A \exp \frac{Q_r (N)}{RT}$$

where A is a constant containing the driving force for the reaction, entropy term, and geometric factors; Q_r (N) is the activation energy for the formation of a mobile reaction front; R is the gas constant; T is the absolute temperature. Q_r (N) has the order of magnitude of the self-diffusion of the solvent atoms and decreases with increasing dislocation density (N).

The incubation period for precipitation of a stable phase is given by:

$$t_p = B \exp \frac{Q_p (c,T) + Q_d}{RT}$$

where B is a factor containing an entropy term and geometric factors; Q_p (c,T) is the activation energy for nucleation of the second phase; Q_d is the activation energy for diffusion of the solute. Q_p (c,T) decreases with increasing solute concentrates (c) and decreasing transformation temperature (T). At low temperatures of transformation, Q_p (c,T) $\ll Q_d$.

Both these expressions and the effect of their mutual influence are plotted schematically as a function of aging temperature in Figure 23. Those factors which influence recrystallization effect the driving force.

Recrystallization that proceeds by the migration of high angle boundaries through a matrix of random dislocations and subgrain walls is termed discontinuous. The driving force (P) together with the grain boundary mobility (M) determine the growth rate: $\dot{G} = M \cdot P$. The total driving force is actually the sum of three component forces, the first of which is due to the elimination of random dislocations and subgrain boundaries by the recrystallization front. This can be expressed by:

$$P_N = Gb^2 (N_0 - N_1)$$

where G is the shear modulas; b is the Burgers vector; N_0 and N_1 are the dislocation densities in the deformed and recrystallized region, respectively (Fig. 24a).

A reaction termed discontinuous precipitation can occur, in which precipitates form in the recrystallization front from a supersaturated solid solution, or from metastable particle (Fig. 24b). This sets up a second driving force[77] which can be expressed as:

$$P_c = \frac{1}{V} \Delta gc + \frac{1}{V} \Delta go$$

where Δgc is the difference in free energy of the supersaturated crystal and new strain free crystal created by the front; Δgo is the interfacial energy associated with particle formation. P_N and P_c can be additive, in which case a discontinuous recrystallization and precipitation reaction occurs. A deformed and supersaturated solid solution transforms to strain free grains containing precipitates (Fig. 24c).

Fig. 23

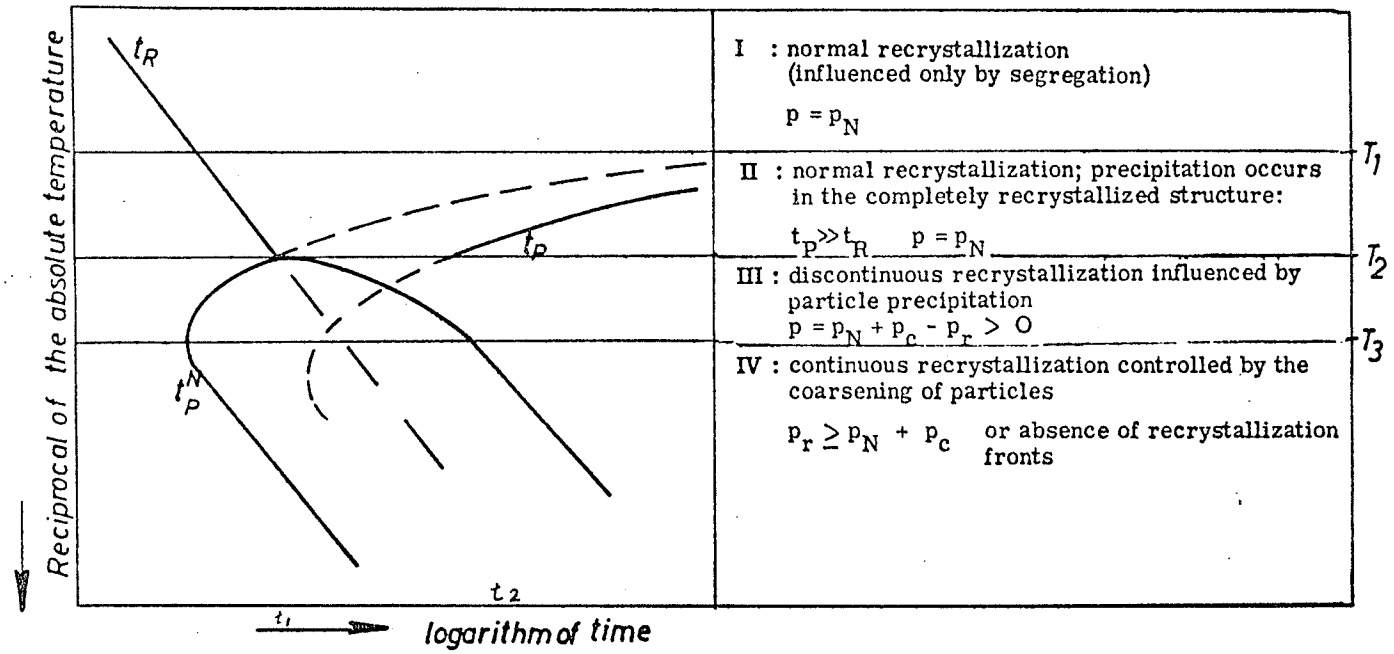

Schematic diagram showing possibilities for interaction between recrystallization & precipitation processes, [76].

KEY:

t_R - start of recrystallization

t_p - start of precipitation in undeformed crystal

t_p^N - start of continuous precipitation on dislocations

P - total driving force for recrystallization front

P_N - driving force due to elimination of dislocations and subgrain walls

P_c - driving force due to discontinuous precipitation

P_r - retarding force due to continuous precipitation ahead of reaction front

Fig. 24, [127]

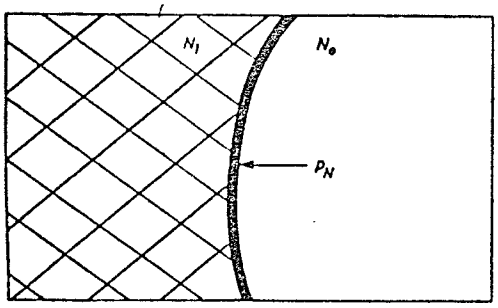

a) Discontinuous recrystallization. A grain boundary serves as reaction front and reduces the dislocation density from N_1 to N_0.

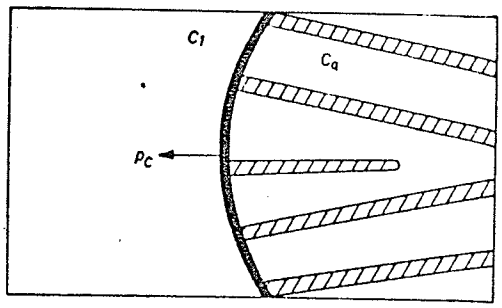

b) Discontinuous precipitation. The supersaturation of dissolved atoms (C_1) acts analogously to the dislocations as a chemical force on the reaction front.

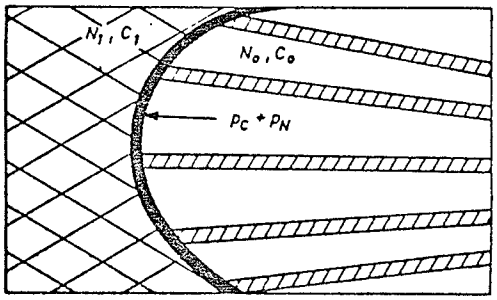

c) Combined discontinuous reaction. Both dislocation density N_1 and concentration C_1 are reduced to N_0 and C_0 in the reaction front. The prerequisite for this is a supersaturated defect solid solution.

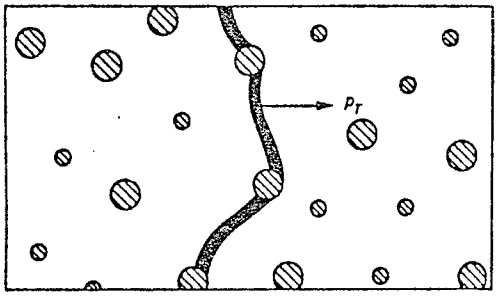

d) Dispersed particles exerting a retarding force P_r on the reaction front. If particles are equilibrium precipitate, they must be avoided. If they are not stable, they dissolve and reprecipitate behind the reaction front.

The continuous precipitation of particles in front of a discontinuous front can also occur, exerting a retarding force on the front (Fig. 24d). For spherical particles, Zener[78] has shown this force to be given by:

$$P_r = 3f / 2r \cdot \gamma \text{ G.B.}$$

where f is the precipitate volume fraction; r is the particle radius; γ G.B. is the grain boundary energy.

Here it is assumed that the interaction between grain boundary and particle is independent of the nature of the particle. Ashby et al[79] have revised this calculation, removing this assumption.

These three forces make up the total driving force (P) for discontinuous recrystallization, and are time and temperature dependent. P_N decreases as a result of recovery; P_c decreases and P_r increases if continuous precipitation occurs ahead of the dislocation front; P_r decreases as a result of particle coarsening. The driving force, as a function of time, is considered for temperature ranges of transformation shown in Figure 23.

(i) $T > T_1$: In this temperature range, precipitation does not occur and discontinuous recrystallization is only affected by the solute in solid solution. The driving force is equivalent to P_N and its variation with time is shown in Figure 25a.

(ii) $T_1 > T > T_2$: Here, precipitation occurs after recrystallization and solute atoms have no influence except as before. The removal of high dislocation densities and other defects by recrystallization removes possible nucleation sites which can be considered as delaying continuous

precipitation ($t_p^N >> t_R'$). Driving force variations with time are shown in Figure 25b.

(iii) $T_2 > T > T_3$: Continuous precipitation occurs at cold worked defect nucleation sites, before recrystallization. Depending on whether discontinuous precipitation occurs, the additive driving force P_c may be considered in the total driving force (Fig. 25c, 25e). In either case, the total driving force (P) decreases with time. If discontinuous recrystallization is not complete in the matrix before P becomes zero, the reaction front is stopped (Fig. 25d, 25f). In this case, the situation is that described for $T < T_3$.

(iv) $T < T_3$: In this temperature range, the total driving force for the movement of a discontinuous reaction front is less than zero (Fig. 25g); that is, $P_N + P_c < P_r$. The continuous precipitation in the cold worked region of the matrix has advanced to such a state that a discontinuous reaction front cannot move. In such a case, the annealing out of defects is controlled by the formation and resolution of precipitate particles.[80] This is called continuous recrystallization and is schematically sketched in Figure 26. The initial precipitation of particles reduces the segregation of the solute atoms at dislocations and facilitates their rearrangement. Further rearrangement is controlled by the disolution of the smaller and growth of the larger particles. As soon as a particle located at a dislocation node dissolves, these dislocations can migrate. Subgrain boundaries anneal by this process, forming larger defect free areas with increasing angles of misorientation. Finally the resultant dislocation network has the character of a grain boundary and the matrix is considered crystallized. The

Fig. 25 (a-g) Driving force of discontinuous recrystallization versus time for the various temperature ranges of Fig. 23.

KEY:

t_R' - start of recrystallization

t_R'' - finish of recrystallization

t_P^N - start of continuous precipitation

P_N - driving force due to elimination of dislocations and subgrain walls

P_c - driving force due to discontinuous precipitation

P_r - retarding force due to continuous precipitation ahead of reaction front

P - total driving force of discontinuous recrystallization

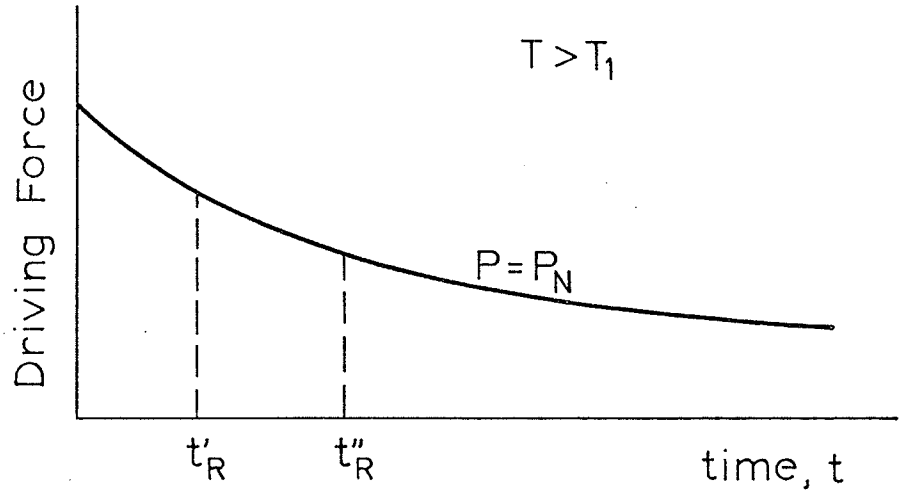

Fig. 25(a)

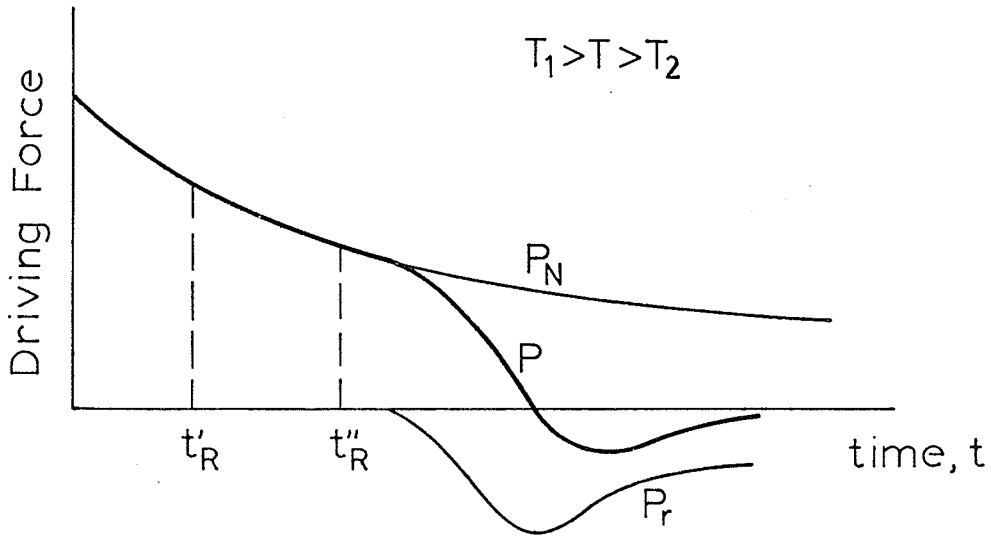

Fig. 25(b)

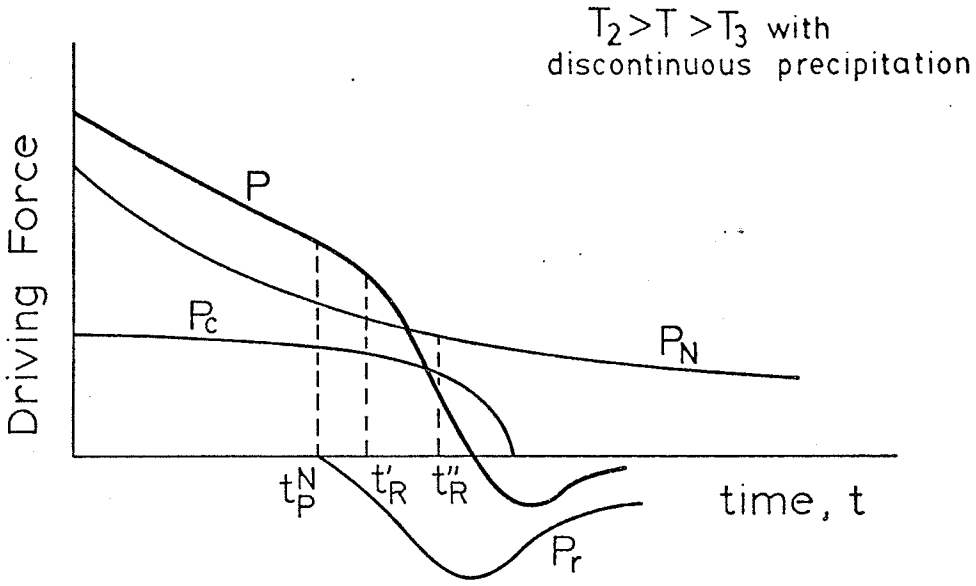

Fig. 25c

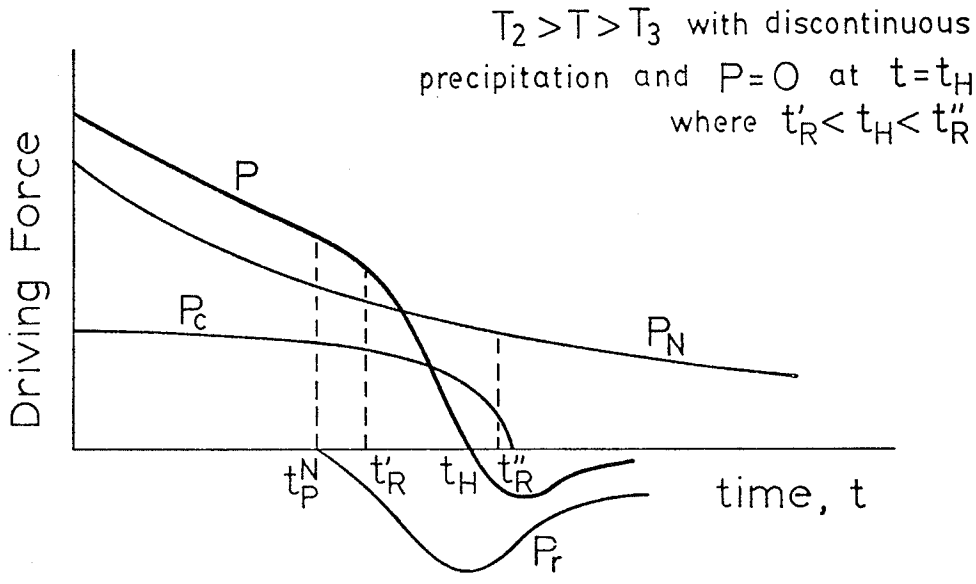

Fig. 25d

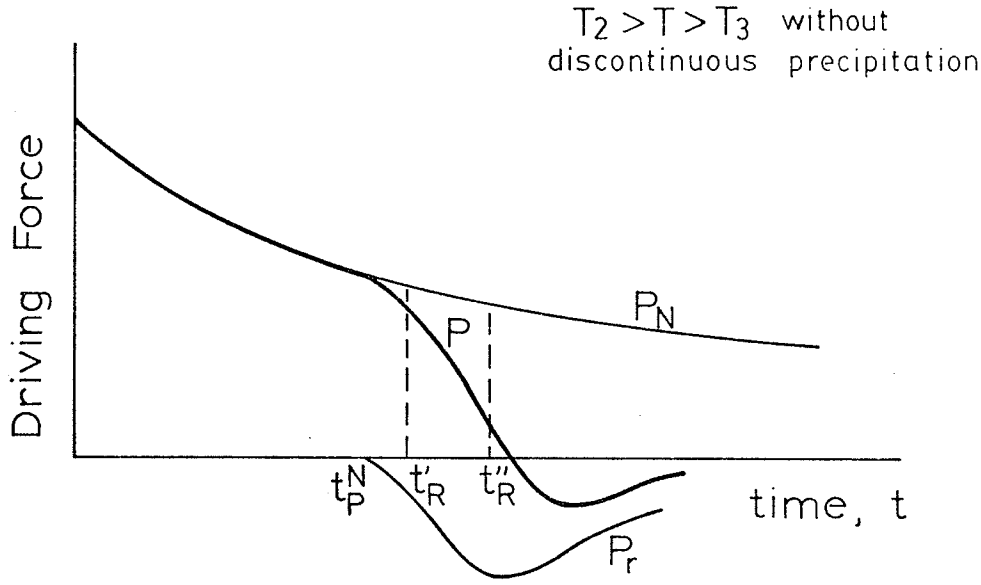

Fig. 25e

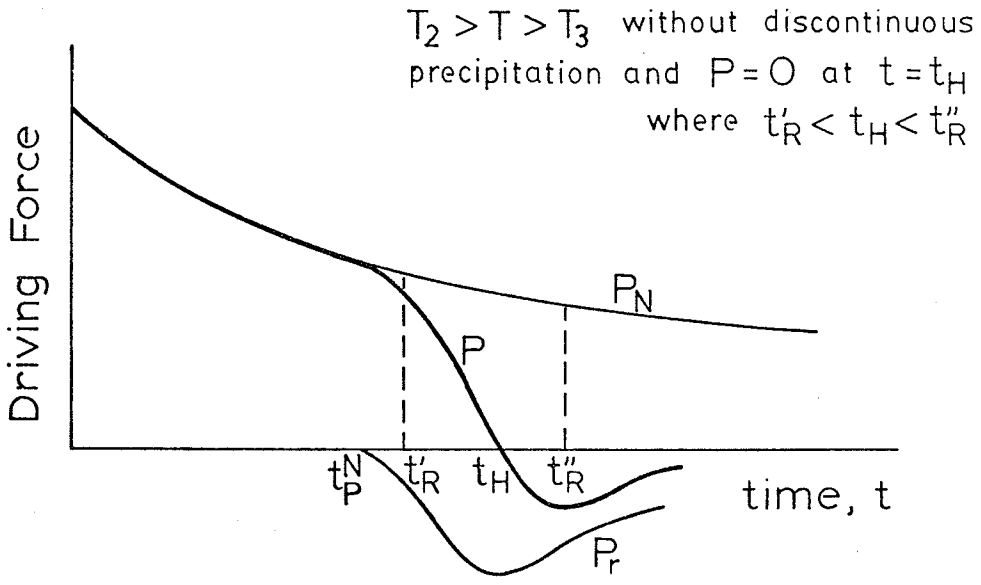

Fig. 25f

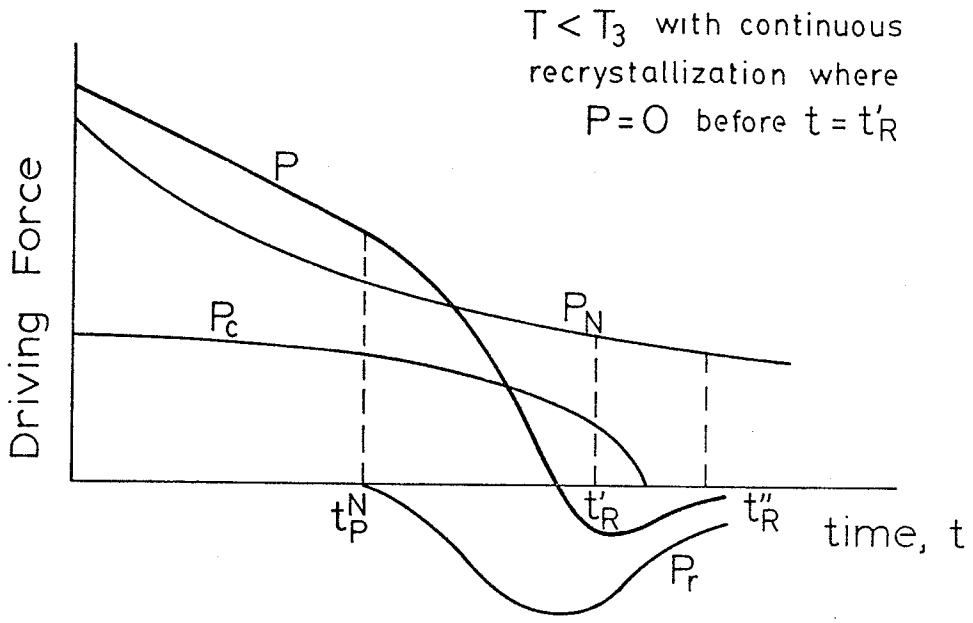
T < T3 with continuous
recrystallization where
P = 0 before t = t'R
Driving Force
P
Pc
PN
tPN
t'R
t''R
time, t
Pr

Fig. 25g

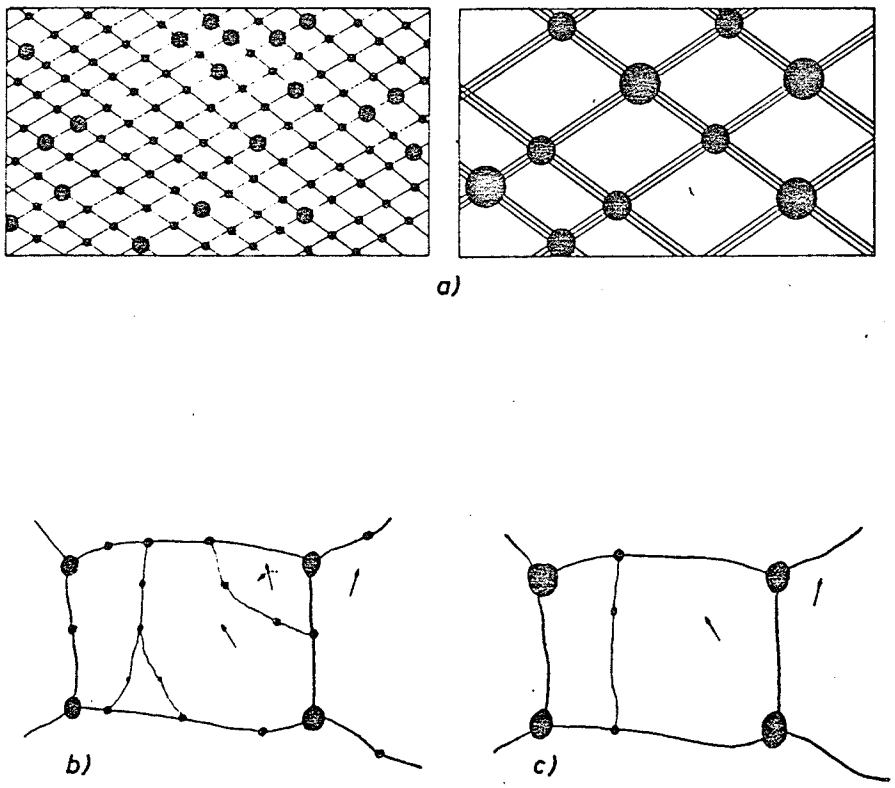

Fig. 26 Schematic sketch of continuous recrystallization, [76].

a) No grain boundaries are able to move as a recrystallization front. Annihilation and rearrangement of the dislocations are controlled by growth of the particles. Subgrains form and their size and orientation difference (indicated by thickness of the lines) increase.

b) Sub-boundaries are pinned by particles.

c) After dissolution of the smallest particles, a subgrain can anneal out by Y-node motion (left) or by subgrain rotation (right).

continuously recrystallized structure differs from the discontinuous kind, only in distribution of grain size and particles.

An increase in solute concentration for a constant dislocation density will shift the incubation time for precipitation to smaller values. Assuming that this has little effect on the beginning of recrystallization, the temperatures T_1, T_2, and T_3 are shifted to higher values.

An increase in dislocation density causes the start of recrystallization to be displaced to lower values, assuming the start of precipitation is not affected. The temperatures T_2 and T_3 are displaced to lower values and above a certain density, recrystallization is always complete before the start of precipitation (Fig. 27). However, it is reasonable to assume that an increase in dislocation density also reduces t_p^N for continuous precipitation. The effect of increasing dislocation density on the total driving force for continuous recrystallization at a constant time and temperature is shown schematically in Figure 28.

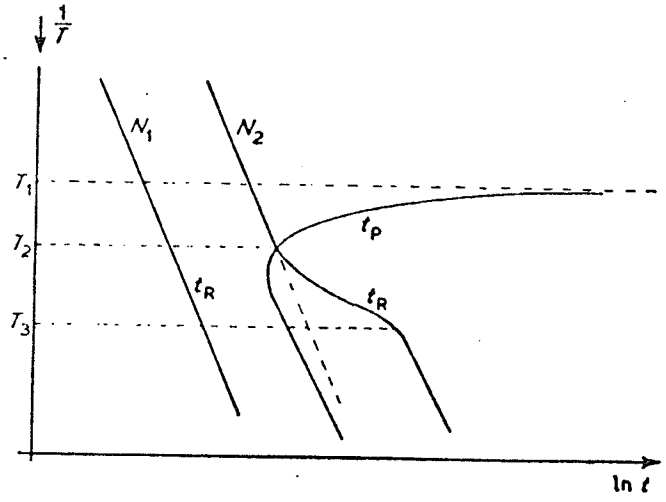

Fig. 27 Temperature dependence of incubation periods for precipitation (t_P) and recrystallization (t_R) as a function of dislocation density N, if it is assumed that the dislocations have little effect on the beginning of precipitation. With dislocation density N_1, there is no mutual influence of both processes. With dislocation density N_2 ($< N_1$) and temperature T_2, there is mutual influence of precipitation and recrystallization, [76].

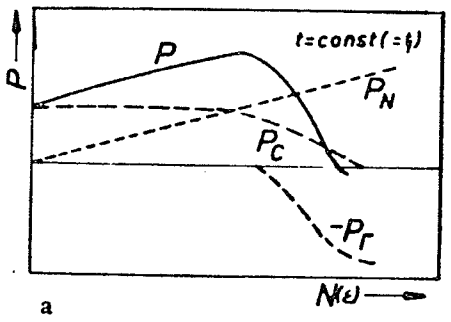

Fig. 28 The forces acting at the reaction front as a function of dislocation density N, [76].

CHAPTER 3 EXPERIMENTAL TECHNIQUES

3.1 ALLOY FABRICATION

The nominal composition of the alloy used in this investigation was 40% Co, 38% Ni, 17% Cr, and 5% Nb, prepared with material of the following purities: Co 99.9%, Ni 99.9%, Cr 99.9%, and Nb 99.9%. Alloys were made in an induction furnace under a partial pressure of argon and 15 mm. square ingots were cast in sand moulds. The ingots were slightly cold rolled and then soaked for three days at 1100° C in an argon filled silica capsule. Subsequent steps of cold rolling and annealing at 1200° C for five to six hours were followed until the desired thickness for tensile specimens or thin foils was obtained. Cooling from the annealing temperature was carried out by breaking the silica capsules in an iced water medium. It was found that an initial annealing temperature greater than 1100° C results in the ingot cracking on subsequent cold rolling. This was probably due to the inhomogeneity in the as cast condition leading to localised melting at grain boundaries.

The degree of deformation by cold rolling was measured as a reduction in thickness of the specimen. Light, moderate, and heavy deformations represented one or more passes through the rolls until the initial thickness of the material in the as annealed condition was reduced by 5%, 30%, and 60%, respectively. Aging of the material was in the main at 800° C and always in argon filled silica capsules.

3.2 MECHANICAL PROPERTIES

All tensile specimens during this investigation were prepared from material in the states of cold rolled and cold rolled and aged. Tensile specimens were shaped on a milling machine to a one inch guage length and ¼ inch radii shoulders. All samples were 2 mm. in thickness to ensure a minimum of five grains across the cross-section. These specimens were tested in an Instron testing machine at room temperature and at a strain rate of 3.33×10^{-3}/sec.

Hardness measurements were done with a Vickers pyramid indentor at a load of ten kilograms. Surfaces of the specimens were polished to a grit of 600.

3.3 PRECIPITATE EXTRACTION

Precipitation occurs on aging at 800° C with or without prior deformation. The precipitate particles were separated from the matrix in an extraction cell using an electrolyte of 10% sulphuric in water at a current density of about 0.05 amperes per cm^2. After the matrix had completely dissolved, the precipitate and electrolyte were separated in a centrifuge. The solution was then carefully siphoned off and the remaining precipitate washed in alcohol and centrifuged several times. The well dried precipitate was then scraped from the centrifuge tubes and collected into a small vial. X-ray powder samples were then prepared by mounting the precipitate powder on thin glass rods with glue. The samples were placed in a Philips powder camera and irradiated with filtered $CoK\alpha$ radiation. Analysis of the results followed the standard Debye-Scherrer technique.

3.4 OPTICAL METALLOGRAPHY

Prior to electron microscope investigation, extensive optical metallography was carried out. Samples were mechanically polished in successive stages of emery paper, diamond pastes, and Al_2O_3 powder, the latter of which had the finest size of 0.05 μ. The polished specimens were etched electrolytically in a solution of six parts HCl acid to one part H_2O with an applied voltage of two to five volts. The etched samples were then examined on a Vickers 55 optical microscope.

3.5 ELECTRON MICROSCOPY

3.5.1 Extraction Replicas

Carbon extraction replicas of various deformed and aged specimens were prepared. The surfaces were prepared as above for optical metallography. However, the degree of electro-etching was somewhat more. A thin carbon film was deposited on the surface with an evaporating unit. The surface was then scribed in squares of approximately 2 mm. sides. A further electro-etching was carried out in a solution of 5% sulphuric acid in methanol at ten volts for a few seconds. The specimen was then washed by carefully dipping into a pure ethanol bath, and the surface allowed to dry for a few seconds. The carbon film was lifted from the specimen surface by slowly immersing the specimen into a distilled water bath, and then collected on 200 mesh copper grids for the microscope holder.

3.5.2 Thin Foils

Thin foils were prepared by an electrolytic jet polishing technique. Specimen strips approximately 6 mm. square were used with thickness varying from 0.15 - 0.30 mm. The edges were lacquered and the specimen centered in the jet stream of the polishing cell containing an electrolyte of 10% perchloric acid in methanol. The temperature of the electrolyte was maintained at -50° C to -60° C in a dry ice methanol bath. Polishing was carried out at the high voltage end of the plateau region in the characteristic voltage-current polarization curve. This was generally 20 V with a current density of 200 milliamperes. When a hole formed, the specimen was quickly removed, then washed and the lacquer removed in a room temperature bath. After drying, the specimen was placed between two tissue sheets and the thinned area cut carefully away with a sharp scalpel. This segment was mounted into a specimen holder on 75 mesh copper grids. Examination of thin foils and extraction replicas was made in a Philips EM 300 microscope.

CHAPTER 4 EXPERIMENTAL RESULTS

As noted before, the nominal composition of the alloy used during the present investigation was 40% Co, 38% Ni, 17% Cr, and 5% Nb. In studying the effects of prior cold work on the aging behaviour, it was decided to use light, moderate, and heavy deformations which were arbitrarily chosen to be cold rollings of 5%, 30%, and 60% reductions respectively. In considering earlier work by Chung et al[5] in the solution treated and quenched state, the aging temperature for the studies was in the main 800° C and for times up to 150 hours.

4.1 HARDNESS MEASUREMENTS AND TENSILE TESTING

The Vickers pyramid hardness against aging time is plotted in Figure 29 for the solution treated condition and prior deformation of 5%, 34%, and 60%. It is observed that the change in peak harness on aging gradually diminishes with increasing amount of cold rolling. In the solution treated condition, an increase of 110 VPH occurs after 104 hours, while prior 60% cold working demonstrates a nearly continual drop in hardness of 36 VPH for the same aging time. Thus the time to attain peak hardness is gradually reduced from approximately 500 hours aging time with the solution treated condition to zero time in the heavily deformed state. Chung et al's[5] earlier work has shown that the hardness change is due to precipitation of orthorhombic Ni_3Nb. From Figure 29, it can be inferred that light deformation (5%) accelerates precipitation since its hardness curve is akin to aging at a higher temperature with the consequent lowering of the peak hardness (310 VPH to 288 VPH) and shifting it to lower values of aging time (500 hr. to 54 hr.). However, moderate (34%) and heavy (60%) deformations with their overall increase in hardness and different rate of hardness

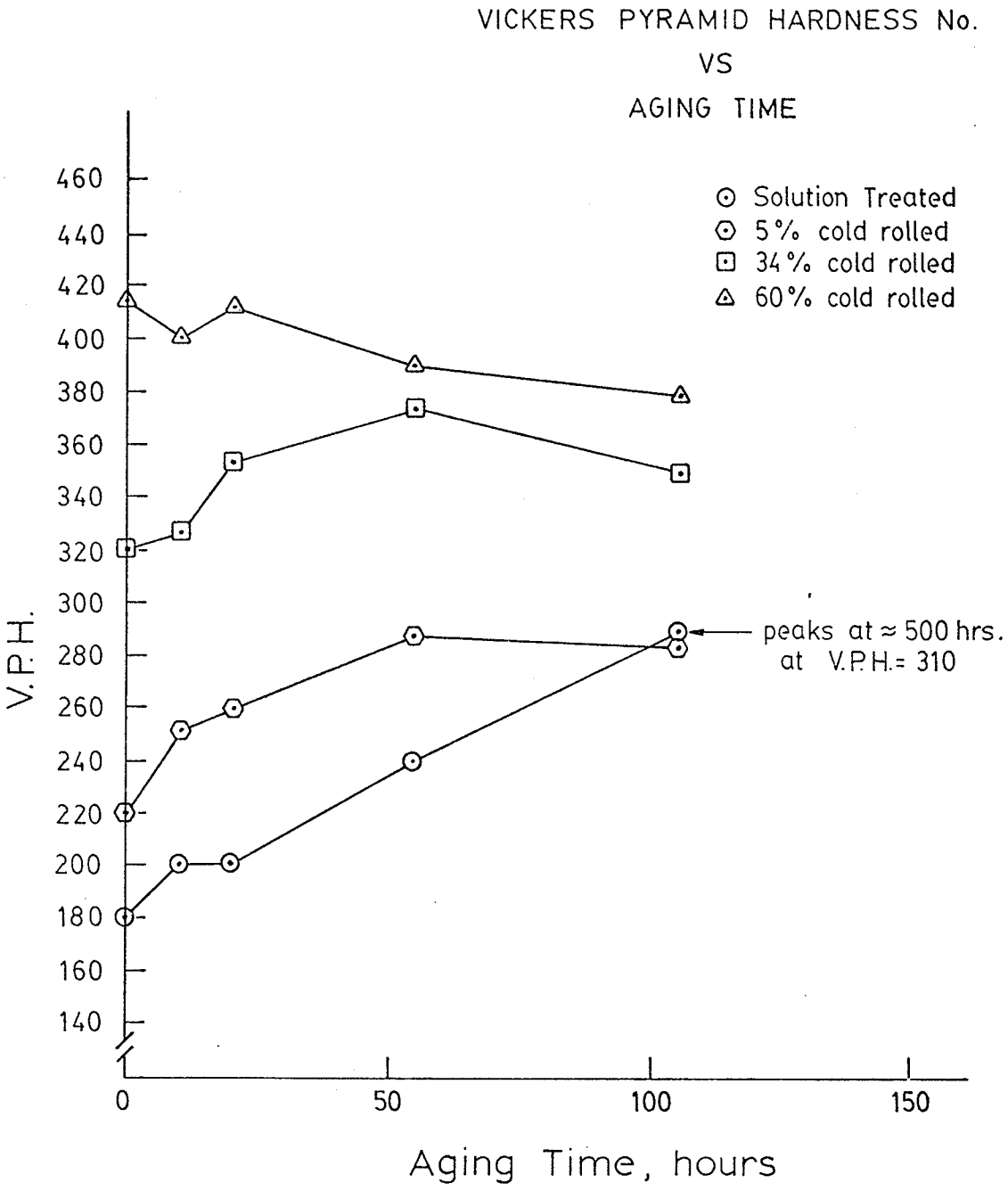
VICKERS PYRAMID HARDNESS No.
VS
AGING TIME
Solution Treated
5% cold rolled
34% cold rolled
60% cold rolled
peaks at ≈ 500 hrs.
at V.P.H.= 310
V.P.H.
460
440
420
400
380
360
340
320
300
280
260
240
220
200
180
160
140
0
50
100
150
Aging Time, hours

Fig. 29

change suggest that different or additional factors are involved in aging.

Tensile test results of specimens aged after solution treatment and various amounts of deformation are presented in Figures 30 - 33. The work on the solution treated condition[81] shows 150% and 90% increase in yield strength (YS) and ultimate tensile strength (UTS) respectively, after only 12 hours aging time. Subsequent changes in UTS are slight with a peak at 48 hours, while the YS drops, then rises again, leveling to a fairly constant value at 150 hours. The percentage of elongation drops continually from 75% to 11% after the same aging time.

In the lightly cold rolled condition, the initial improvement over the as annealed condition before aging is 75% for the YS and 200% for the UTS. With aging, the YS first drops slightly and then further increases by about 6% on aging for 100 hours. The UTS increases steadily upon aging with a 14% improvement after 100 hours aging time. Also in this time, the percentage elongation has dropped steadily from 60% to 30%.

Tensile tests on the moderately cold rolled condition (Fig. 32) show an initial increase in YS and UTS over the solution treated condition of 300% and 150% respectively. There is also a correspondingly sharp (73%) drop in elongation. With aging, the UTS remains fairly constant, while the YS peaks after 50 hours with a 17% improvement from initial cold rolled condition. The elongation falls continually from 20% to 15% with aging of 100 hours.

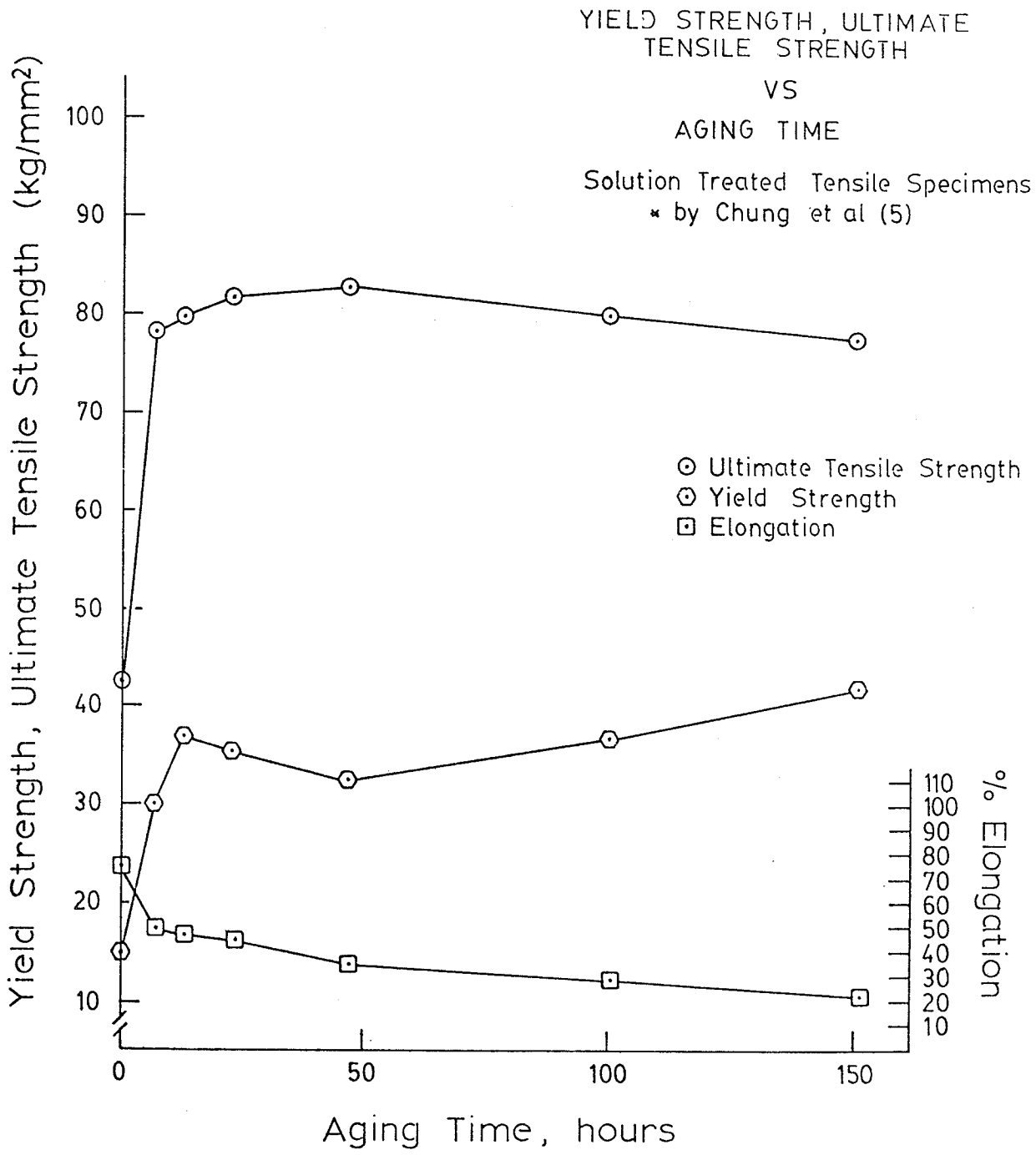
YIELD STRENGTH, ULTIMATE TENSILE STRENGTH
VS
AGING TIME
Solution Treated Tensile Specimens
* by Chung et al (5)
Ultimate Tensile Strength
Yield Strength
Elongation
Yield Strength, Ultimate Tensile Strength (kg/mm²)
% Elongation
Aging Time, hours
100
90
80
70
60
50
40
30
20
10
110
100
90
80
70
60
50
40
30
20
10
0
50
100
150

Fig. 30

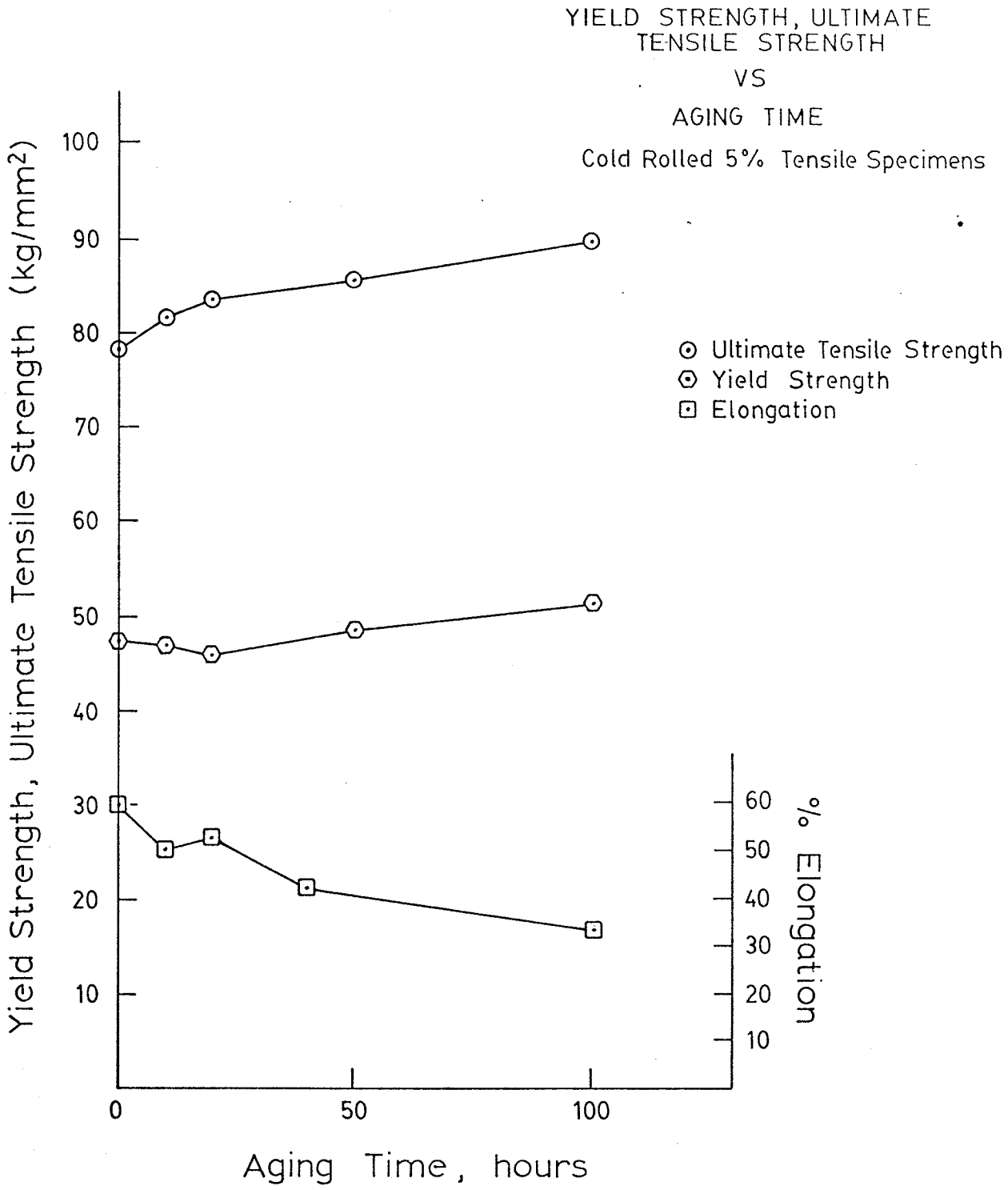
YIELD STRENGTH, ULTIMATE TENSILE STRENGTH
VS
AGING TIME
Cold Rolled 5% Tensile Specimens
Ultimate Tensile Strength
Yield Strength
Elongation
Yield Strength, Ultimate Tensile Strength (kg/mm²)
% Elongation
Aging Time, hours
100
90
80
70
60
50
40
30
20
10
60
50
40
30
20
10
0
50
100

Fig. 31

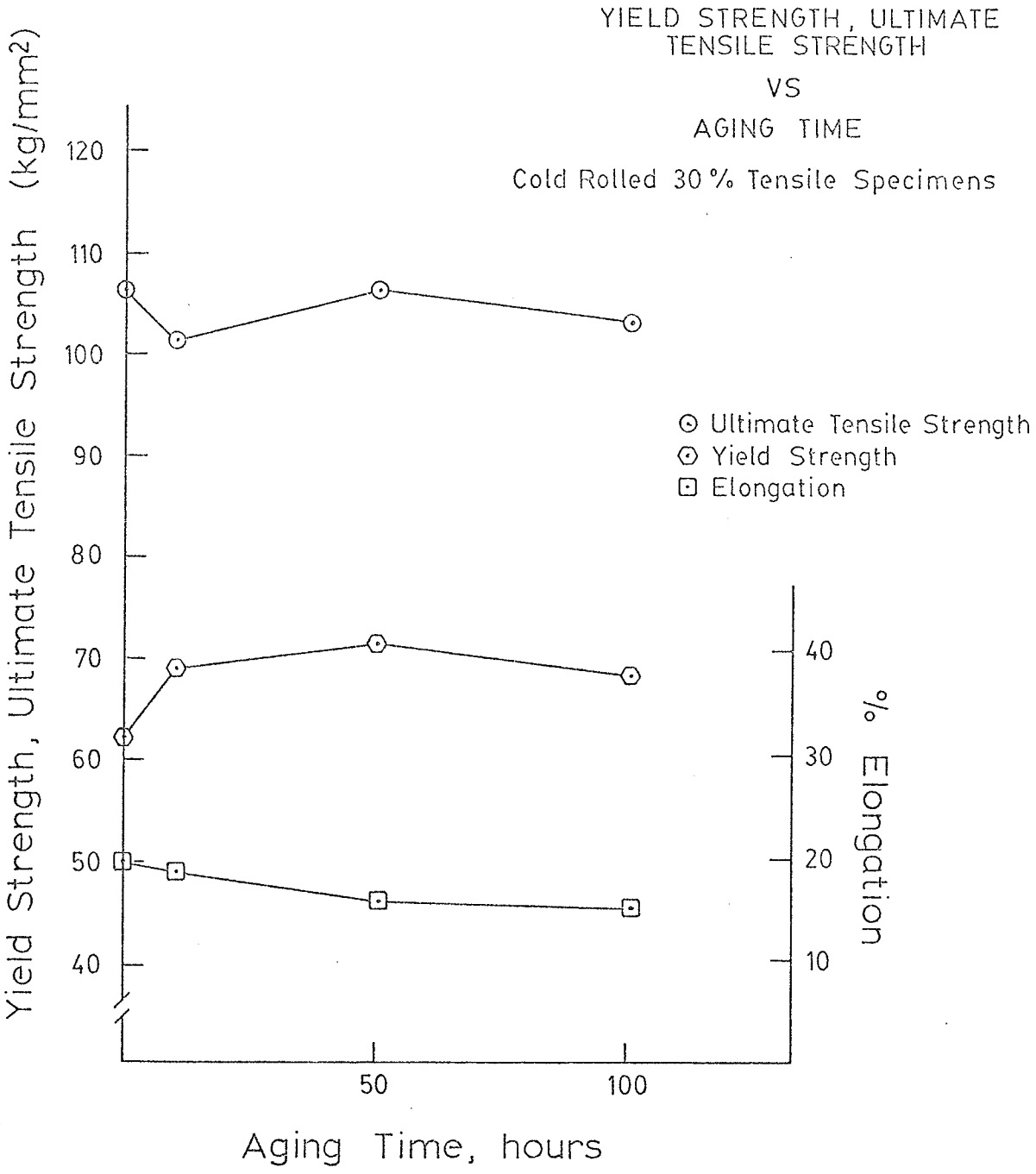
YIELD STRENGTH, ULTIMATE TENSILE STRENGTH
VS
AGING TIME
Cold Rolled 30 % Tensile Specimens
Yield Strength, Ultimate Tensile Strength (kg/mm²)
120
110
100
90
80
70
60
50
40
40
30
20
10
% Elongation
50
100
Aging Time, hours
Ultimate Tensile Strength
Yield Strength
Elongation

Fig. 32

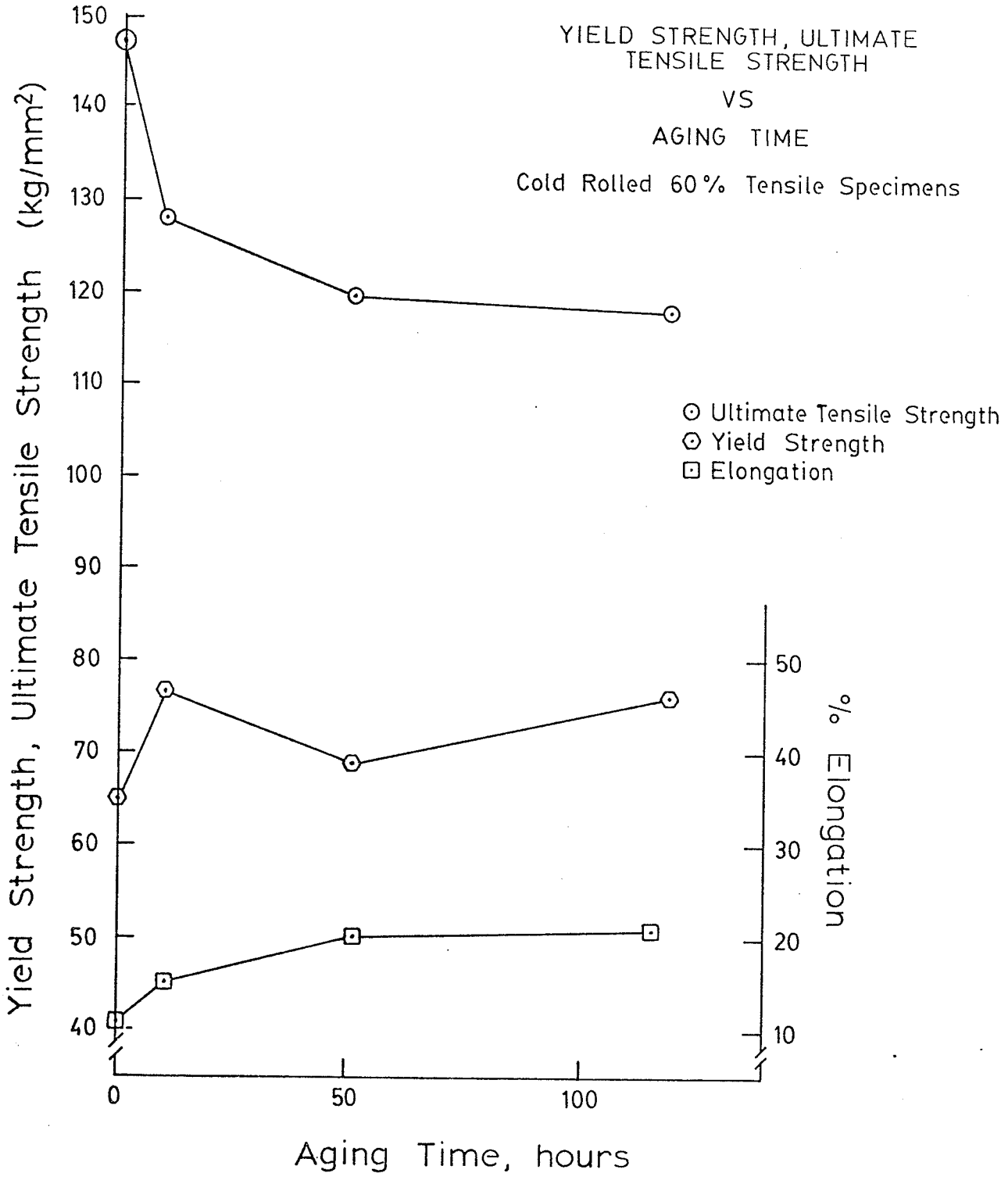
YIELD STRENGTH, ULTIMATE TENSILE STRENGTH
VS
AGING TIME
Cold Rolled 60% Tensile Specimens
⊙ Ultimate Tensile Strength
⊙ Yield Strength
⊡ Elongation
Yield Strength, Ultimate Tensile Strength (kg/mm²)
% Elongation
Aging Time, hours
150
140
130
120
110
100
90
80
70
60
50
40
50
40
30
20
10
0
50
100

Fig. 33

Tensile results on heavy cold rolling (Fig. 33) as compared with moderate cold rolling demonstrate a similar increase in initial YS over the as annealed condition. However, the initial UTS has improved by 250%. On aging, double peak values of YS occur at 10 and 119 hours, each representing a 17% improvement over the initial value. The UTS values, on the other hand, drop with a decreasing rate on aging. The total change after 100 hours from the initial cold worked condition is -20%. The corresponding elongation increases with aging time from a value of 12% to 22%. The character of the change in UTS and elongation curves are significantly different from those of the solution treated, lightly cold rolled, and moderately cold rolled conditions. This suggests the possibility of some additional phenomena occurring with precipitation, namely recrystallization.

4.2 OPTICAL METALLOGRAPHY

A series of optical metallographic examinations were made on solution treated, and lightly, moderately, and heavily deformed specimens in the pre and post aging conditions. The more significant of these results are given in Figures 35 to 48.

The as solution treated material exhibited a generally equiaxed grain structure with the frequent presence of annealing twins (Fig. 35). Grain size on solution treating at 1250° C seemed to be dependent on the amount of prior deformation to a greater degree than on the time of annealing (Fig. 34). On aging the solution treated specimen at 800° C,[5] precipitation of orthorhombic Ni_3Nb occurs in the form of long plates lying on the (111) planes. In Figure 36, the traces of these planes are clearly delineated by the four intersecting directions of the Ni_3Nb precipitates.

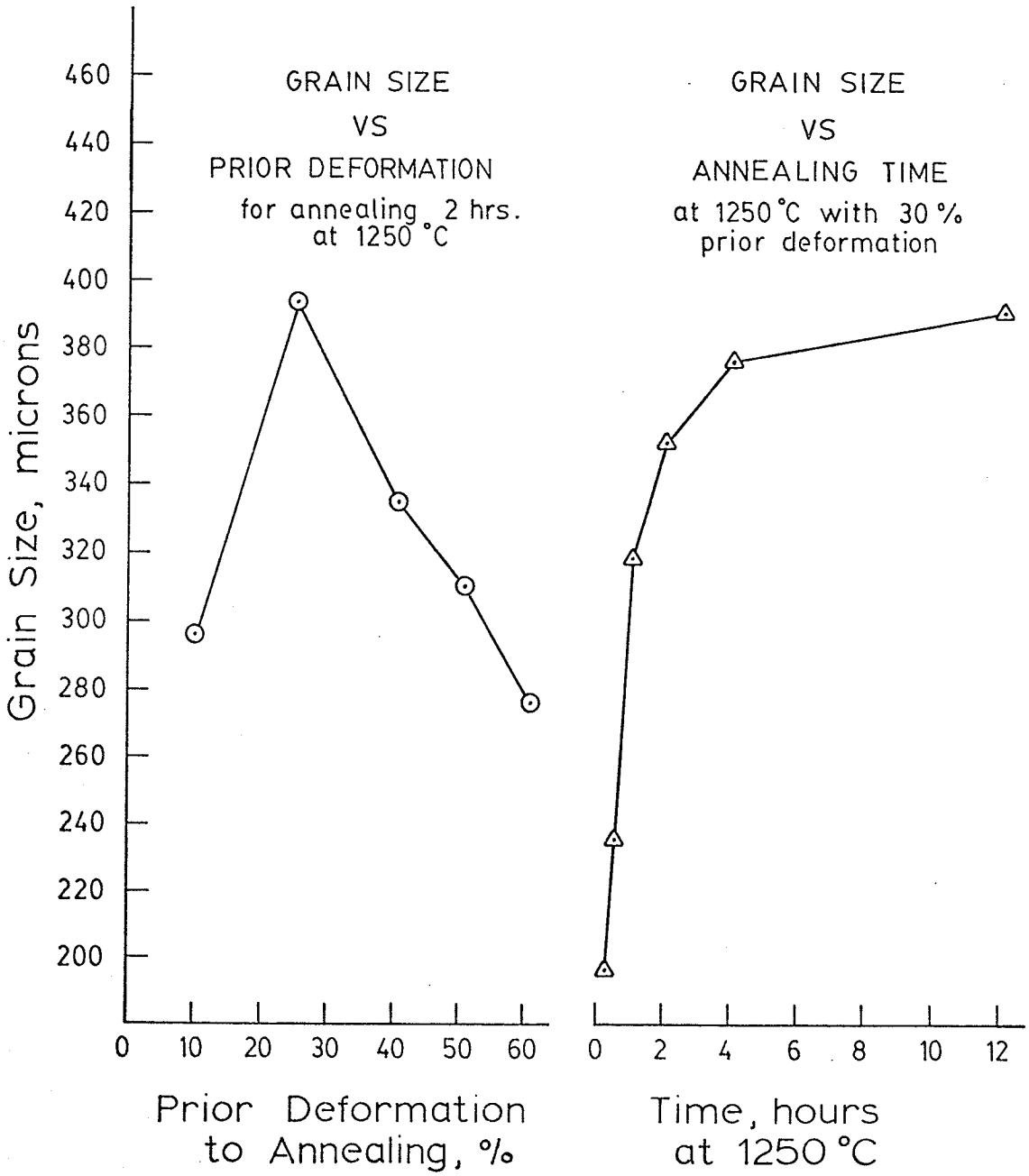
GRAIN SIZE
VS
PRIOR DEFORMATION
for annealing 2 hrs.
at 1250 °C
GRAIN SIZE
VS
ANNEALING TIME
at 1250 °C with 30 %
prior deformation
Grain Size, microns
460
440
420
400
380
360
340
320
300
280
260
240
220
200
0
10
20
30
40
50
60
Prior Deformation
to Annealing, %
0
2
4
6
8
10
12
Time, hours
at 1250 °C

Fig. 34

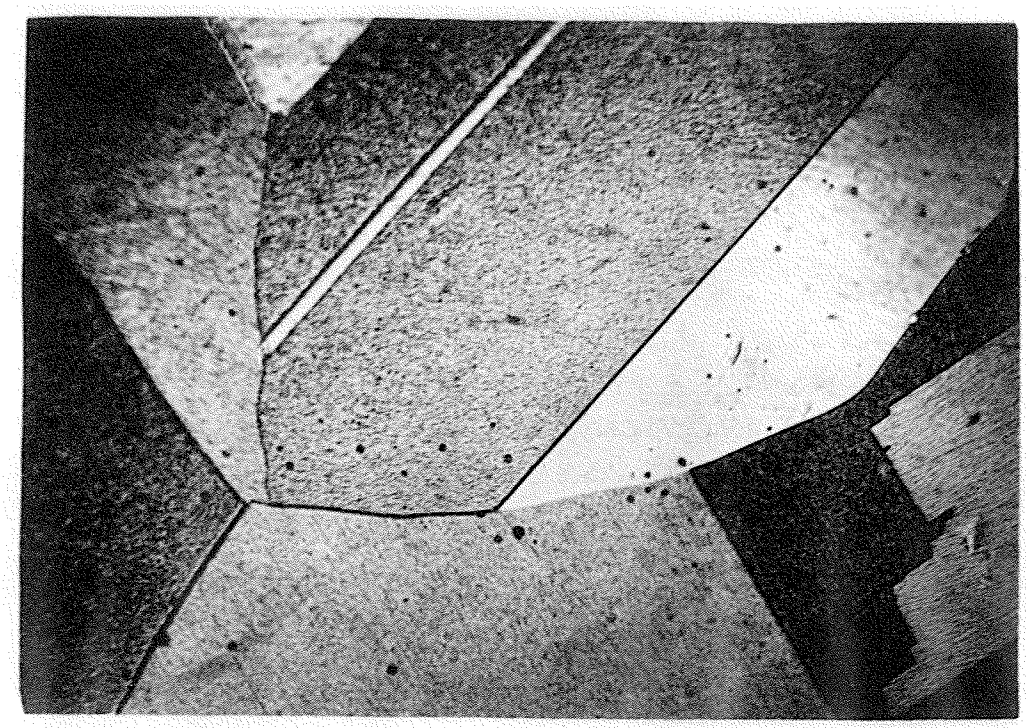

Fig. 35 Microstructure of as solution treated at 1200° C. (312x)

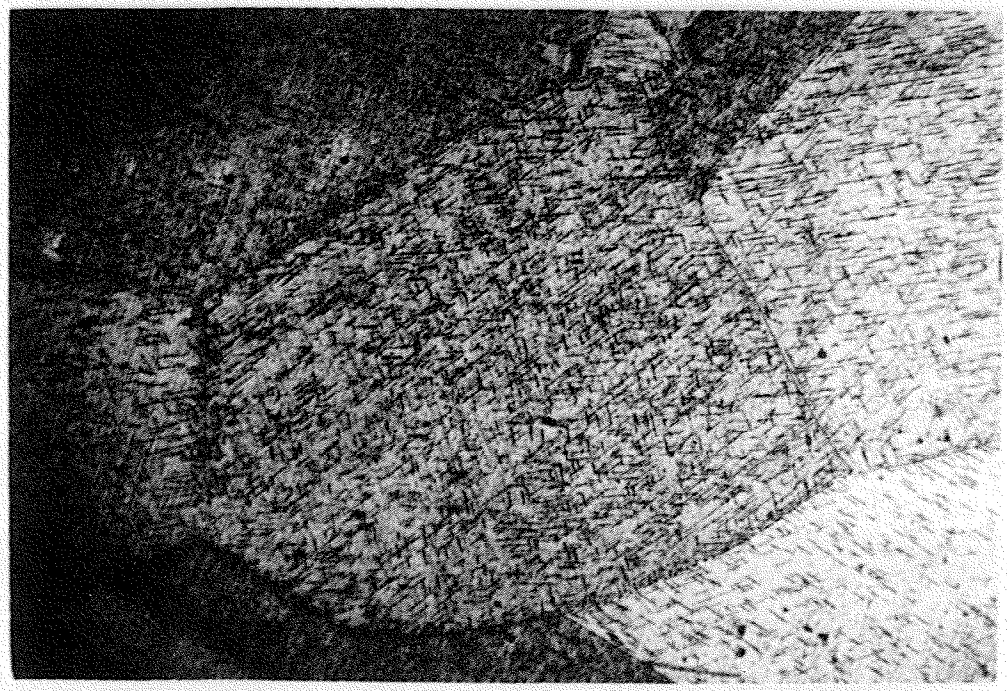

Fig. 36 Microstructure of as solution treated + 50 hr. at 800° C. (420x)

A prior deformation of 5% does little to change the microstructure except increase the volume fraction of precipitate for a given length of aging time. Early stages of precipitation are shown in Figure 37 (after 10 hours), while the more advanced stages are shown in Figure 38 (after 50 hours).

A deformation of 30% produces a general twisting and bending of grains and twin boundaries as well as a general network of striations in the grain interior (Fig. 39). Aging accents the striated nature as shown in Figures 40 - 42. After 10 hours at 800° C, the majority of striations seem to be parallel to those formed by cold working, but are much more distinct. After 50 hours, a clear cross-hatched network of long precipitates and striation has developed similar to that observed on aging the solution treated and lightly deformed specimens. Figure 41 also shows evidence of grain boundary precipitation occurring. After 100 hours, the structure does not seem to have changed greatly, except for an increase in precipitate size and appearance of small recrystallized grains, as shown in Figure 42.

Heavy deformation of 60% produces a markedly striated optical microstructure (Fig. 43), which is retained and sharpened with an aging time of 10 hours (Fig. 44). However, with further aging, the microstructure becomes less well defined, as shown in Figure 45. A cross-hatched network of long precipitate is visible in Figure 46, but not to the extent observed with moderate deformation. This figure also shows areas where the striations have disappeared, leaving behind small distorted spheres of about ½ μ in size. After 119 hours, the striation disintegration is much more extensive,

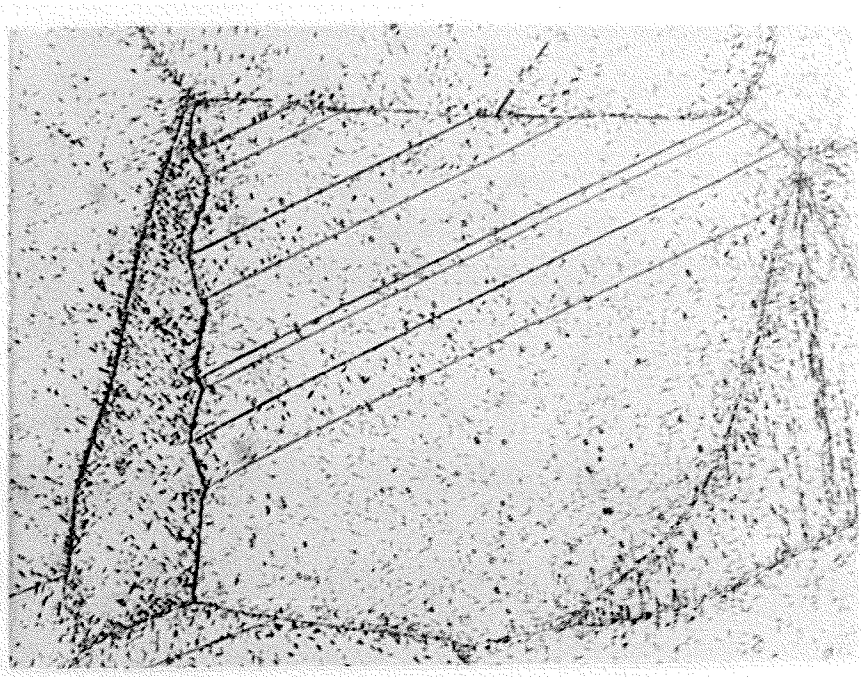

Fig. 37 Microstructure of 5% cold rolled (CR) + 10 hr. at 800° C. (150x)

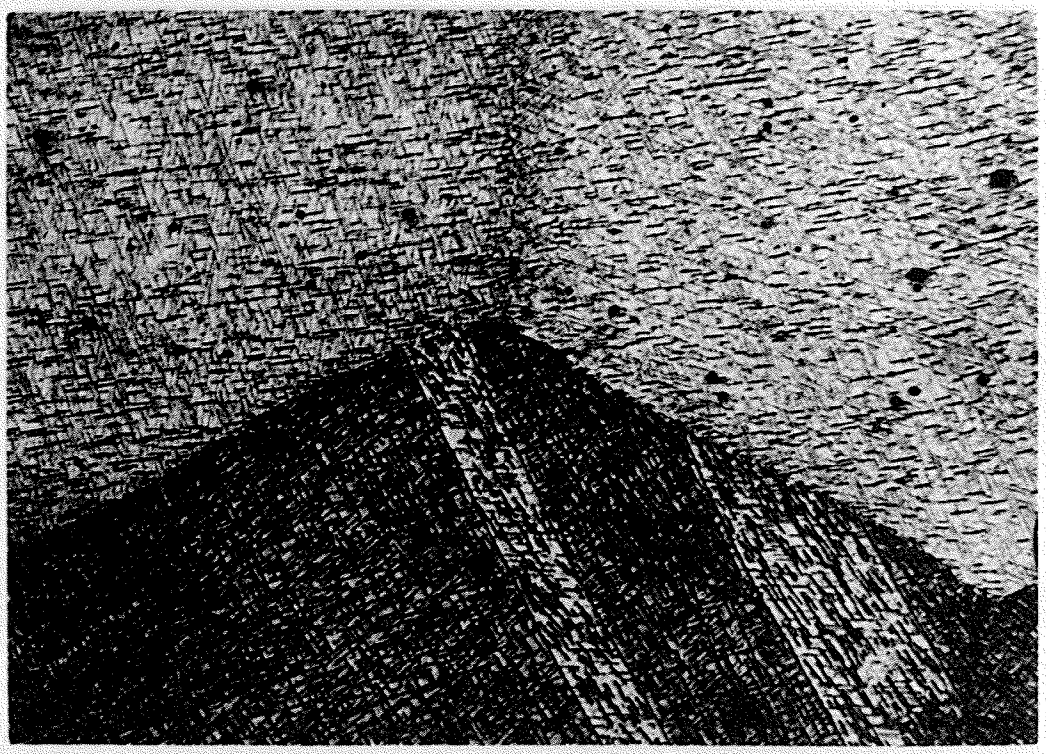

Fig. 38 Microstrucutre of 5% CR + 50 hr. at 800° C. (350x)

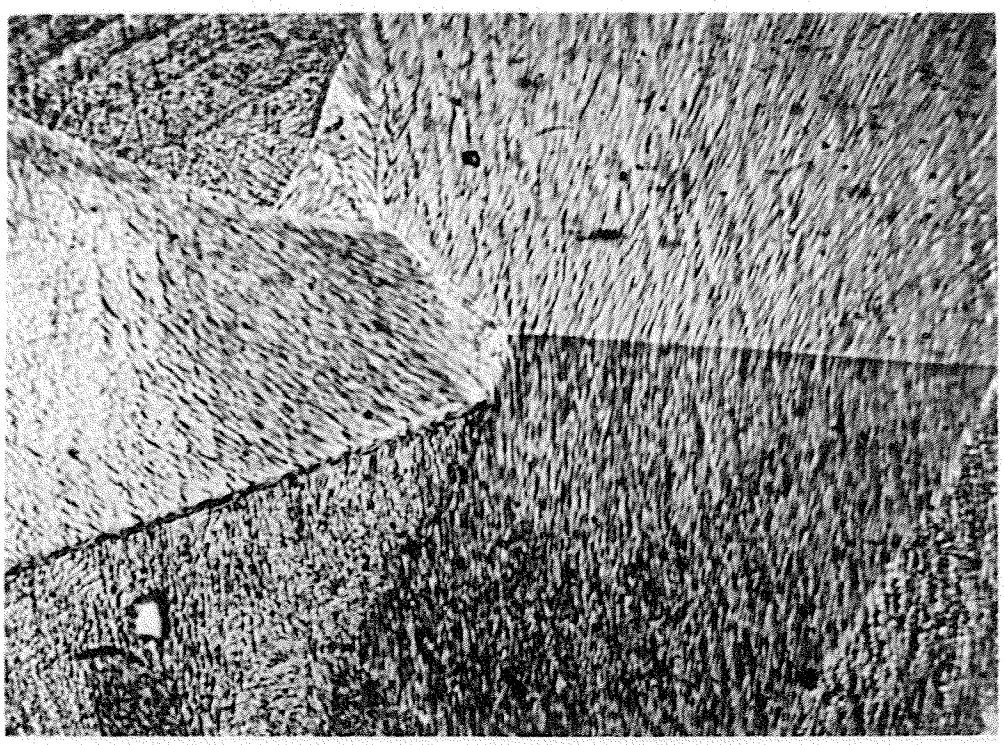

Fig. 39 Microstructure of as 30% CR. (1720x)

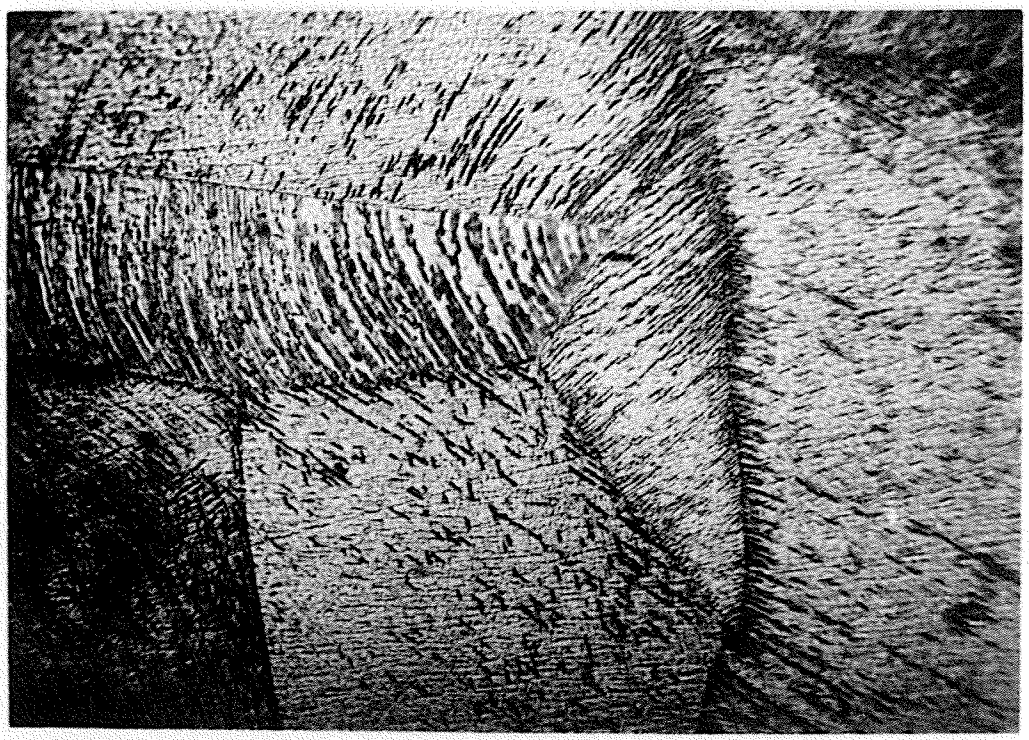

Fig. 40 Microstructure of 30% CR + 10 hr. at 800° C. (1330x)

Fig. 41 Microstructure of 30% CR + 50 hr. at 800° C. (1560x)

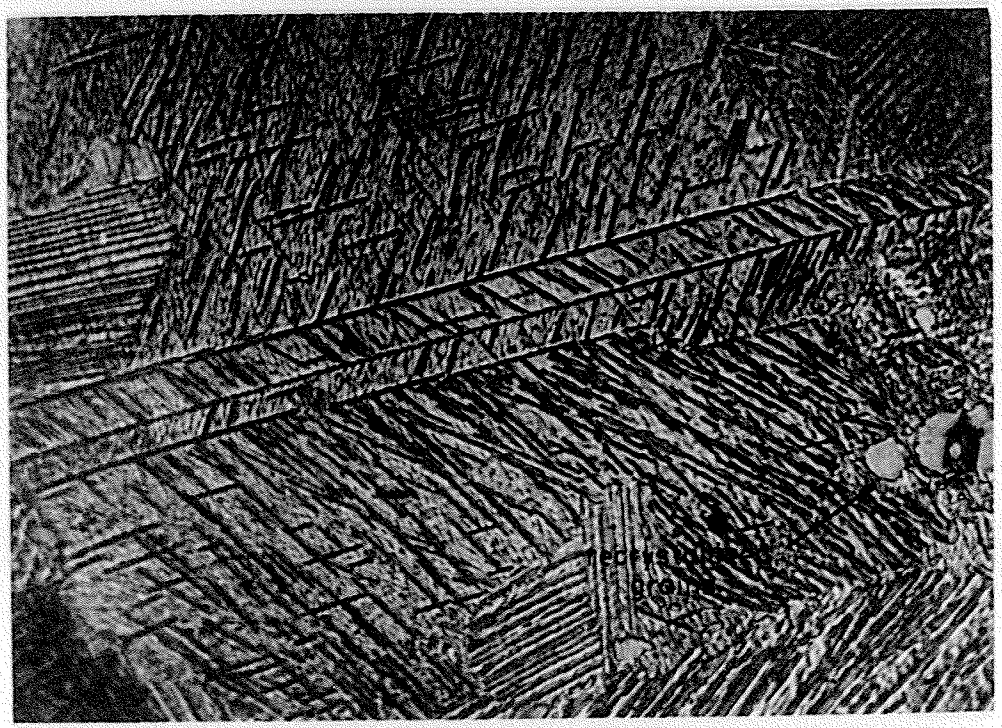

Fig. 42 Microstructure of 30% CR + 100 hr. at 800° C. (1560x)

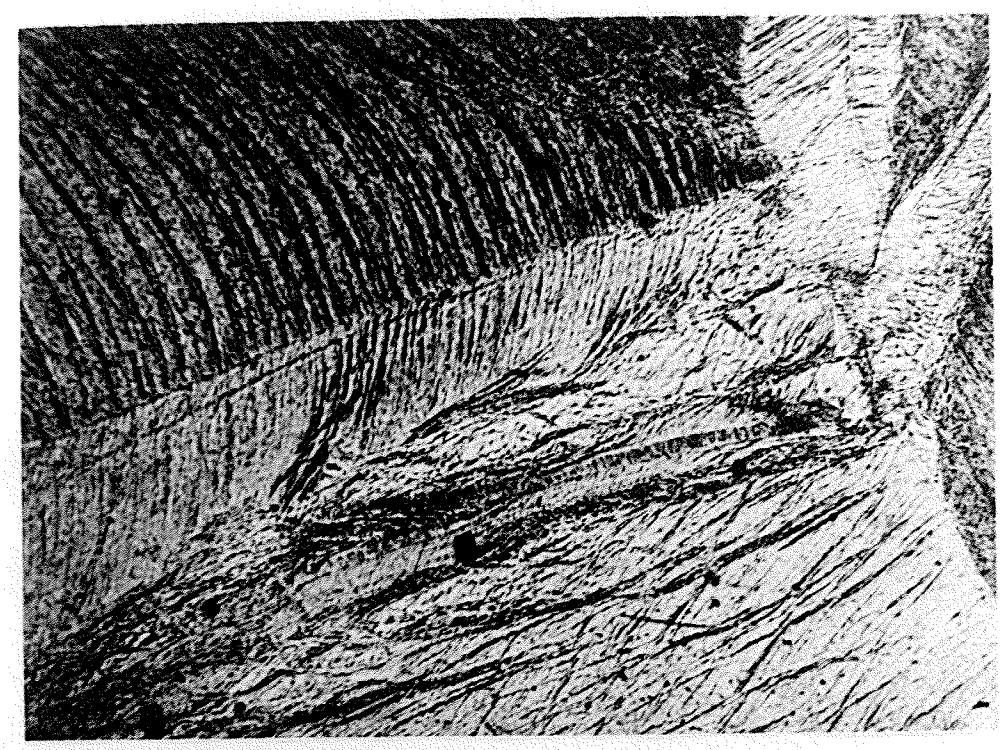

Fig. 43 Microstructure of as 60% CR. (420x)

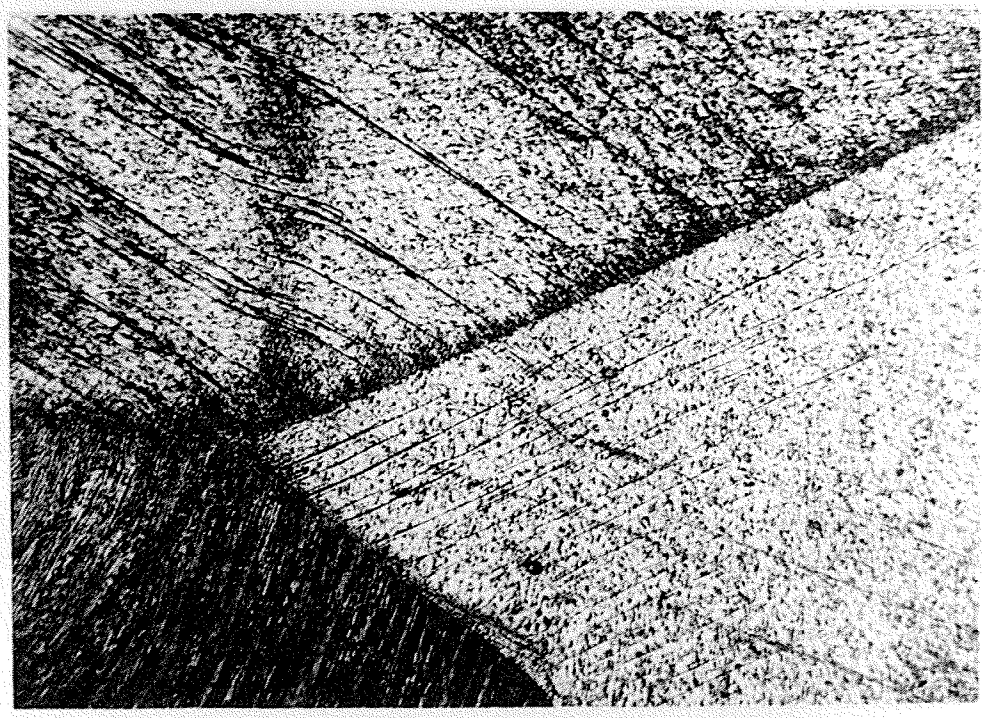

Fig. 44 Microstructure of 60% CR + 10 hr. at 800° C. (470x)

Fig. 45 Microstructure of 60% CR + 51 hr. at 800° C. (625x)

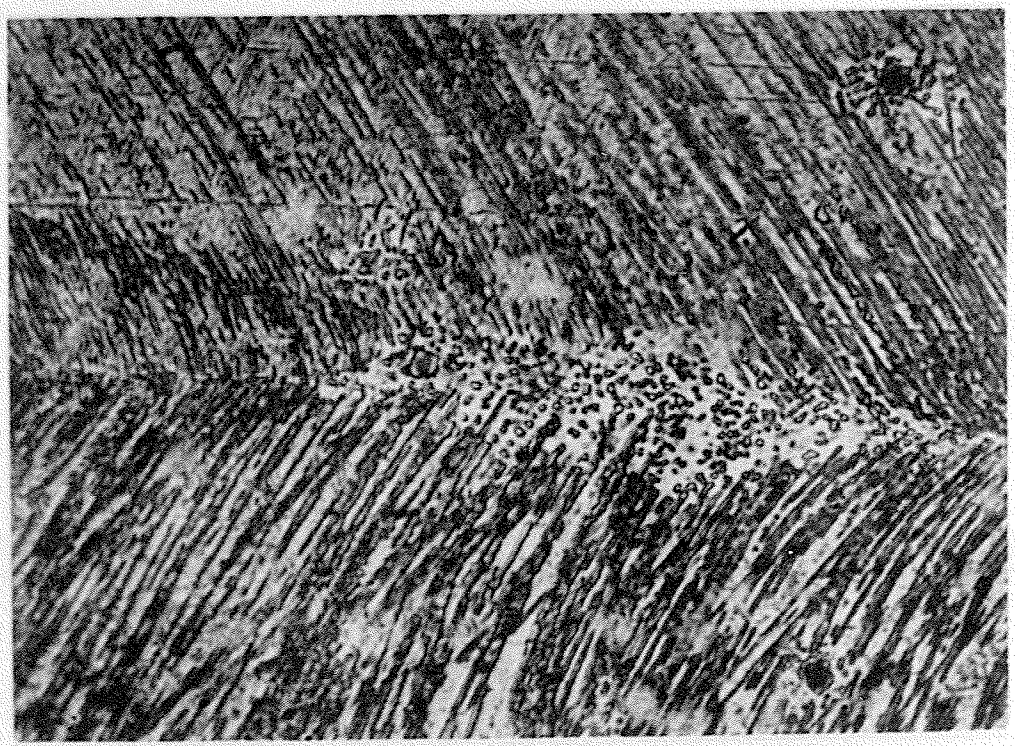

Fig. 46 Microstructure of 60% CR + 51 hr. at 800° C. (2340x)

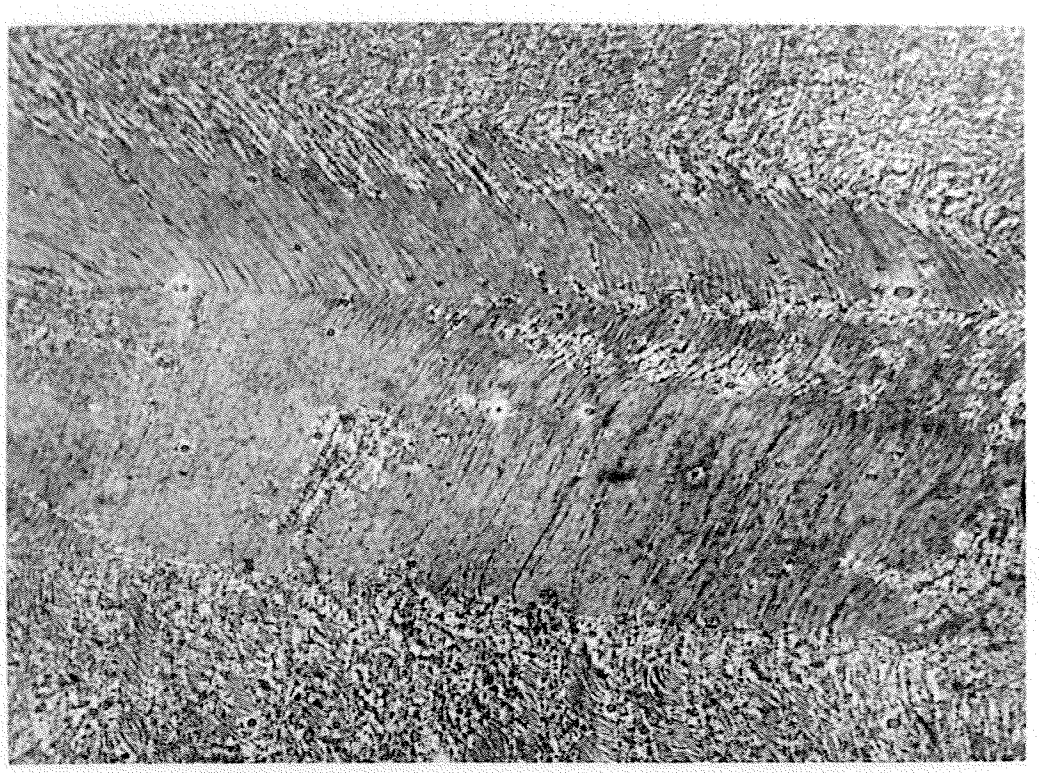

Fig. 47 Microstructure of 60% CR + 119 hr. at 800° C. (266x)

Fig. 48 Microstructure of 60% CR + 119 hr. at 800° C. (2340x)

as shown in Figures 47 and 48. The largest spheroidal particles present are about one micron in size and some of them can be seen in the process of coalescing. Near the boundary between the two areas, the particles occasionally appear to align with an imaginary extension of the striations. It was not possible to distinguish recrystallized grain boundaries in any area.

4.3 PRECIPITATE EXTRACTION AND X-RAY ANALYSIS

Electrochemical extraction of precipitate particles of the aged and deformed and aged conditions was done for the various aging treatments. Identification was carried out by the Debye-Scherrer X-ray film technique. The type of particle formed proved independent of the amount of prior deformation. The major precipitate matched the expected stable orthorhombic Ni_3Nb reported in the ASTM file,[82] with lattice parameters of a = 5.11 Å, b = 4.25 Å, c = 4.54 Å. Its reported space group of Pmmn indexed many observed reflections. However, some of these indexed reflections were not reported as visible on the file card for Ni_3Nb. In addition, NbC and $M_{23}C_6$ carbides with face centered cubic structures were also identified.

4.4 ELECTRON MICROSCOPY

4.4.1 Precipitate Extraction

The carbon extraction replica technique was used to study the precipitation process with the electron microscope. This method gave a verification of the types of precipitates observed previously by X-rays, and information concerning the size, shape, and distribution of the particles was also obtained.

The replica from lightly deformed material aged 10 hours revealed clusters of rod-shaped particles about 0.1 μ in length and identified by electron diffraction ring patterns as NbC. On aging for 54 hours, these particles grew to approximately 0.3 μ. A network of long (2 to 4.5 μ) intersecting particles, identified as orthorhombic Ni_3Nb, were also identified. Both types of particles are shown in Figure 49. This figure also shows a string of oblate spheroid particles, identified as $Cr_{23}C_6$, and are probably associated with a grain boundary. Aging for 100 hours does little to change the described microstructure, except to increase the density of long Ni_3Nb orthorhombic precipitates.

A prior cold work of 60% and aging for ten hours caused Ni_3Nb phase to precipitate out as long narrow particles in a direction seemingly parallel to the striations observed in the optical microstructure. Their shape is much more irregular than those particles observed in lightly deformed and aged specimen (Fig. 50). Also present are the rod-shaped NbC particles observed with a light prior deformation. The size of these are the same as those observed in the specimen lightly deformed and aged for 54 hours (0.3 μ, Fig. 51). Aging for 109 hours produces a cross-hatched network of Ni_3Nb precipitate, 2 to 3 μ in length, with a great majority of the particles aligning in one direction (Fig. 52). There are also present regions where Ni_3Nb precipitate is entirely in the form of distorted spheres, some of which appear to be in the process of coalescing (Fig. 53). This shape of precipitate ranges in size form 0.2 to 1.0 μ. There seems to be very little mixing of these precipitate morphologies, except in the region of transition from one to the other. There is an overall presence of NbC rod-shaped particles, about the same size as those observed with earlier aging time, but in reduced density.

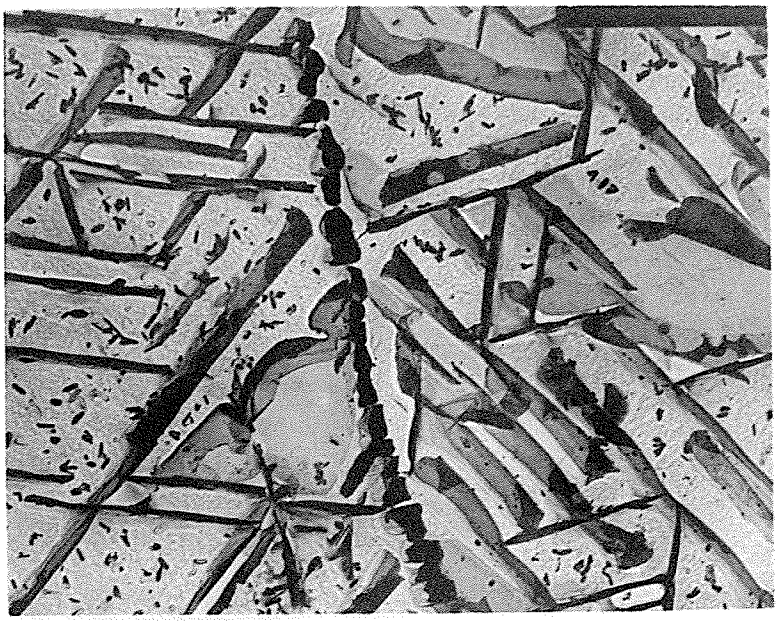

Fig. 49 Carbon extraction replica of 5% CR + 54 hr. at 800° C. (9,020x)

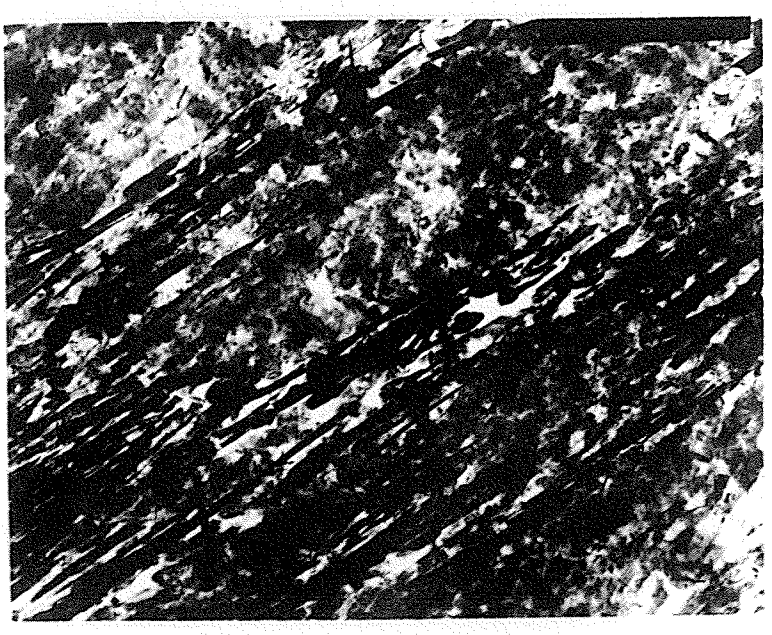

Fig. 50 Carbon extraction replica of 60% CR + 10 hr. at 800° C. (12,220x)

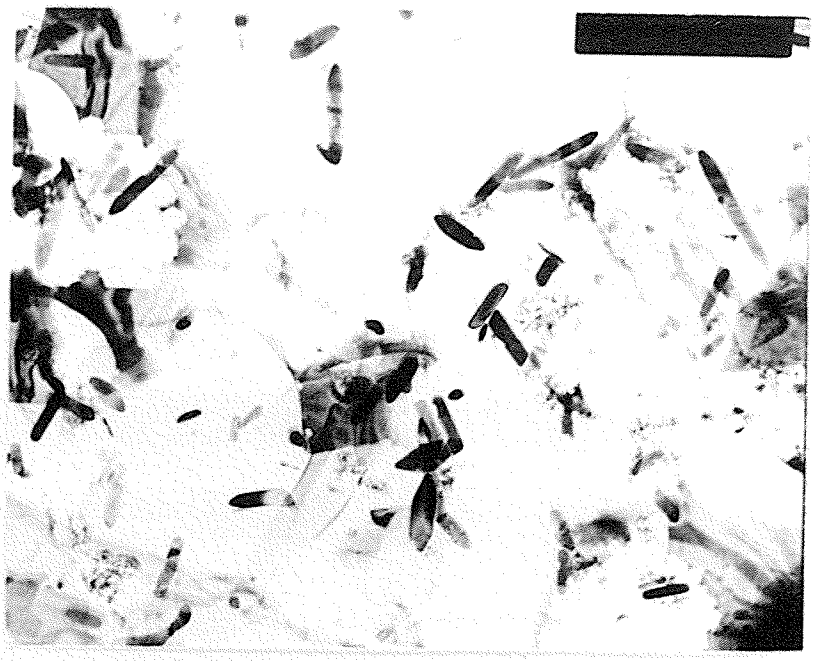

Fig. 51 Carbon extraction replica of 60% CR + 10 hr. at 800° C. (47,520x)

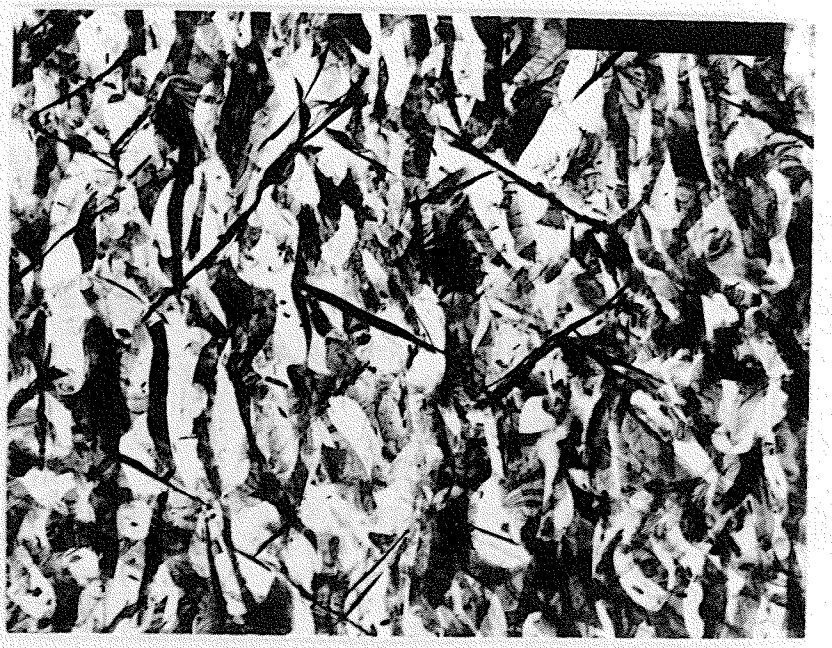

Fig. 52 Carbon extraction replica of 60% CR + 100 hr. at 800° C. (10,720x)

4.4.2 Thin Foil Electron Microscopy

Thin foils of the solution treated and the lightly, moderately, and heavily deformed specimens with pre and post aging treatment were prepared and examined. This work gave precise details of the structure of the deformed specimens and its effect upon microstructure formed by thermal treatments.

4.4.2.1 As Solution Treated

The standard anneal used for this alloy was six to ten hours at 1250° C. Foils examined revealed an FCC matrix with a lattice parameter of 3.565 Å. There appeared to be what at first was thought occasional stacking faults as shown in Figure 54. Trace analysis did establish that these were on (111) matrix planes. However, electron diffraction patterns and darkfield images (Fig. 55 and 56) demonstrated a crystal structure associated with these bands, apart from the matrix. Further analysis showed these areas to be thinly twinned regions. Detailed analysis is given in Appendix A.

4.4.2.2 As Deformed

With increasing amount of deformation, thin foils revealed a dislocation network taking on an increasing degree of tanglement. No definite cell structure was formed, even after heavy deformation, as shown in Figure 57. The most striking features of the deformed condition were the presence of long, parallel bands in the matrix. Examples of their appearance are given in Figures 58 - 63. This structure was observed in all foils and the density of which appeared to increase with deformation. Detailed analysis of the diffraction patterns identified them to be deformation twins. Analysis was the same as that followed for the solution treated

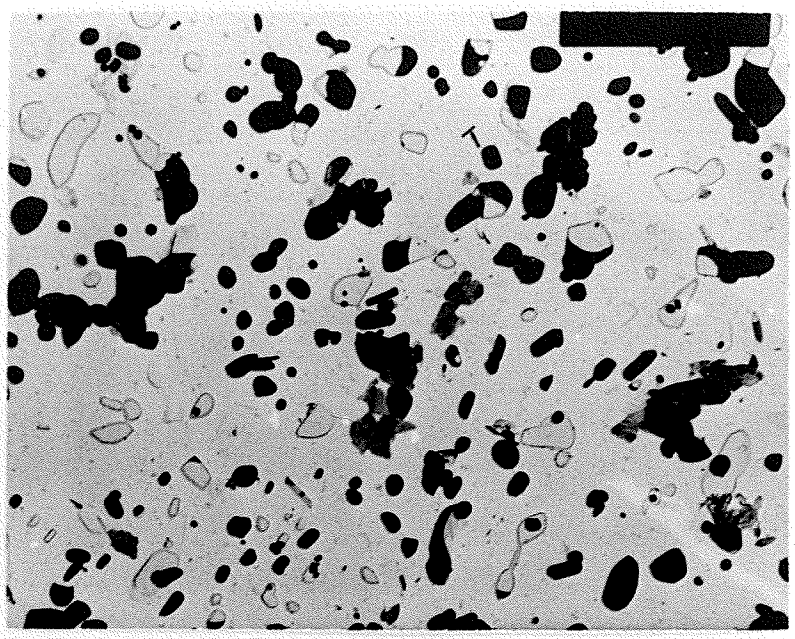

Fig. 53 Carbon extraction replica of 60% CR + 100 hr. at 800° C. (10,720x)

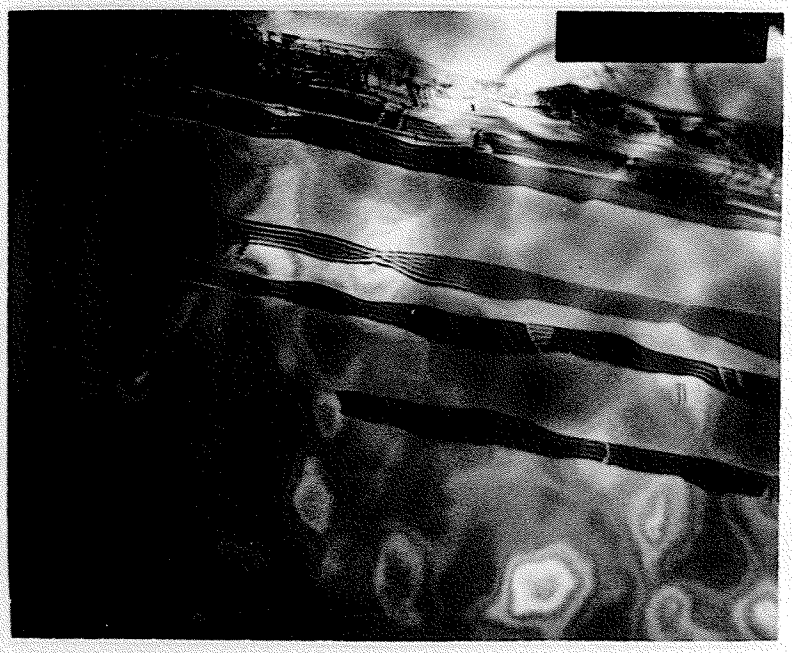

Fig. 54 Brightfield of as solution treated showing twin bands. (25,430x)

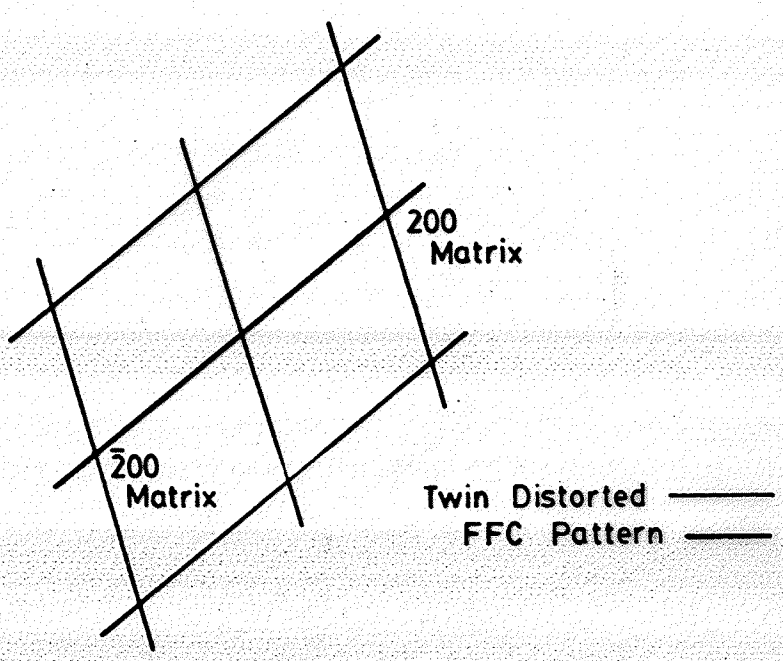
200
Matrix
$\bar{2}00$
Matrix
Twin Distorted
FFC Pattern

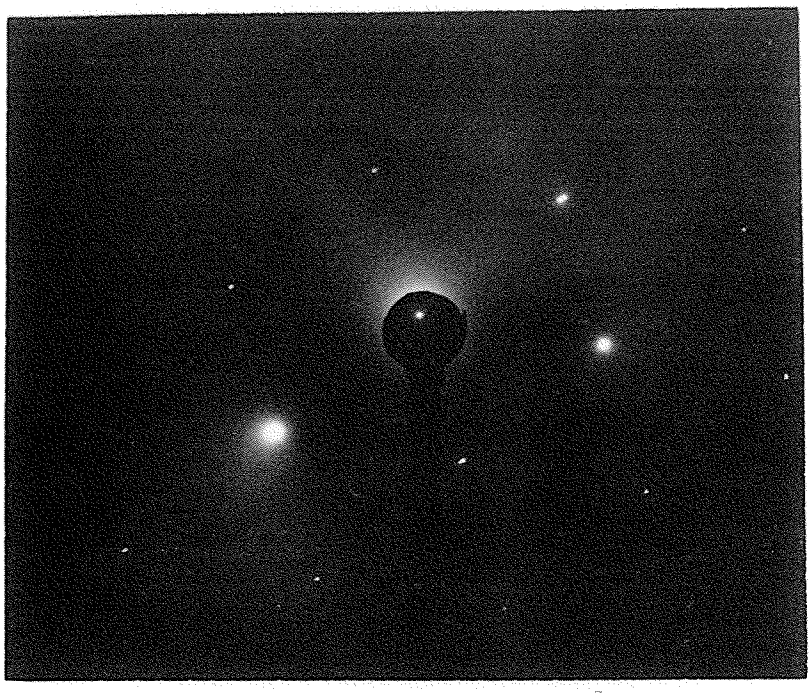

Fig. 55 SADP of band region in Fig. 54.

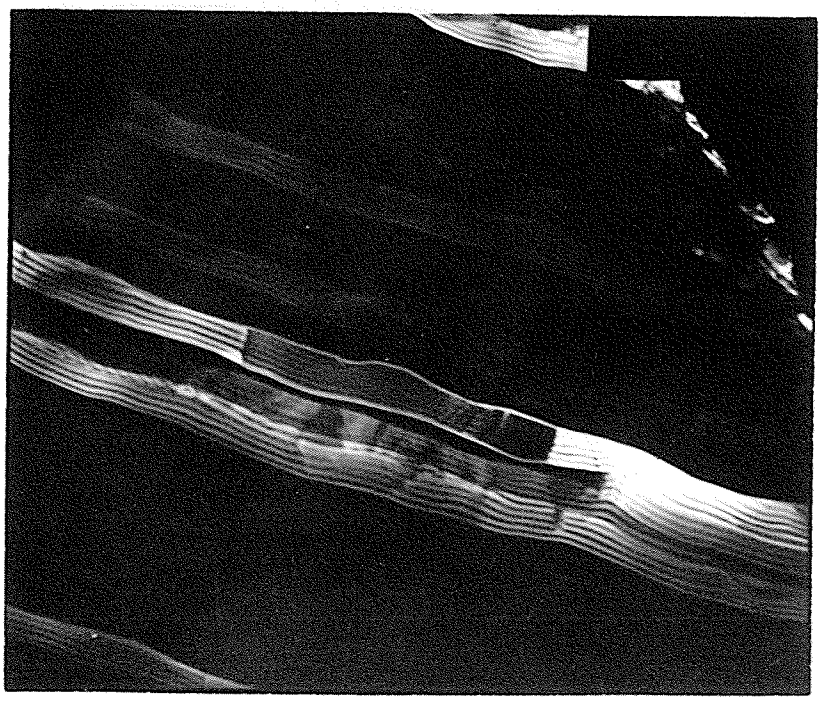

Fig. 56 Darkfield of Fig. 54. (30,370x)

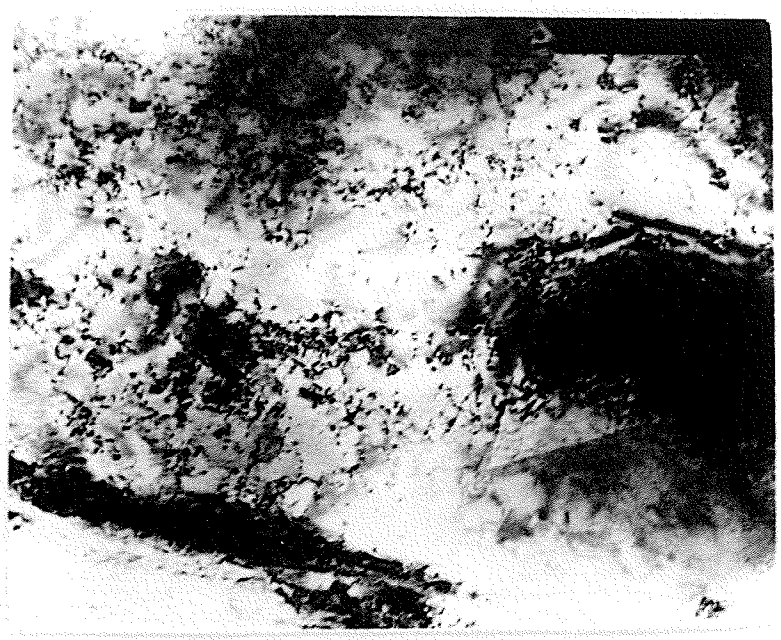

Fig. 57 Brightfield of 60% CR condition showing dislocation tanglement. (67,620x)

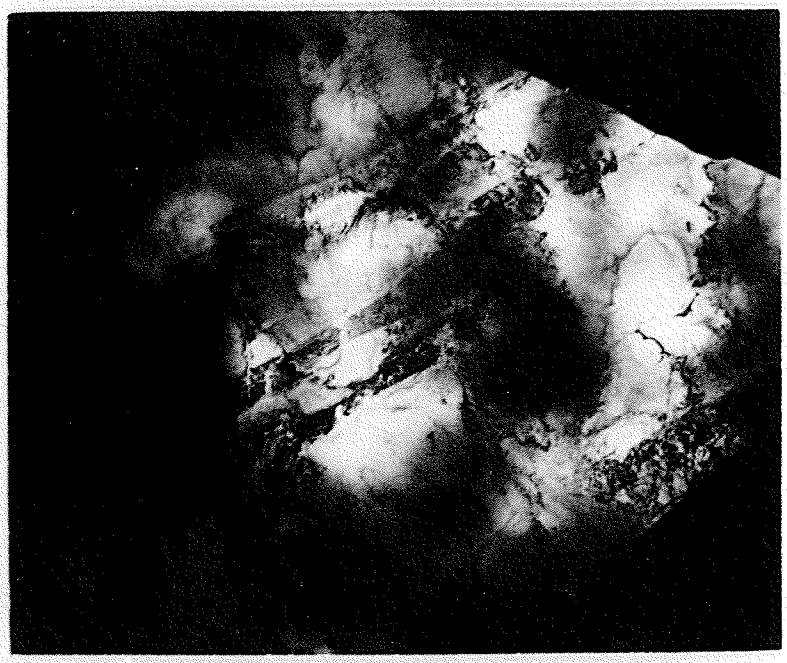

Fig. 58 Brightfield of 5% CR condition showing twin bands (30,370x)

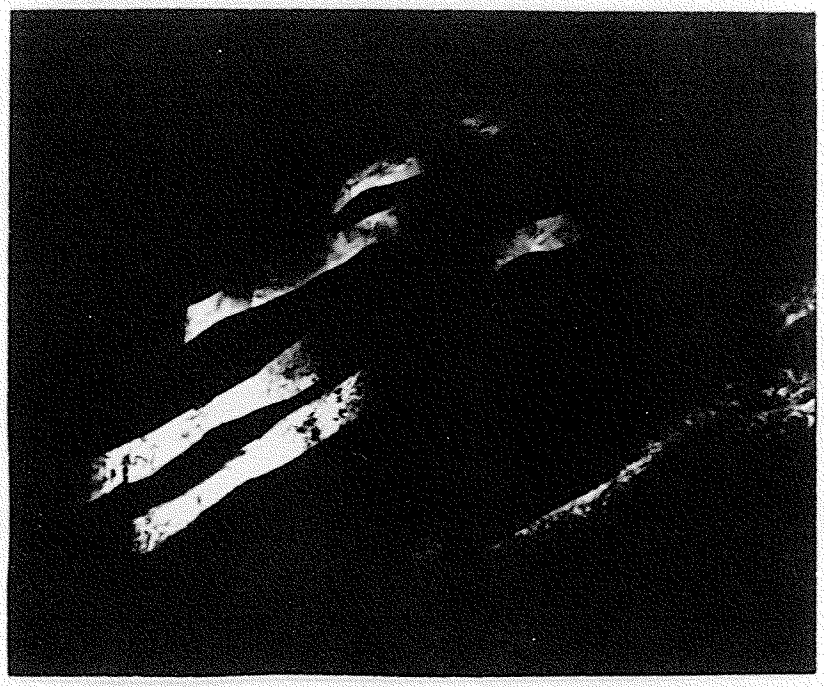

Fig. 59 Darkfield of Fig. 58. (30,370x)

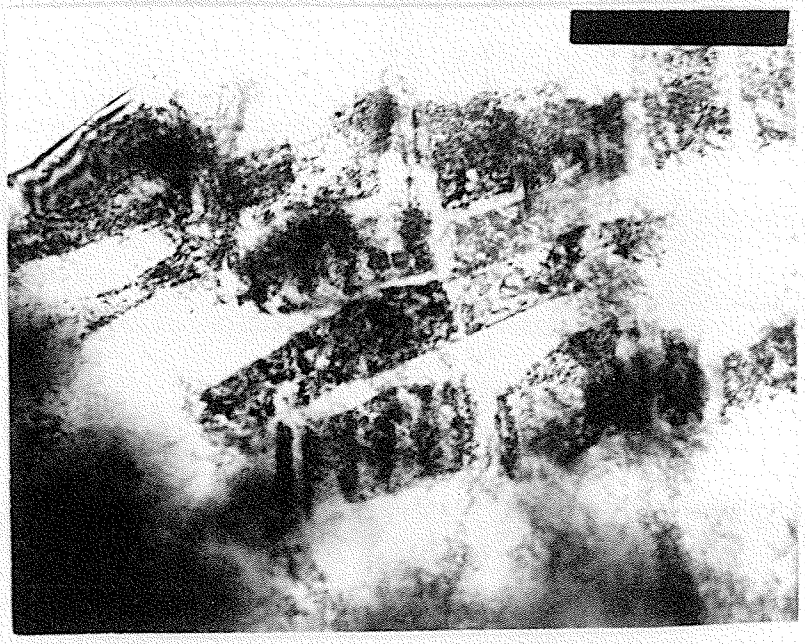

Fig. 60 Brightfield of as 30% CR showing twin bands. (37,510x)

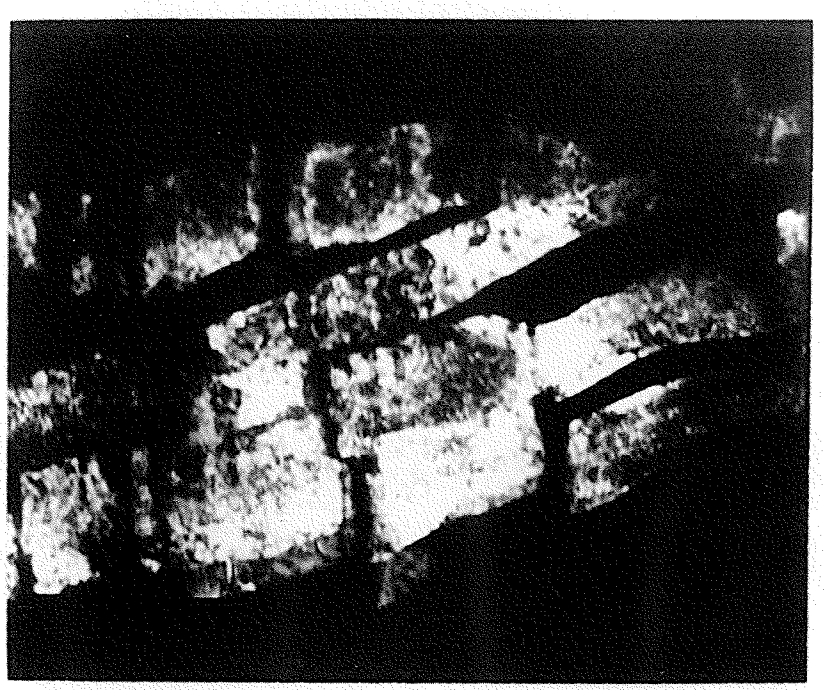

Fig. 61 Darkfield of Fig. 60. (37,510x)

Fig. 62 Brightfield of as 60% CR showing stepped twin bands. (30,370x)

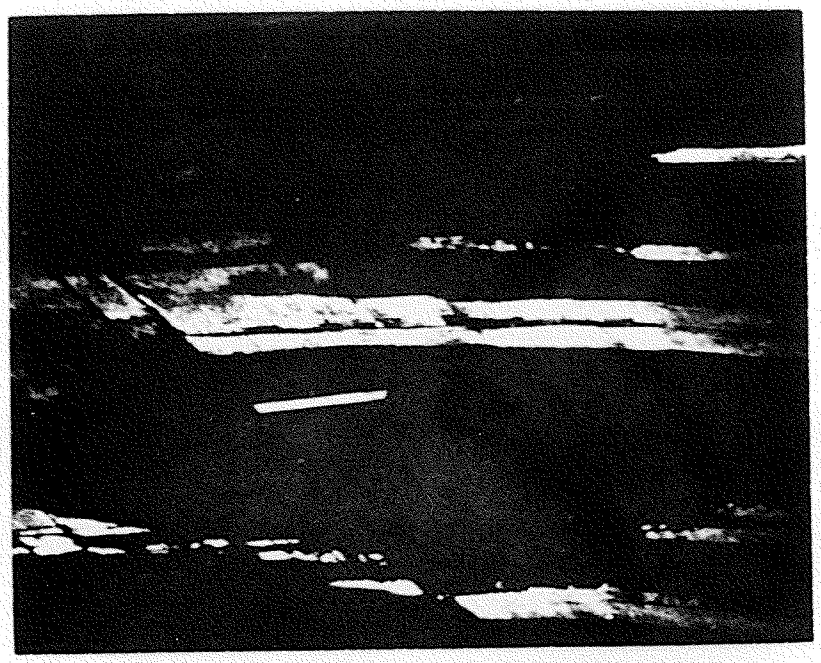

Fig. 63 Darkfield of Fig. 62. (30,370x)

Fig. 64 Brightfield of 5% CR + 50 hr. at 800° C showing Ni_3Nb plate precipitate. (19,070x)

specimen. This included the superposition of matrix and twin FCC diffraction patterns, the description of anomalous diffraction patterns as distorted FCC twin patterns due to thiness of twins, and the matching of normal FCC twin pattern with FCC matrix patterns at some relative degree of tilt. This is given in Appendix A.

4.4.2.3 Aging of the Lightly Deformed Material

Aging precipitated out two sizes of particles. The smaller set were of the order of 0.10 μ after 100 hours and could not be identified with electron diffraction. However, their shape and size were similar to NbC particles observed with carbon extraction replica techniques. The second set of particles appeared as long plates whose diffraction patterns were identified as those due to orthorhombic Ni_3Nb phase with a = 5.11 Å, b = 4.25 Å, c = 4.54 Å. A typical width of these precipitates was 0.05 μ and a length of 2.5 μ, which did not vary much by aging over 25 hours. Brightfield images of these particles are shown in Figures 64 and 65, with an Ni_3Nb-matrix electron diffraction pattern in Figure 66. Trace analysis established that the orthrhombic precipitates lie on (111) matrix planes. Occasionally, even after 100 hours of aging, deformation twins, whose diffraction symmetry was similar to those observed in the as deformed condition, were also seen (Fig. 67). It was only possible to distinguish between twinned regions and precipitates by electron diffraction, as both were identical in appearance in brightfield.

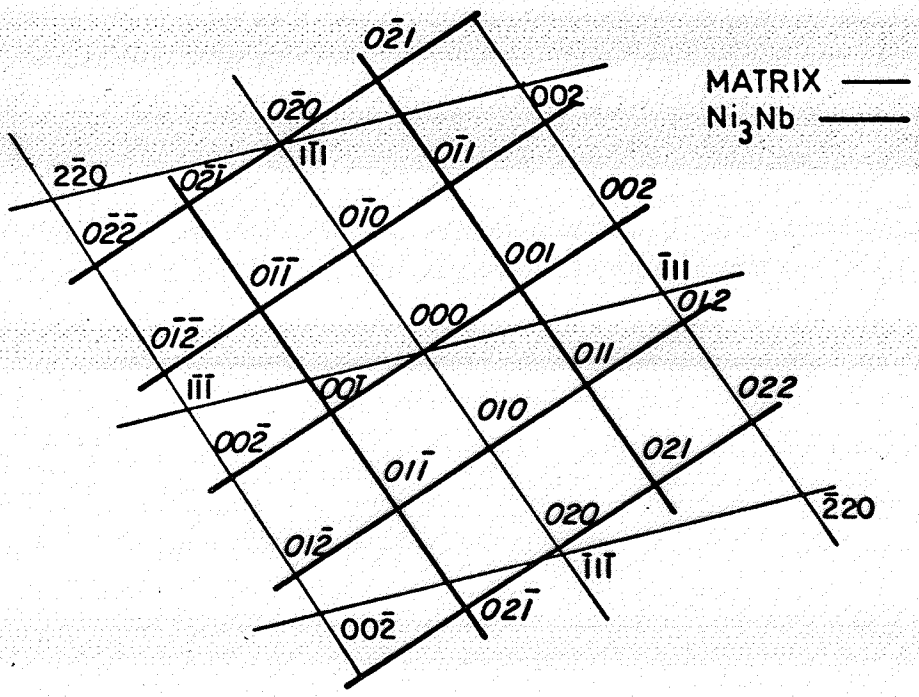
MATRIX
Ni_3Nb
$0\bar{2}1$
$0\bar{2}0$
002
$2\bar{2}0$
$02\bar{1}$
$1\bar{1}1$
$01\bar{1}$
$02\bar{2}$
$01\bar{0}$
002
$01\bar{1}$
001
$\bar{1}11$
$01\bar{2}$
000
012
$1\bar{1}\bar{1}$
001
011
022
$00\bar{2}$
010
$11\bar{1}$
021
020
$\bar{2}20$
$01\bar{2}$
$\bar{1}1\bar{1}$
$00\bar{2}$
$02\bar{1}$

Fig. 65 Brightfield of 5% CR + 109 hr. at 800° C showing small NbC particles. (37,510x)

Fig. 66 SADP of long precipitate in Fig. 64 indexed as Ni_3Nb.

4.4.2.4 Aging of the Moderately Deformed Material

Aging for ten hours does little to change the dislocation structure of the as deformed specimen. However, the diffraction patterns did not provide any evidence for the presence of deformation twins. Instead, long precipitates of Ni_3Nb having the brightfield appearance of the initial deformation twins were seen. This is shown in Figures 68 and 69. With an aging time of up to 50 hours, the number of Ni_3Nb precipitates increase, forming an intersecting network (Fig. 70).

As with lightly deformed material after 50 hours of aging, there is present a second set of unidentified particles which are of the order of 0.1 μ (Fig. 71). The dislocation density seemed to diminish slightly with aging, but no clear dislocation substructure or recrystallized grains appeared after 100 hours.

Trace analysis of the structure of the lightly and moderately deformed material has established that precipitation of Ni_3Nb occurs on (111) matrix planes. The orientation relationship between matrix and precipitate was observed to be as follows:

$$(010)\ Ni_3Nb\ //\ \{111\}\ FCC$$
$$[100]\ Ni_3Nb\ //\ \langle 110\rangle\ FCC$$

Initially, in the moderately deformed case, precipitation seems restricted to a single (111) plane in the same manner as deformation twinning was in the cold worked state. On further aging to 50 hours, precipitation occurs on other (111) planes forming an intersecting network. The sudden disappearance of deformation twin structure happens with little change in

Fig. 67 Brightfield of 5% CR + 25 hr. at 800° C showing a deformation twin. (47,520x)

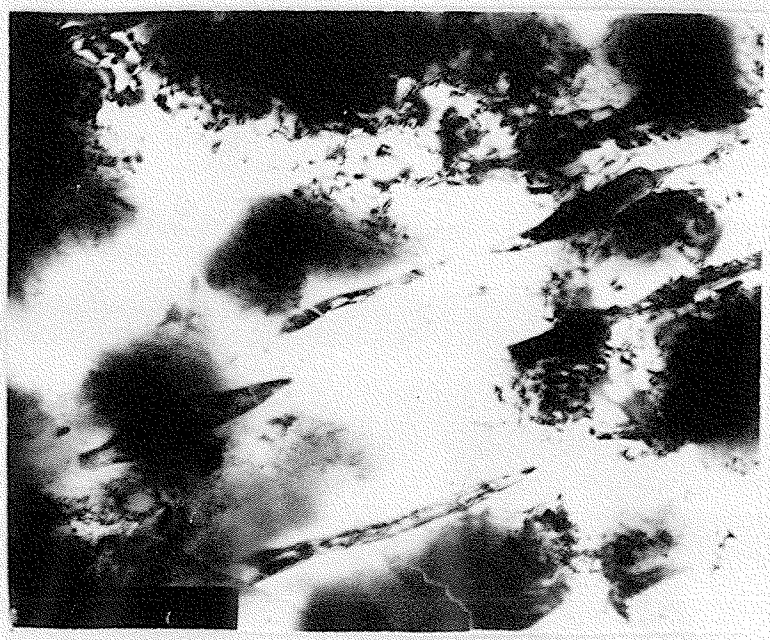

Fig. 68 Brightfield of 30% CR + 10 hr. at 800° C showing Ni_3Nb precipitates. (30,370x)

Fig. 69 Darkfield of Fig. 68. (30,370x)

Fig. 70 Brightfield of 30% CR + 50 hr. at 800° C showing intersecting Ni_3Nb precipitates. (19,010x)

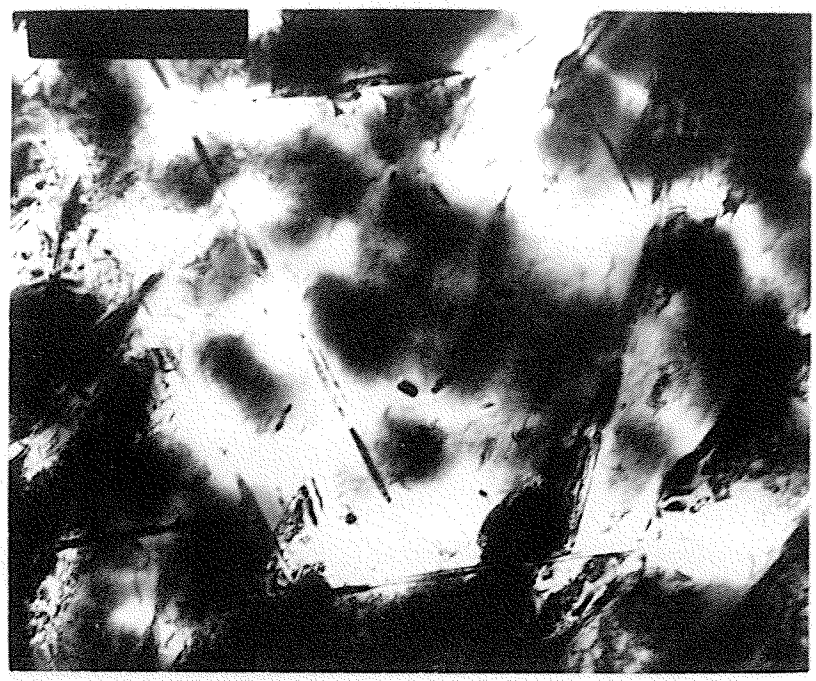

Fig. 71 Brightfield of 30% CR + 50 hr. at 800° C showing intersecting Ni_3Nb precipitates and smaller NbC particles. (47,520x)

Fig. 72 Darkfield of 60% CR + 10 min. at 800° C showing precipitate nucleation. (112,550x)

overall dislocation distribution, and with the simultaneous appearance of Ni_3Nb of similar shape and habit. This seems to suggest the former twin-matrix interfaces act as nucleation sites for initial precipitation of Ni_3Nb.

4.4.2.5 Aging Of the Heavily Deformed Material

Precipitation in 60% cold rolled material was observed after aging only ten minutes at 800° C (Fig. 72). It was not possible to establish conclusively the type of precipitate formed at this early stage. After 20 minutes of aging time, precipitation was observed to be clearly nucleating at the interfaces of deformation twin and the matrix. This is shown in Figures 73 to 76. Figure 76 is the selected area diffraction pattern of matrix-twin area in Figure 75. The normal coherency of a (011)/(011) matrix-twin diffraction pattern is altered by precipitation at the interface. This is apparent in that the (011) twin patterns are rotated slightly with respect to each other such that their normally common (111) planes are no longer parallel. In Figure 75, a few rod-shaped precipitates between the deformation twin band areas are also observed.

Areas having undergone recrystallization were also observed after only 20 minutes aging. They were characteristically free of dislocations and contained distorted sphere-shaped particles ranging in size from 50 to 1450 Å (Fig. 77). The extent of recrystallization increased with aging time, but was not complete even after 100 hours at 800° C. The morphology of the particles in recrystallized areas tends towards a spheroidal shape with increasing aging time and are between 2000 - 4000 Å in size after 100 hours, as shown in Figure 78. These particles were identified as

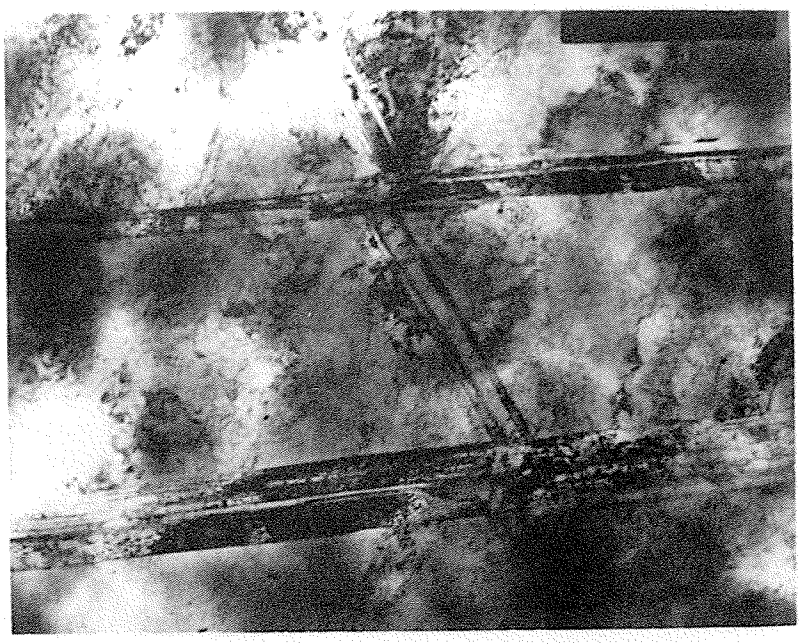

Fig. 73 Brightfield of 60% CR + 20 min. at 800° C showing intersecting deformation twin bands. (30,370x)

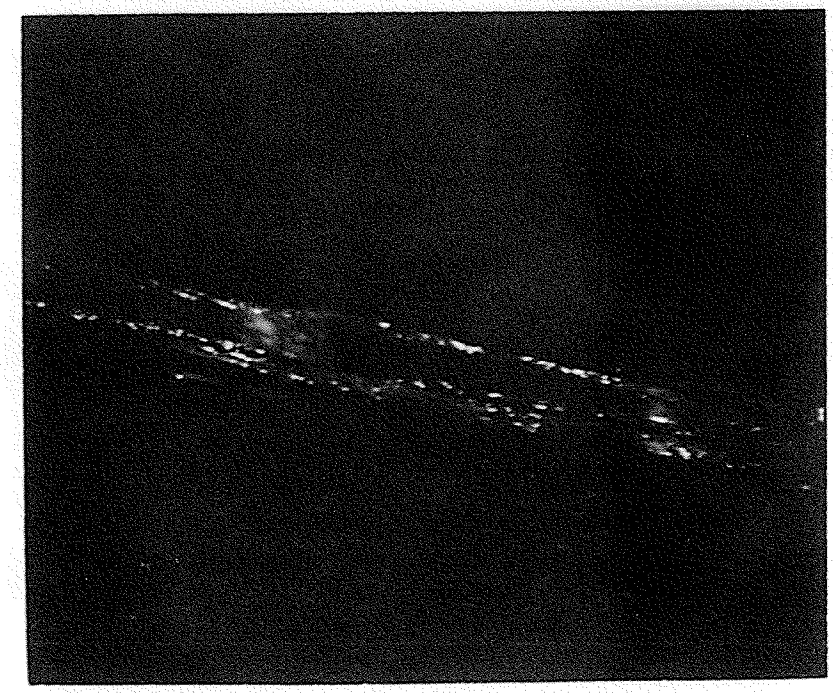

Fig. 74 Darkfield of Fig. 73 showing precipitate formation at twin matrix interface. (55,860x)

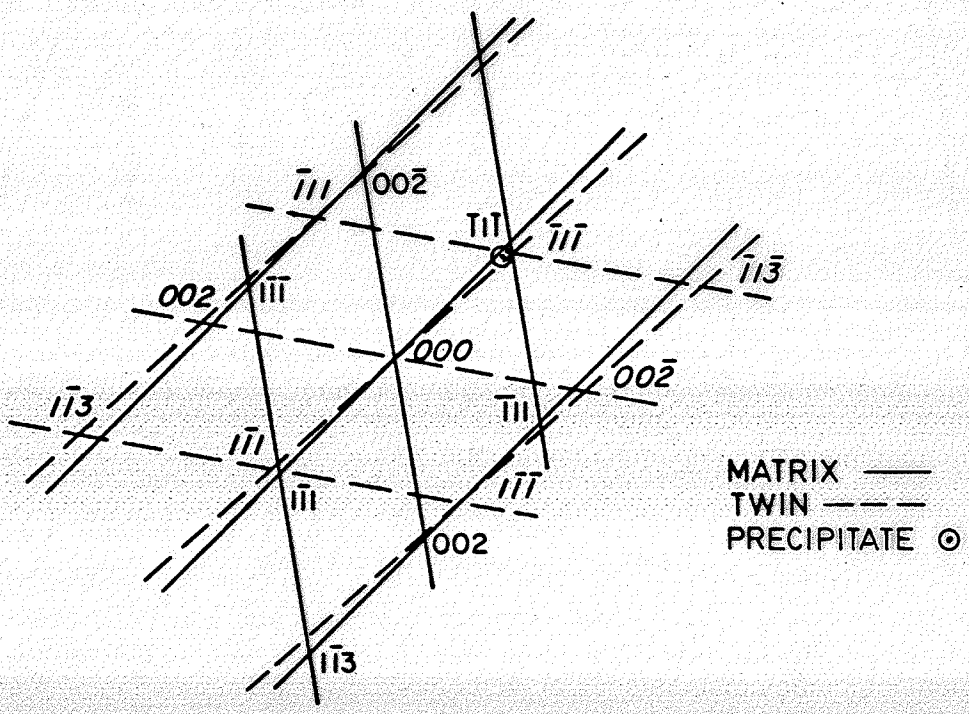
$\bar{1}11$
$00\bar{2}$
$\bar{1}\bar{1}\bar{1}$
$\bar{1}11$
$\bar{1}\bar{1}\bar{3}$
002
$\bar{1}\bar{1}\bar{1}$
000
$00\bar{2}$
$\bar{1}\bar{1}\bar{3}$
$\bar{1}11$
$\bar{1}11$
$\bar{1}\bar{1}\bar{1}$
002
$\bar{1}\bar{1}3$
MATRIX
TWIN
PRECIPITATE ⊙

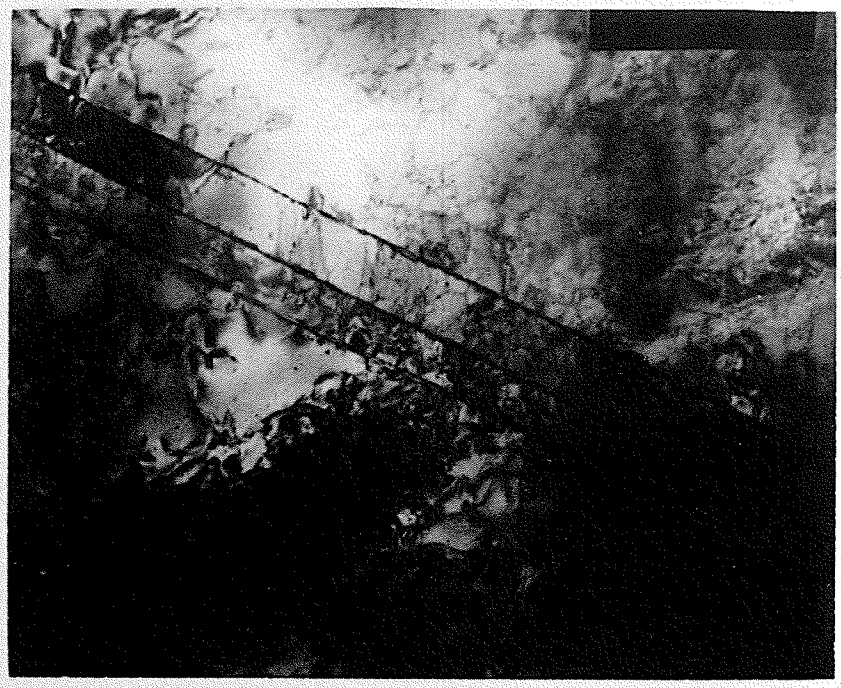

Fig. 75 Brightfield of 60% CR + 20 min. at 800° C showing precipitates at interface of adjacent twin bands and matrix. (85,040x)

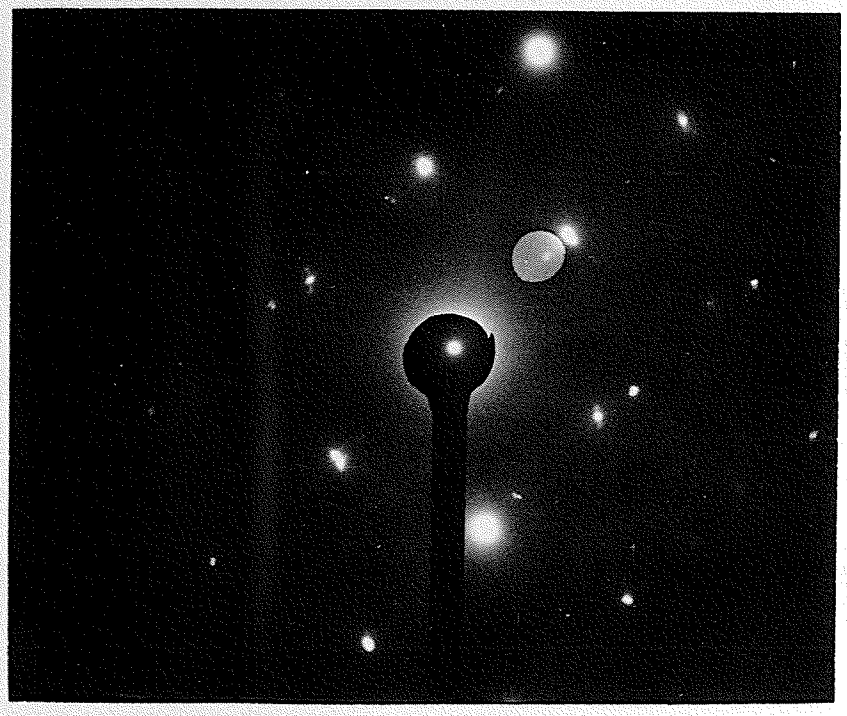

Fig. 76 SADP of twin area in Fig. 75 showing a loss in coherency between twins with precipitation at interface.

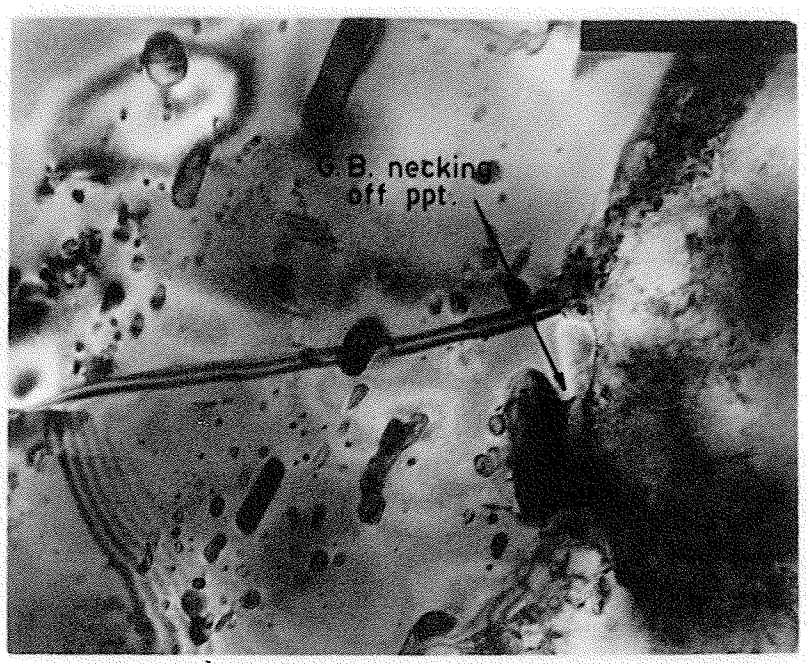

Fig. 77 Brightfield of 60% CR + 20 min. at 800° C showing recrystallized region bordering on cold worked region. Note varied size of oblate spheroidal precipitate in recrystallized area. (55,860x)

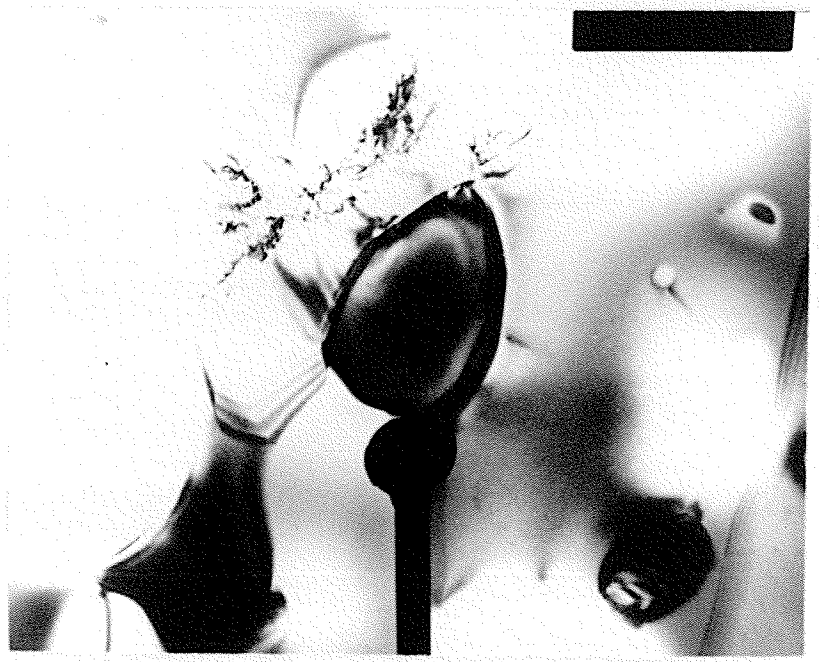

Fig. 78 Brightfield of 60% CR + 100 hr. at 800° C showing spheroidal shaped Ni_3Nb precipitate. (55,860x)

orthorhombic Ni_3Nb after all aging treatments. In addition to nucleation sites for precipitation, the deformation twin interfaces were also observed to serve as nucleation sites for recrystallized grains (Fig. 79).

Plate-shaped precipitate, similar to those observed in lightly and moderately deformed specimens, appeared in the non-recrystallized regions of the matrix after only two hours at 800° C (Fig. 80). This observation was made at all aging times up to 100 hours and the particles were identified as orthorhombic Ni_3Nb phase. After ten hours, the length of this precipitate ranged from 0.1 μ to 4μ.

Plate-shaped Ni_3Nb also occurred in the recrystallized areas of the matrix, but not until it was also observed in cold worked regions. A particularly interesting example after two hours is shown in Figures 81 - 83, where recrystallized matrix between parallel plate precicitate has a twin orientation relationship.

The recrystallization front between cold worked regions and recrystallized areas gave some interesting observations. In Figure 84, there is an extensive Morié fringe contrast in the cold worked side of the front. Together with selected area diffraction and darkfield technique, this seems to be associated with the formation of spheroidal-shaped Ni_3Nb. Also in this figure, it is observed what appears as the necking of a precipitate by the recrystallization front. In areas well removed from the recrystallized regions, in addition to major plate-type Ni_3Nb particles, occasionally small spheroidal-shaped particles were also observed, but never to the extent and size as those observed in recrystallized regions after only a few hours of aging (Fig. 85).

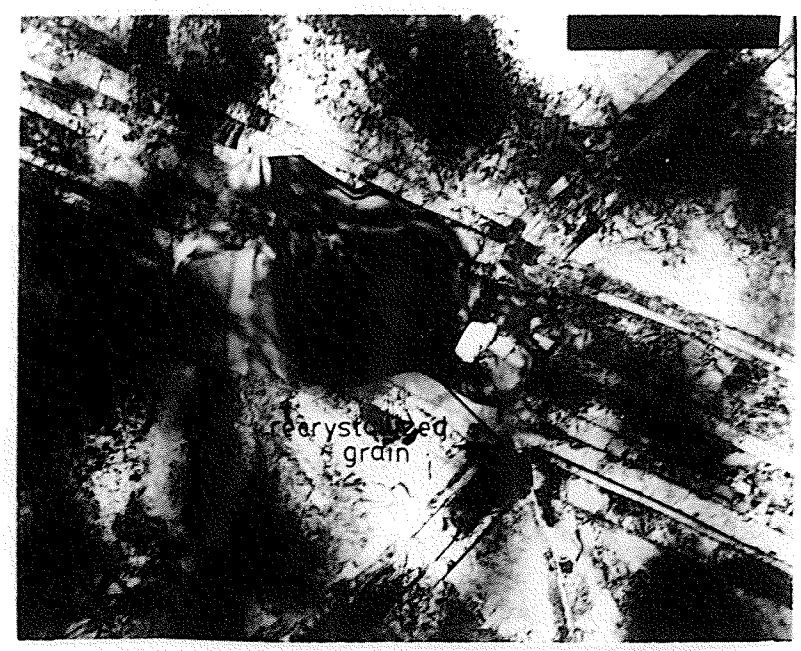

Fig. 79 Brightfield of 60% CR+ 1 hr. at 800° C showing nucleation of recrystallized grain in twin band areas. (37,510x)

Fig. 80 Brightfield of 60% CR + 2 hr. at 800° C showing plate shaped Ni_3Nb precipitate in cold worked region of matrix. (37,510x)

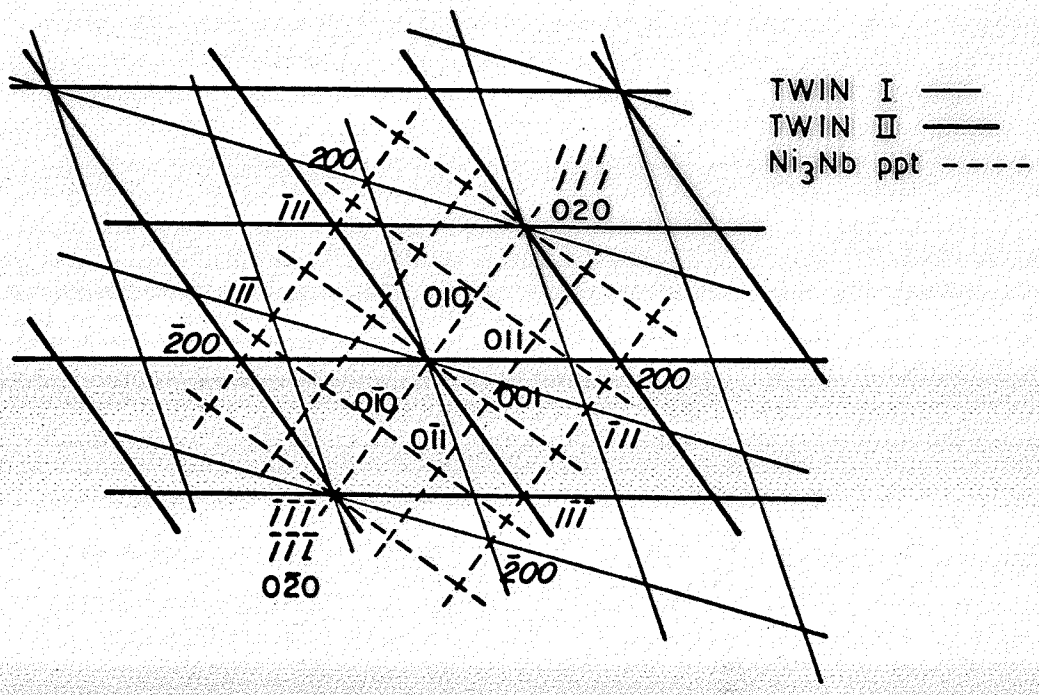
TWIN I
TWIN II
Ni3Nb ppt
200
111
020
111
010
111
011
200
200
001
010
011
111
111
111
020
200

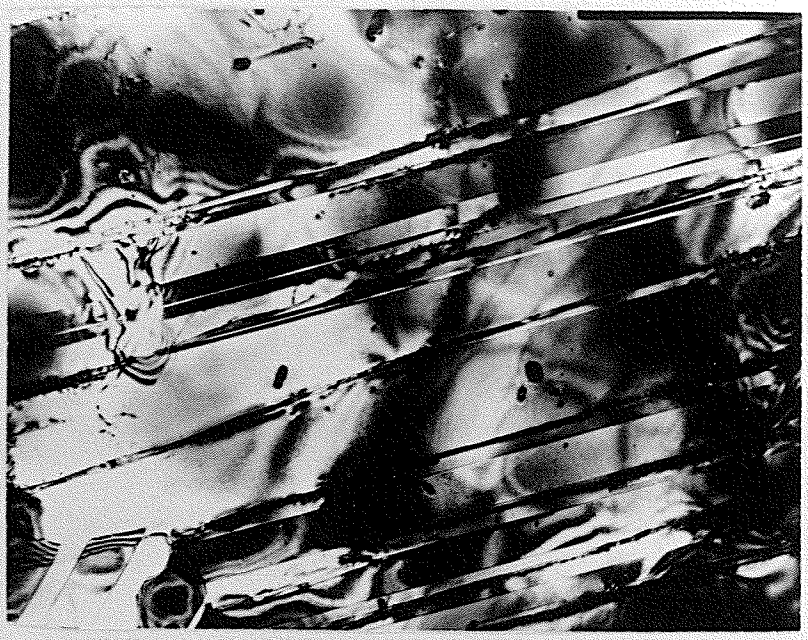

Fig. 81 Brightfield of 60% CR + 20 hr. at 800° C. Shows recrystallized twin regions with Ni_3Nb precipitates near interfaces. (30,370x)

Fig. 82 SADP of Fig. 81 showing twin orientation of $(011)_{T1}$ // $(011)_{T2}$ and Ni_3Nb precipitate.

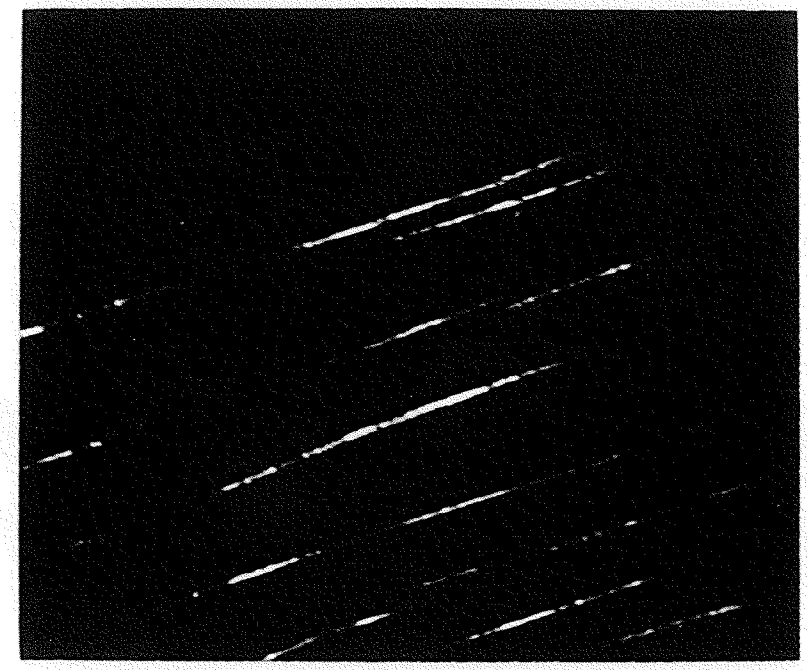

Fig. 83 Darkfield of Fig. 81 showing Ni_3Nb precipitate at interface of twins. (30,370x)

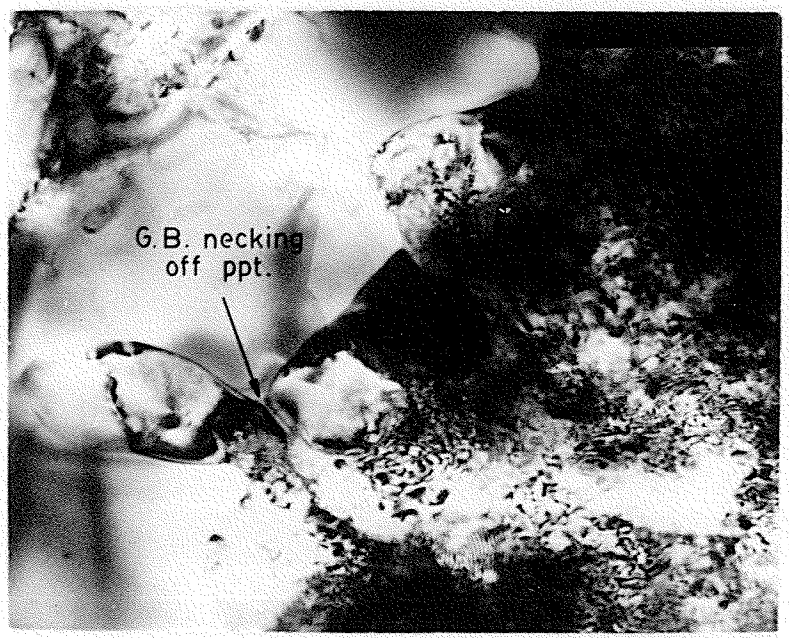

Fig. 84 Brightfield of 60% CR + 2 hr. at 800° C showing precipitation at recrystallization front and Morié fringe pattern. (67,620x)

The dislocation substructure occasionally appeared to take on a cell network in the early stages of aging, as shown in Figure 75, but generally changed relatively little except for complete obliteration in recrystallized areas.

Aging of heavily deformed material was also carried out at a higher temperature of 850° C. After ten hours, complete recrystallization of the matrix had occurred with orthorhombic Ni_3Nb precipitate present both in the form of plates and distorted spheres. Figure 86 indicates a tendency for the latter towards a row arrangement. Figure 87 is a high magnification micrograph of this row effect and shows particle agglomeration in progress. Aging for 20 hours at 850° C increased the amount of plate-like Ni_3Nb, while the spheroidal type did not seem to change (Fig. 88 and 89).

As a final note to electron microscopy results, the indexing of orthorhombic Ni_3Nb precipitate mainly followed the reflecting conditions of space group Pma2, independent of particle shape and aging treatment (Appendix B). The orientation relationship between plate Ni_3Nb and matrix was observed to be:

(010) Ni_3Nb // {111} MATRIX

[100] Ni_3Nb // <110> MATRIX

in cold worked and recrystallized regions alike. However, no such specific relationship seems to exist for distorted sphere-shaped Ni_3Nb in the recrystallized area of heavily deformed and aged material.

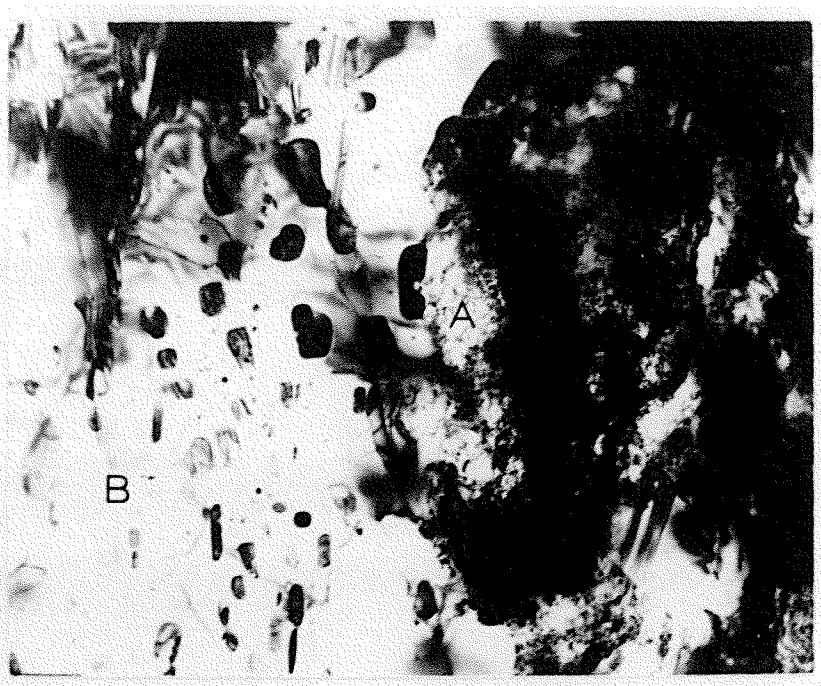

Fig. 85 Brightfield of 60% CR + 2 hr. at 800° C showing various sizes of precipitate in the recrystallized region. (25,430x)

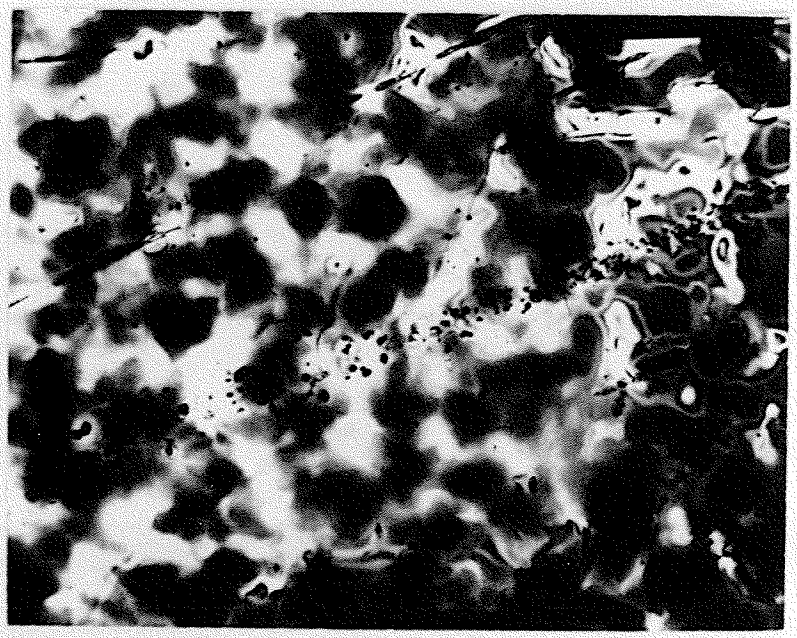

Fig. 86 Brightfield of 60% CR + 10 hr. at 850° C showing plate shaped precipitates and oblate spheroidal precipitates aligned in rows. (12,670x)

Fig. 87 Brightfield of 60% CR + 10 hr. at 850° C showing process of agglomeration of oblate spheres. (112,540x)

Fig. 88 Brightfield of 60% CR + 20 hr. at 850° C showing plate Ni_3Nb and rows of spheroidal precipitates. (10,720x)

Fig. 89 Same as Fig. 88 with magnification of 47,520x.

CHAPTER 5 DISCUSSION

The following discussion of experimental results is broadly divided into a discourse on the effect of deformation on the material in the supersaturated solid solution state, and on the results of aging in this state.

To begin with, it is necessary to consider the close relationship between deformation twinning and martensitic transformation. The former is a mode of plastic deformation and occurs as a result of applied stress, while the latter is a basic type of phase transformation where applied stress has only a secondary importance. Both can be classified under the descriptive terminology used by Christian,[38] of a military reaction in which the product is formed by atomic movements which are highly disciplined, coordinated, and depend on one another. This is opposed to a civilian reaction which is characterized by long range transportation of atoms involving diffusion in the case of phase transformation, and movement on relatively few atomic planes (slip) in the case of plastic deformation. In martensitic transformation, there is an orderly arrangement of atoms from one crystal structure to another, while in twinning, this realignment produces the original crystal structure but with a new orientation. The main experimental criterion used to determine these reactions is the change in shape of the parent volume distorting the surrounding matrix. The changes in shape are quite similar so that martensite and deformation twins look alike, taking the form of small lenses or plates.

Cobalt is an allotropic metal, having HCP crystal structure at room temperature and an FCC structure at high temperature. It is well established[83]

that the transformation is martensitic in nature. Much work has been done to establish the physical characteristics of this transformation in pure Co and Co-Ni alloys.[83-98] Upon cooling, it is suppressed by the addition of Ni to below room temperature,[90] but can be induced by mechanical deformation. Work on a group of Co-Ni base alloys, called MP alloys,[99,100,101] has shown that a stress-induced transformation acts as a strengthening mechanism. In these alloys, the total composition of Co and Ni is 70% and the thermal stability of the CPH phase is shown in Figure 90. One alloy in particular, MP35N, has a composition very similar to the alloy used during present investigations; that is, 35% Co, 35% Ni, 20% Cr, 10% Mo versus 40% Co, 38% Ni, 17% Cr, and 5% Nb.

In the cold worked condition, the optical microstructure of both these alloys are very similar (Fig. 43 and 91) with fine parallel striations on two or more sets of {111} planes. By X-ray and electron microscopy investigation, Graham and Youngblood[100] established that the striations were thin platelets of CPH structure and mechanical twins formed by cold deformation. Initially, the same explanation was thought to account for the similar structure of our alloy. However, the presence of the hexagonal phase could not be confirmed, and the striations were found to be the result of mechanical twinning only. These twins are easily distinguished from annealing twins which are orders of magnitude larger (Fig. 35). Some mechanical size twins were found in the annealed state, but their existence was probably due to the mishandling of the foil before examination in the electron microscope.

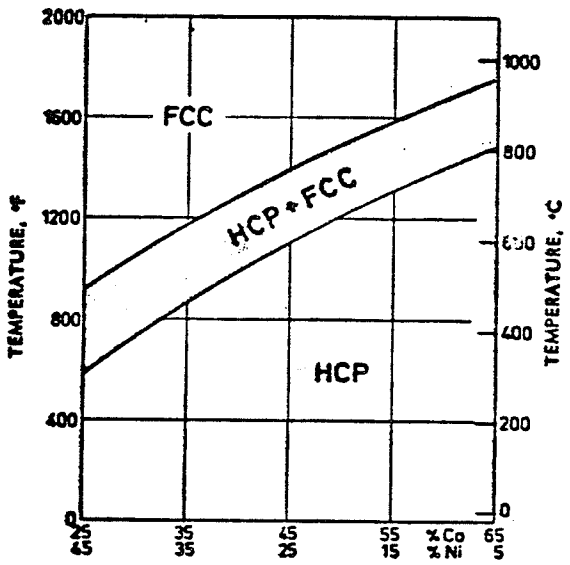

Fig. 90 Structural diagram for multiphase alloys containing 20% Cr, 10% Mo, 70% Ni + Co, [101].

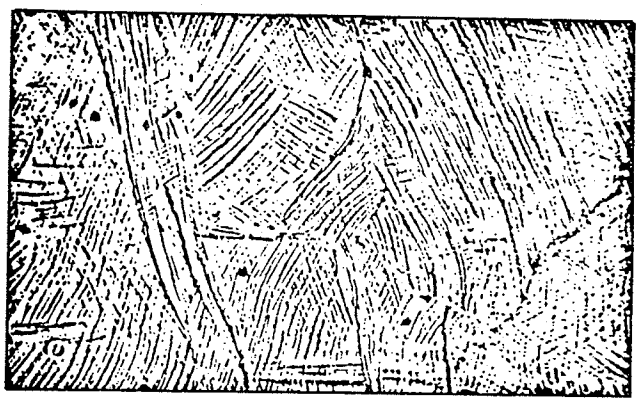

Fig. 91 Microstructure of swaged 70% MP35N alloy, [99].

Mechanical properties of the two alloys were also different. The MP35N alloy was generally stronger as reflected in the higher values of hardness for similar amounts of cold reduction (Fig. 92).

The basic concepts of the FCC → CPH martensitic transformation and of mechanical twinning are very similar. The stacking sequence of close-packed planes of the FCC phase is changed into the hexagonal structure by the sweeping of an a/6 <112> partial dislocation on every second plane. Twinning requires a shear of a/6 <112> on each close-packed plane.[87]

A B C A B A B	A B C A C B A
FCC CPH	FCC Twin

In the pole mechanism, the latter is accomplished by the rotation of an a/6 <112> Shockley partial about a dislocation with a screw component a/3 <111>, while the former requires a screw component of 2a/3 <111>.[96,97,98]

Why the martensitic transformation dominates in MP35N and not in our alloy must stem from the free energy changes involved. The hypothetical schematics are shown in Figures 93 and 94. At room temperature, the lowest free energy state of our alloy is the same as high temperature FCC structure, while for the MP35N alloy, it may be the hexagonal phase. If so, the high activation energy of transformation required for the latter retains an FCC lattice. No matter what the initial case for the MP35N may be, however, the rate of change of free energy with cold work must be greater for the FCC structure than for the CPH. After some deformation, the difference in free energy levels between the two lattices is greater than the activation energy, and the transformation occurs. Since mechanical twins were also observed, the free energy level with twinning as a mode of plastic deformation must be close to that of hexagonal transformation. For the MP35N

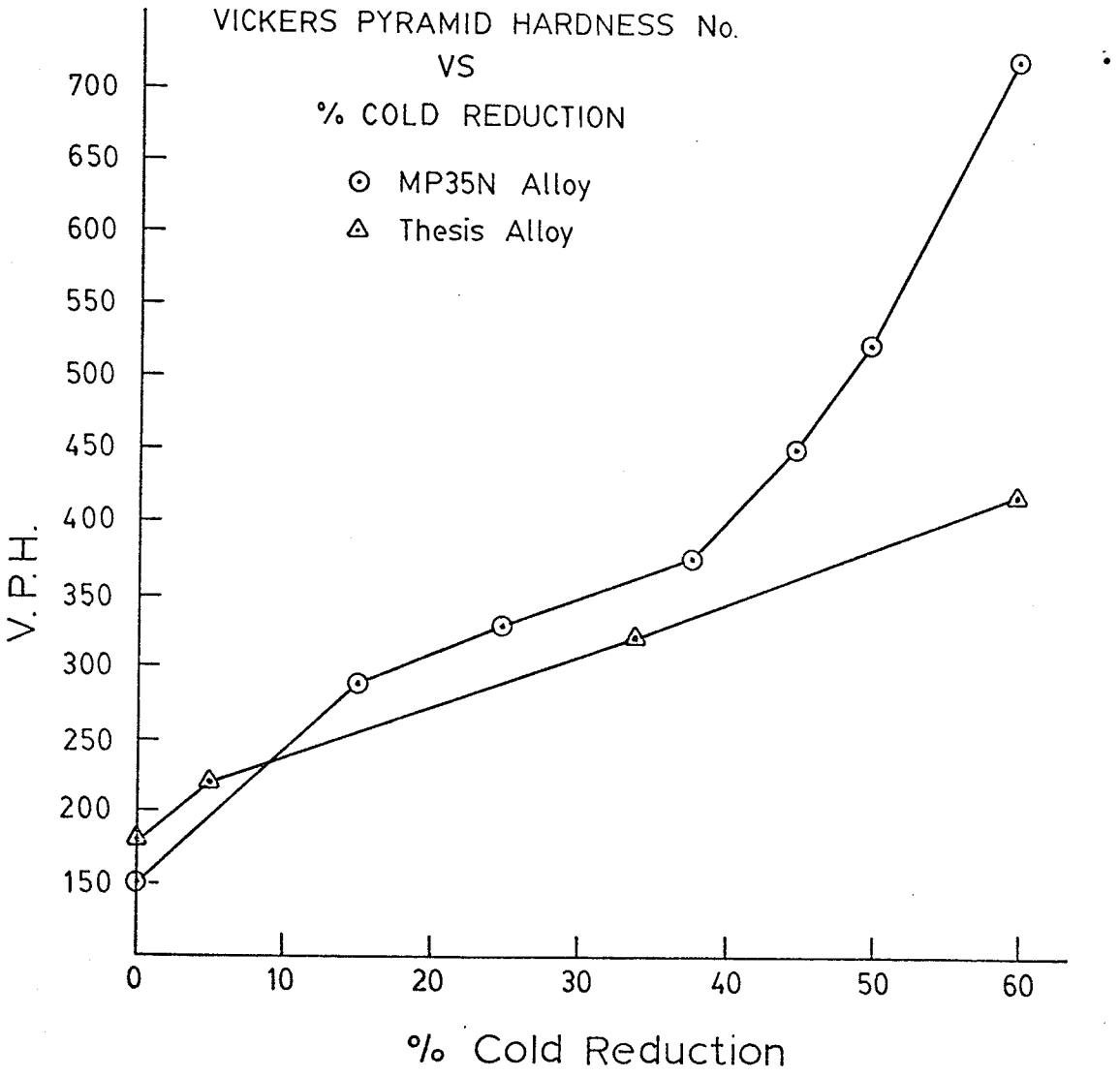
VICKERS PYRAMID HARDNESS No.
VS
% COLD REDUCTION
MP35N Alloy
Thesis Alloy
V.P.H.
700
650
600
550
500
450
400
350
300
250
200
150
0
10
20
30
40
50
60
% Cold Reduction

Fig. 92

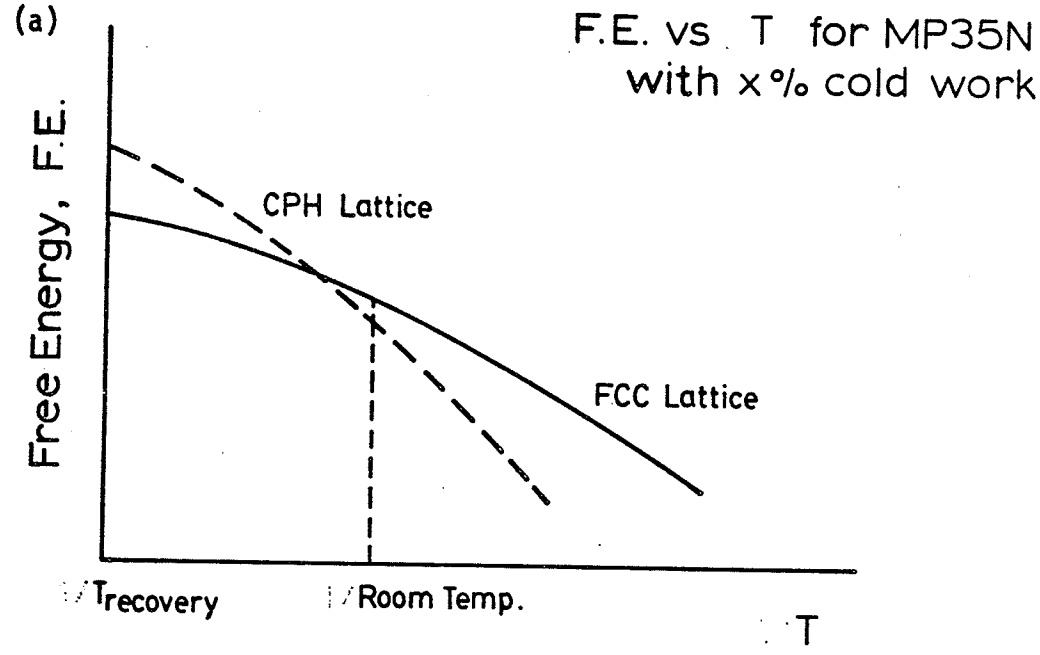
(a)
F.E. vs T for MP35N with x% cold work
Free Energy, F.E.
CPH Lattice
FCC Lattice
Trecovery
Room Temp.
T

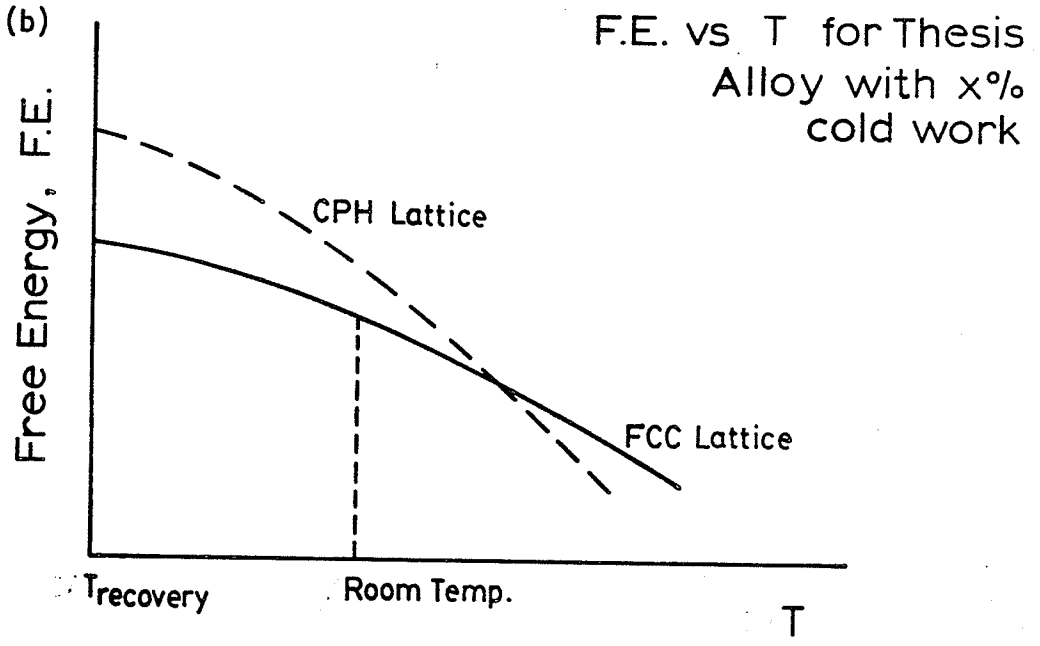
(b)
F.E. vs T for Thesis Alloy with x% cold work
Free Energy, F.E.
CPH Lattice
FCC Lattice
Trecovery
Room Temp.
T

Fig. 93

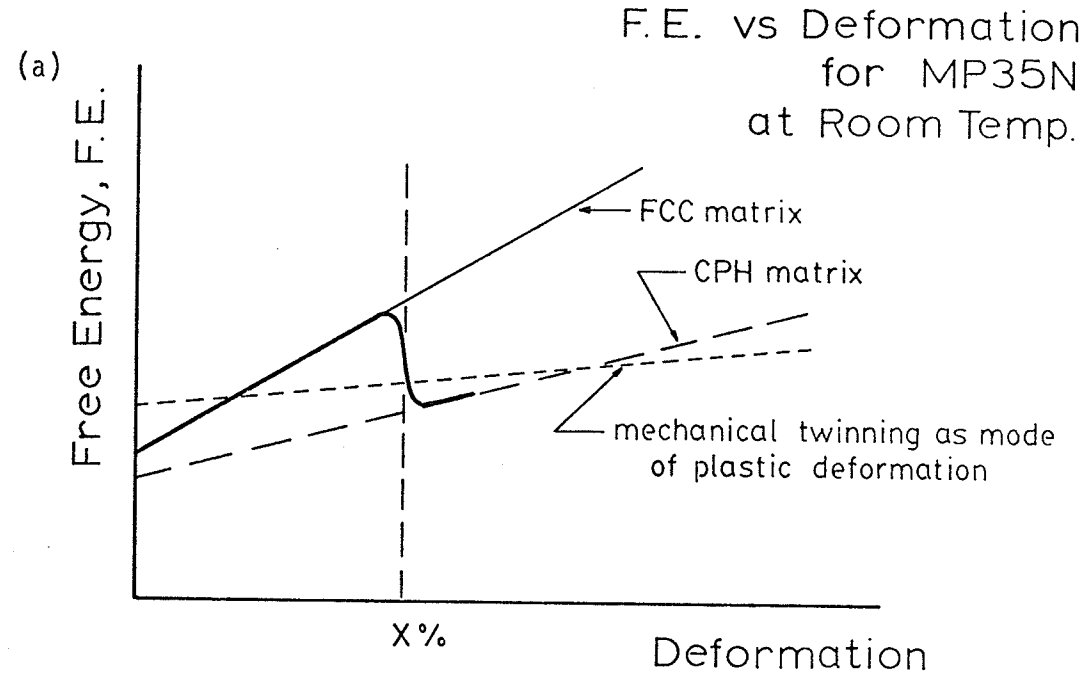
(a)
F.E. vs Deformation
for MP35N
at Room Temp.
Free Energy, F.E.
FCC matrix
CPH matrix
mechanical twinning as mode
of plastic deformation
X%
Deformation

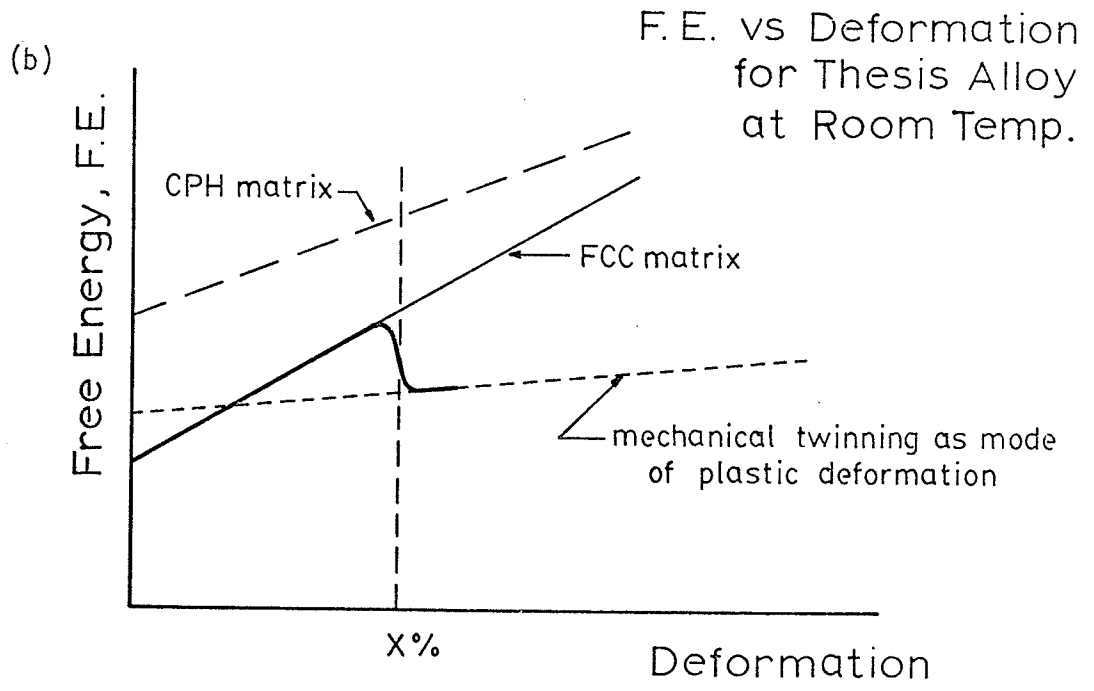
(b)
F.E. vs Deformation
for Thesis Alloy
at Room Temp.
Free Energy, F.E.
CPH matrix
FCC matrix
mechanical twinning as mode
of plastic deformation
X%
Deformation

Fig. 94

alloy then,if the pole mechanism is the operable mode of transformation, dislocation intersections involving the rotation of Shockley partials about screw components of 2a/3 <111> are biased with deformation. But since such a mechanism is inherently inhomogeneous, it is reasonable to expect that those intersections with a/3 <111> screw component may also operate, forming mechanical twins. In our alloy, however, twinning is only possible as the hexagonal phase can not form. Although these are quaternery alloys, the above hypothesis may be justified from a consideration of the binary phase diagrams (Fig. 95 - 99) of the constituent elements. At room temperature, the possible hexagonal phase is due, of course, to the polymetric nature of Co. The addition of nickel suppresses this phase, but it is strongly promoted by the addition of Cr. Mo and Nb both stabilize the high temperature FCC phase, but Nb is much more effective. Thus, although our alloy has a slightly higher ratio of Co to Ni than MP35N, the addition of less Cr, and Nb in lieu of Mo, suggests that the total absence of CPH structure in the former is reasonable. Therefore, our alloy has an overall tendency to remain FCC even with plastic deformation.

Another probable important factor is stacking fault energy. It has been shown that Co and Co-base alloys generally have low SFE.[102] The occurrence of a martensitic transformation and/or mechanical twinning in the above alloys, requiring partial dislocations, is evidence of that fact. The absence of cell formation in the dislocation structure upon deformation (Fig. 58) is also characteristic of low SFE. Work done by Davies et al[103] on Co-Ni alloys shows a continuous drop in SFE from 240 ergs/cm^2 of pure Ni to 10 ergs/cm^2 for an alloy of 70% Co - 30% Ni. The latter has been determined as having a hexagonal structure.[85] Venables,[104] working on the

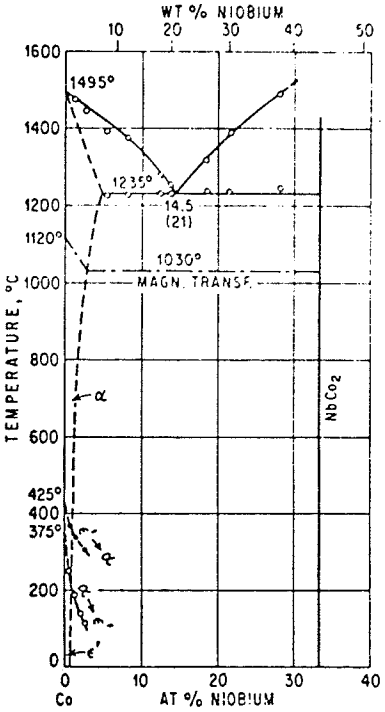

Fig. 95 Binary equilibrium diagram for Co-Nb, [128].

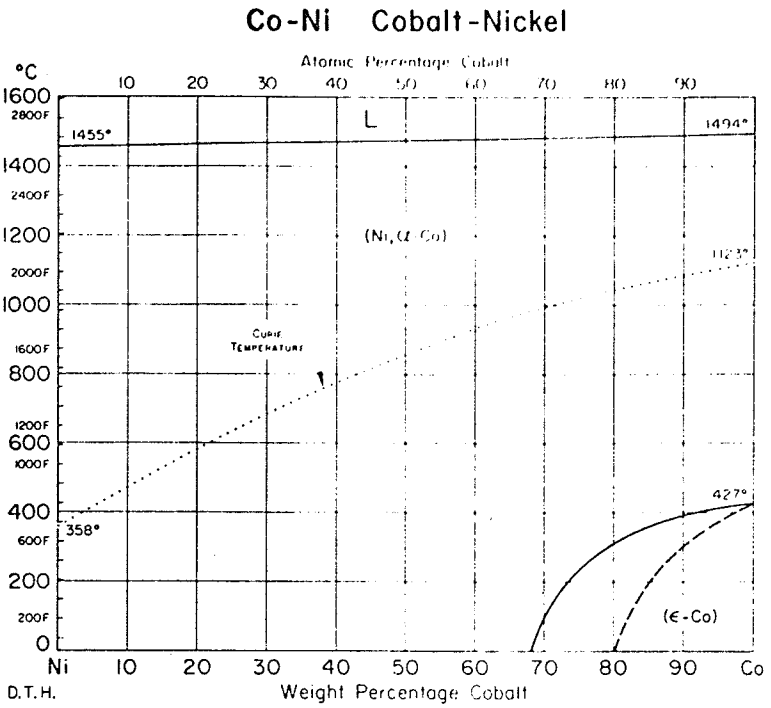

Fig. 96 Binary equilibrium diagram for Co-Ni, [129].

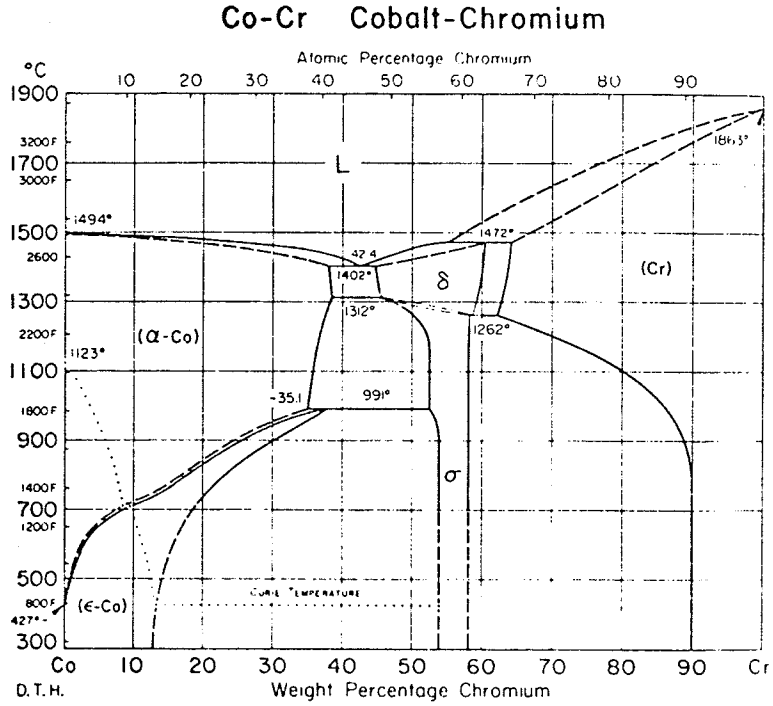

Fig. 97 Binary equilibrium diagram for Co-Cr, [129].

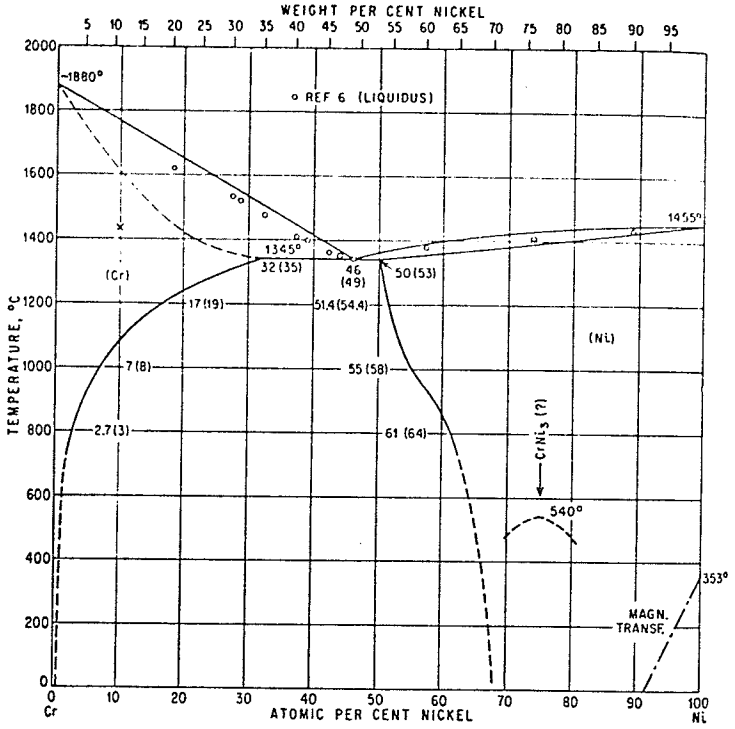

Fig. 98 Binary equilibrium diagram for Cr-Ni, [128] .

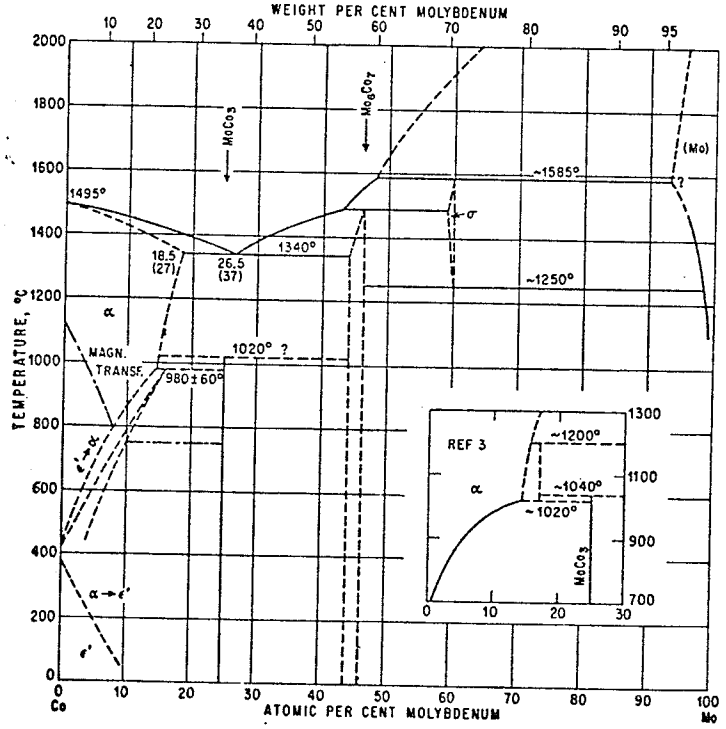

Fig. 99 Binary equilibrium diagram for Co-Mo, [128] .

martensite transformation in stainless steels, has reasoned that the intermediate hexagonal phase ε is favourable when the SFE is low. Similar relationships between SFE and CPH structure, with the addition of solute atoms, has been reviewed by Malis.[105] These observations suggest that the SFE of MP35N alloy is lower than our alloy, and suggest a possible influence on the stress induced hexagonal transformation.

The aging characteristics of our alloy in the solid solution condition have been formally established.[9] The major precipitating phase was orthorhombic Ni_3Nb with small amounts of NbC and $Cr_{23}C_6$ carbides, due to the presence of C as an impurity. Prior deformation does not alter the type of precipitate formed but does affect the nucleation and shape of the orthorhombic precipitate. Electron microscopy indicated that in the very early stages of aging, the deformation twin-matrix interface can act as a nucleation site for Ni_3Nb, supplementing the rate of plate-shaped precipitate formation.

In the literature review, it was shown that the formation of a nucleus involves the summation of three energy terms:

$$\Delta F = -\Delta V + \Delta S + \Delta E$$

where ΔS is the free energy change with the formation of a new matrix-precipitate interface; $-\Delta V$ is the free energy change with the formation of a volume of precipitate (driving force); ΔE is the free energy change associated with strain on formation of precipitate. There is no strain energy associated with a matrix-twin interface that would aid particle nucleation. The volume free energy is a characteristic of the precipitate and would be independent of a nucleation site. It is only the surface

energy requirement for nucleation that is reduced by taking advantage of the surface associated with a twin interface. Figure 100 shows how this would require a smaller critical embryo radius and thus a greater statistical chance of forming. It is interesting to note that as the precipitate forms on a twin interface there is a tendency for the twins to rotate with respect to each other as indicated in the diffraction pattern in Figure 76.

Optical microstructural observations support this contention of precipitation at mechanical twin interfaces. Aging of the solution treated and lightly deformed material results in a cross-hatched pattern of precipitates, as precipitation occurs equally on all four close-packed planes of the matrix. On the other hand, there is an initial preference (10 hr.) for the precipitate to align with deformation twin striations in the moderate and heavily deformed state. As twinning seems to occur on one major {111} plane, it is only in the latter stages of aging that a cross-hatched network of particles is formed. This is stronger in the moderately deformed and aged structure than in the heavily deformed, since the latter is mechanically twinned to a greater extent.

There is no evidence of coherency between matrix and precipitate, but their orientation relationship is in accordance with the matching of their close-packed planes; that is,

$$(010)\ Ni_3Nb\ //\ \{111\}\ FCC$$

$$[100]\ Ni_3Nb\ //\ \langle 110\rangle\ FCC$$

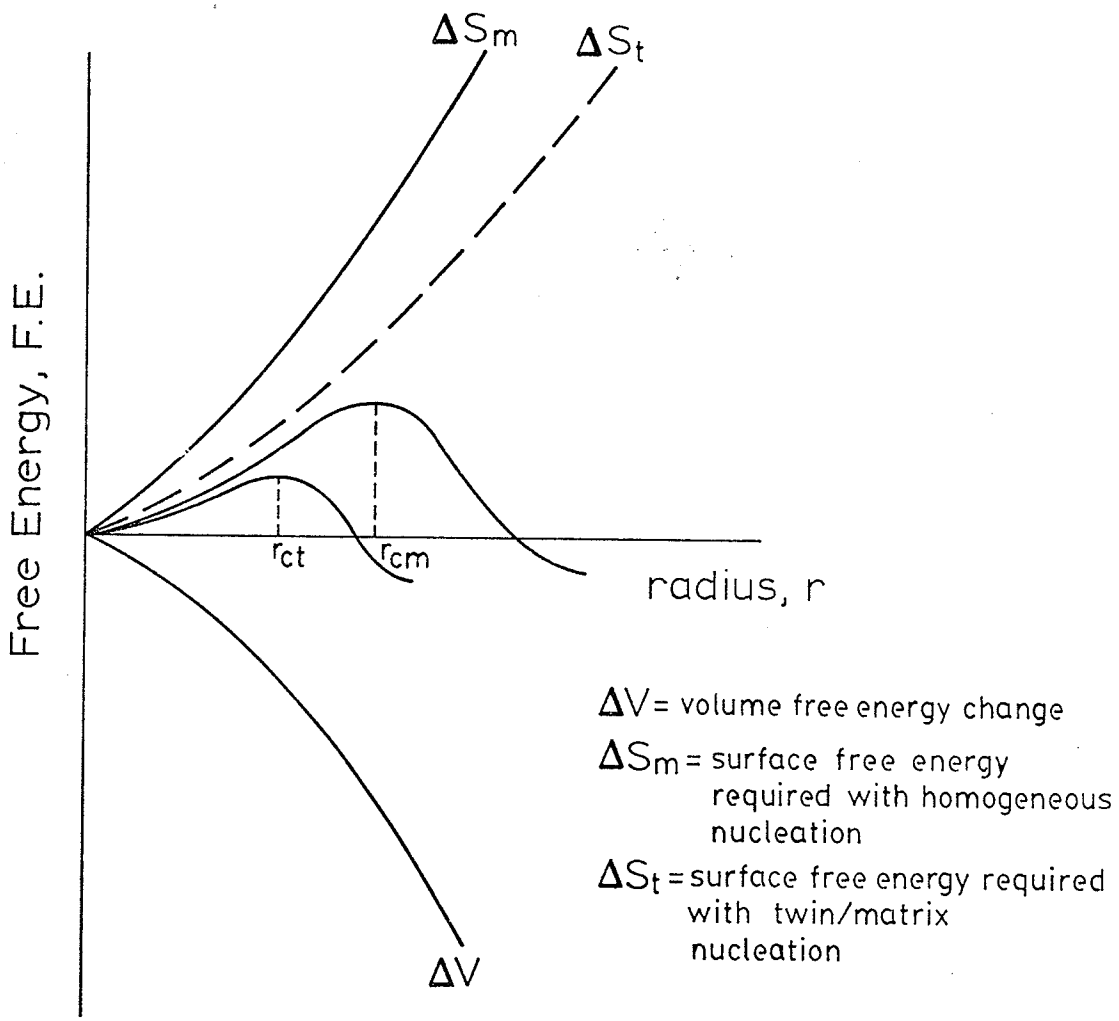
ΔSm
ΔSt
Free Energy, F.E.
rct
rcm
radius, r
ΔV
ΔV = volume free energy change
ΔSm = surface free energy required with homogeneous nucleation
ΔSt = surface free energy required with twin/matrix nucleation

Fig. 100

No precipitation is observed to nucleate at dislocation intersections. It seems that precipitation at deformation twin interfaces is mainly responsible for the rapid rise in peak hardness relative to the solid solution condition on aging. It is also expected that diffusion of solute atoms would have been assisted by the increased vacancy concentration in a deformed condition.

Recrystallization also influences precipitation. This is observed only in the heavily deformed condition and begins in the very early stages of aging. Typical of a relatively low SFE material, there is little evidence of recovery and subgrain wall formation prior to the onset of recrystallization. Observations show the recrystallization front as a moving nucleation site for the orthorhombic precipitate in line with concepts presented in the literature review. Such precipitation is termed discontinuous and results in spheroidal-shaped precipitates. Plate-shaped precipitate at "random" sites ahead of the front is called continuous. The discontinuous precipitate is not preferentially orientated with respect to the recrystallized matrix in the wake of the reaction front. After only 20 minutes at 800° C, their maximum size is 1450 Å, while nucleation of plate precipitate at twin interfaces is just beginning. The required higher rate of diffusion is expected with diffusion along high angle grain boundaries. The recrystallization front is seen as a destroyer of dislocations, and acts as a highway for rapid diffusion, allowing a spheroidal equilibrium precipitate shape to form before being necked off by the boundary (Fig. 77). The factor of 20 in the size range of precipitate is probably typical of precipitation in this manner.

Aging for 100 hr. at 800° C does not complete the recrystallization process and the grain boundary front has the appearance of being held up by the continuous precipitation ahead of the reaction front (Fig. 80).

The area of profuse annealing twins in Figure 81 is unusual, in the sense that one expects and observes such twin orders of magnitude larger in optical microstructures. However, this area may represent a method by which a recrystallization front can move through a network of prior continuous precipitate. The plate-shaped precipitates in this region have a spacing of roughly the same order as the thickness of deformation twins (Fig. 83). It is reasonable to assume that they nucleated at twin lamellae interfaces prior to recrystallization. A recrystallized grain growing into this area would probably be retarded in its movement as in Figure 80. However, recrystallization of the region could occur by grain nucleation at the surface of the plate-shaped Ni_3Nb precipitates. These new grains should have a strong preference to align into the minimum energy configuration of:

(010) Ni_3Nb // {111} MATRIX

[100] Ni_3Nb // <110> MATRIX

With grain growth, the deformation twins would, in effect, recrystallize as annealing twins. The result of plate precipitates within annealing twin boundaries and at ideal orientations would be that shown by Figure 81.

Aging at 800° C corresponds to the temperature range $T_2 > T > T_3$ of Figure 23, where continuous precipitation affects recrystallization. The variation of the discontinuous reaction front driving force with time would be as that depicted in schematic Figure 25d. At $t = t_H$, we have $P = 0$, and the reaction stops.

Aging at 850° C completely recrystallizes the matrix after only ten hours. Precipitates are in the form of both spheroids and plates, but the latter dominates and grows with further aging. These observations fit the temperature range $T_1 > T > T_2$ of Figure 23, where recrystallization is complete before continuous precipitation has begun. The presence of spheroidal precipitates indicates some discontinuous precipitation occurring with recrystallization. The driving force schematic would be similar to Figure 25b. However, the total force P should contain a contribution from discontinuous precipitation.

After ten hours aging, the size of spheroidal precipitate at 850° C was actually smaller than that observed at 800° C (200 - 1000 Å at 850° C vs 100 - 3600 Å at 800° C). At the lower temperature, the reaction front is sluggish, due to retarding force P_r. This would allow a disproportionate amount of time at high rates of solute diffusion along the front, resulting in large discontinuous precipitate. Evidence of this can be seen in Figure 87, where spheroidal precipitates are larger in the vicinity of recrystallization front A than in areas away from the front B. This is consistent with a probably greater retarding force at A than at some earlier history of the front represented by precipitation in B.

Aging at higher temperatures would increase all rates of diffusion involved, but the rates of increase would be greater for diffusion involved in the discontinuous reaction than for continuous precipitation. Thus a retarding force P_r would not occur, allowing less time for discontinuous precipitate to form. Also the driving force for precipitation would, in general, be lower at a higher aging temperature. This would

more than compensate for an increased rate of solute diffusion, resulting in less volume fraction and smaller sized discontinuous precipitate. Also the formation of rows of spheroidal precipitates, as in Figures 88 and 89, suggests that along with destroying the dislocation network, the recrystallization front can also destroy early stages of plate-shaped precipitate at twin interfaces.

The behaviour of the deformation twins on annealing is typical of that described by Cahn.[103] Isolated twin lamellae contract, become parallel sided and blunt ended, and tend to disappear. This was observed in lightly deformed and aged material (Fig. 67). Under heavier deformation, the twin interfaces act as nucleation sites for Ni_3Nb precipitate. Impinging twin lamellae set up stress concentrations and can give rise to recrystallization nuclei as in Figure 79. This photograph also shows the tendency to acquire boundaries parallel to the lamellae, also a common annealing behaviour.

The orthorhombic precipitate (Ni_3Nb) demonstrated an ordered space group symmetry different from that observed for precipitate of the same stoichiometric composition in other alloy systems.[104-111] The X-ray work indicated some extra reflections, matching with the reflecting conditions of the standard space group Pmmn, but which were not present in ASTM file card for this precipitate. These extra reflections could not be accounted for by the other observed precipitates $Cr_{23}C_6$ and NbC. At the same time, the proximity of reflection from the latter at critical angles rendered it impossible to clearly detect another space group symmetry for the orthorhombic precipitate.

With single crystal diffraction by electron microscopy, a clearer definition was possible. Many of the observed reflections in the diffraction patterns were due to (210), (120), and (010) planes, which are forbidden by space group symmetry Pmmn (Appendix B). The only other space group found in the orthorhombic system which allowed these reflections and consistently accounted for all observed diffraction SADP was space group Pma2 (Appendix B). This space group also accounted for all the extra reflections observed in the X-ray powder patterns. Thus the space group of orthorhombic Ni_3Nb precipitate observed in our alloy seems to be different than that observed by Kaufman et al[105] in Inconel 718. They concluded that the structure for Ni_3Nb is isomorphous with Cu_3Ti (orthrhombic space group Pmmn). However, in their interpretation of Ni_3Nb, they did observe the (120) reflection which is forbidden by Pmmn, but permitted by Pma2.

The changes in mechanical properties with aging of the various deformed conditions coincides on the whole with the observed changes in microstructure. The increasing density of mechanical twins and vacancies with greater degree of prior deformation is followed with the general tendency of peak strength occurring at shorter aging times. The as cold worked microstructure of the lightly and moderately deformed specimen is mostly retained with aging up to 100 hours. The relatively flat aging curves of yield and ultimate strengths and the curves of decreasing elongation suggest that precipitation makes a minor contribution to the overall strength of the deformed and aged specimens. This is supported by the observed general decrease in strength and increase in ductility with recrystallization and precipitation occurring in the heavily deformed condition. This is reasonable since the main precipitate, Ni_3Nb

is not coherent with the matrix and its orthorhombic structure has been identified as the stable overaged equilibrium phase in the system of Inconel 718.[127,129] The main strengthening phase of this superalloy was identified as metastable Ni_3Nb body centered tetrogonal, which was never observed in our alloy.

CHAPTER 6 CONCLUSIONS

1. The superalloy studied in this work mechanically twinned on plastic deformation instead of the martensitic transformation (FCC - CPH) which has been observed in alloys of similar composition.

2. On aging, the mechanical twin lamellae act as nucleation sites for Ni_3Nb orthorhombic precipitate while the lamellae themselves have a tendency to disappear. In general, continuous precipitation of Ni_3Nb in the annealed and cold worked matrix is plate-shaped and preferentially oriented as (010) Ni_3Nb // {111} FCC Matrix; [100] Ni_3Nb // <110> FCC Matrix.

3. Partial recrystallization of the matrix occurs with a prior cold rolling of 60% and at an aging temperature of 800° C. This is accompanied by discontinuous precipitation of Ni_3Nb orthorhombic in the shape of spheroids with no preferred orientation with respect to the recrystallized matrix.

4. Aging at 850° C completely recrystallizes the matrix before continuous precipitation begins.

5. Structural analysis of both continuous and discontinuous Ni_3Nb orthorhombic precipitate favour a space group symmetry of Pma2, as opposed to the previous observed symmetry of Pmmn in other alloy systems.

6. On aging, the mechanical properties change in accordance with microstructural transformation. In this superalloy, it appears that precipitation of Ni_3Nb offers little improvement of mechanical properties over an as deformed condition.

APPENDIX A

A matrix fault structure was observed in the annealed and deformed conditions and was ultimately identified as entirely a twinning phenomenon. This conclusion was based on the following electron microscopy evidence:

(a) The indexing of selected area diffraction patterns (SADP) from the fault areas as FCC crystal structure with a lattice parameter identical with the general matrix.

(b) The observed superposition of matrix and fault diffraction patterns in a normal twin-matrix relationship.

(c) The demonstration of crystallographic correspondence between an observed independent FCC diffraction pattern as in (a), with an observed matrix pattern at some relative tilt, on the assumption of a twin structure.

(d) The demonstration that observed anomalous SADP from fault areas are due to the thiness of the fault, and the structure most probably being twins.

Trace analysis is a technique[115] employed using diffraction patterns in conjunction with brightfield or darkfield images to establish on which planes of the matrix lattice a structure or fault is associated with. This tied the observed faults with matrix {111} planes in both annealed and deformed conditions.

The most obvious evidence of a twin structure is that of (b). The process of twinning is effectively a transformation of a crystal volume from one orientation to another along a close-packed plane. This has been mathematically expressed by Hirsch[116] such that, knowing the twin plane, one can predict the transform of any crystallographic direction or plane of the original crystal volume to that of the twin volume. The observation of

superimposed diffraction patterns from one area that includes a suspect twin band and matrix volume is a direct observation of the resultant transformation. Verifying this by theoretical considerations[116] would serve as proof of the twinning phenomena.

Several of the superimposed diffraction patterns were observed in the deformed condition. The most common was the "classical" matrix-twin relationship of (110) FCC Matrix // (110) Twin. However, the one discussed below in some detail is the observed (114) Matrix // (110) Twin. This was found in the cold rolled 5% condition and will be referred to again in the discussion of anomalous diffraction patterns. The brightfield and diffraction patterns are Figures 101 and 102. Trace analysis established a fault plane of (111) with a (114) matrix plane orientation. From Hirsch[116] we have the following relationships which transform a matrix plane (hkl) to the equivalent twin plane (h'k'l') for twinning on plane (111):

$h' = (-h + 2k + 21)/3$; $k' = (2h - k + 21)/3$; $l' = (2h + 2k - 1)/3$.

This will transform (114) matrix to (110) twin, thus theoretically predicting the observation.

Isolated diffraction patterns from the fault areas in the form of evidence (a) were found occasionally in deformed and annealed conditions. In one case, the pattern was tied directly and unambiguously to twinning and formed evidence of type (c). This involved a 60% as cold rolled condition with an isolated FCC {112} type fault diffraction pattern shown in Figure 103. Matrix diffraction patterns of the {210} and {321} type, shown in Figures 104 and 105, were observed at rotations of 23° and 38° respectively from the fault pattern, about a common tilt axis. Trace

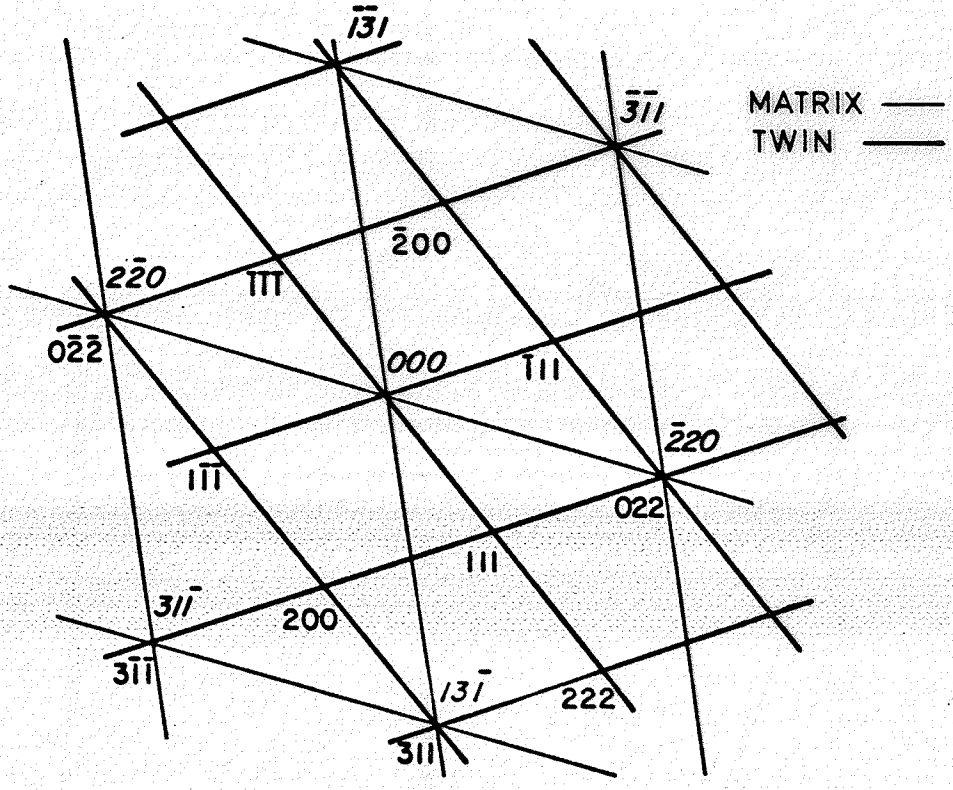
$\bar{1}\bar{3}1$
$\bar{3}\bar{1}1$
MATRIX
TWIN
$\bar{2}00$
$2\bar{2}0$
$1\bar{1}1$
$0\bar{2}\bar{2}$
000
$\bar{1}11$
$\bar{2}20$
$1\bar{1}\bar{1}$
022
111
$31\bar{1}$
200
$3\bar{1}\bar{1}$
$13\bar{1}$
222
311

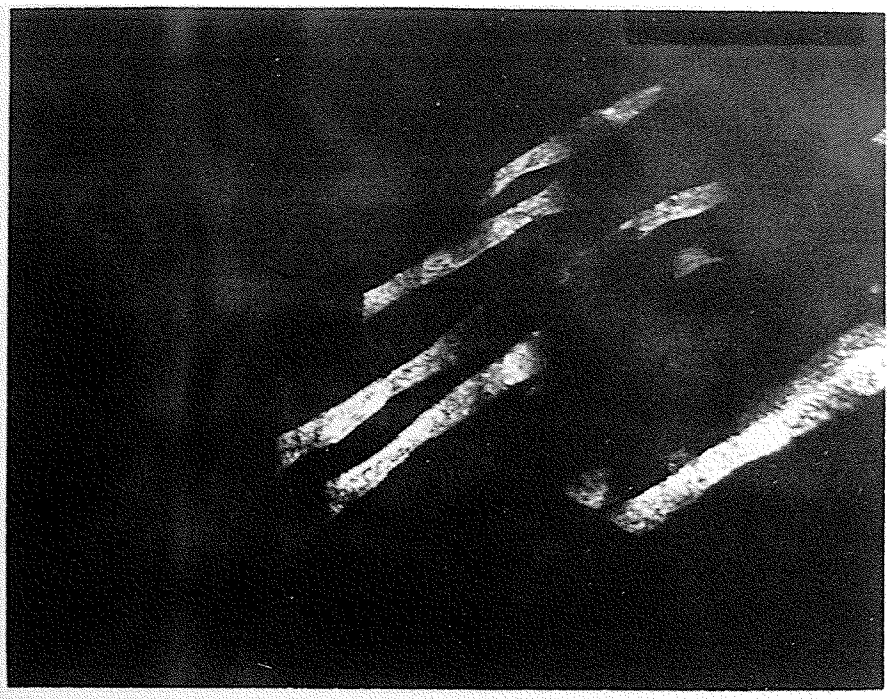

Fig. 101 Darkfield of fault area in as 5% CR. (35,400 X)

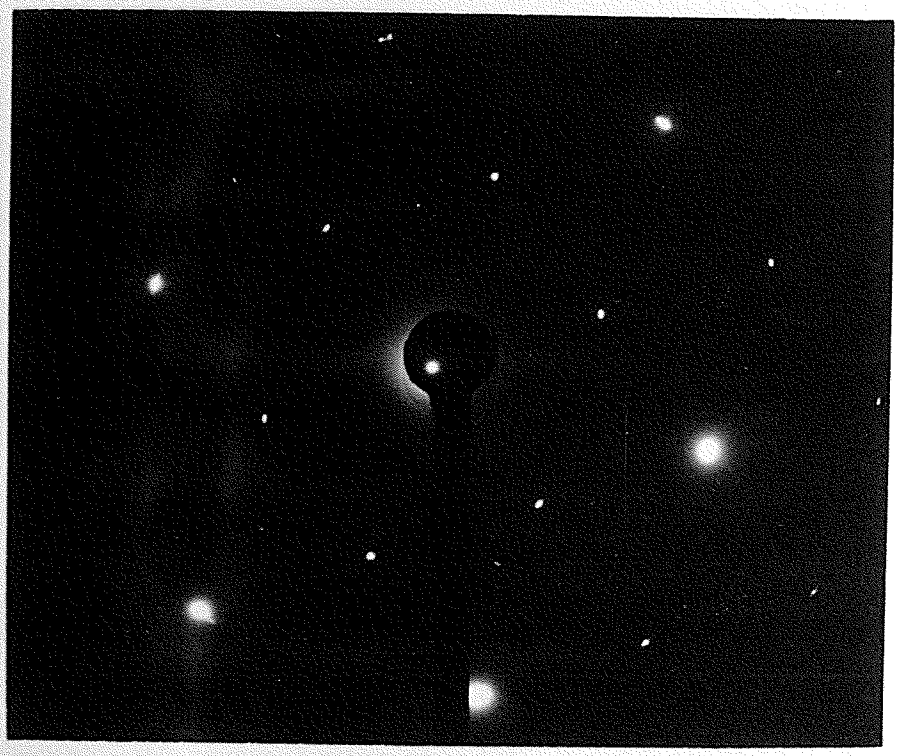

Fig. 102 SADP of fault region and matrix of Fig. 101. (114) matrix // (110) twin.

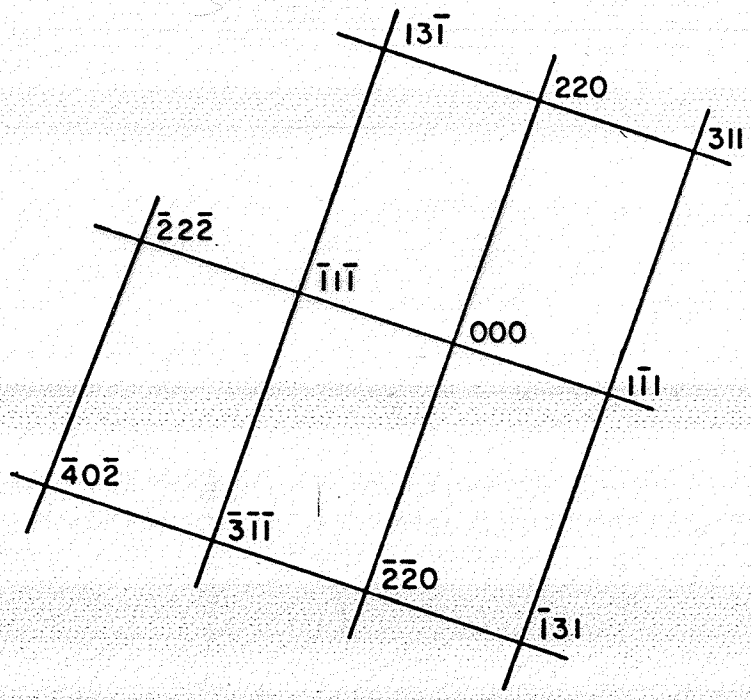
131
220
311
222
111
000
111
402
311
220
131

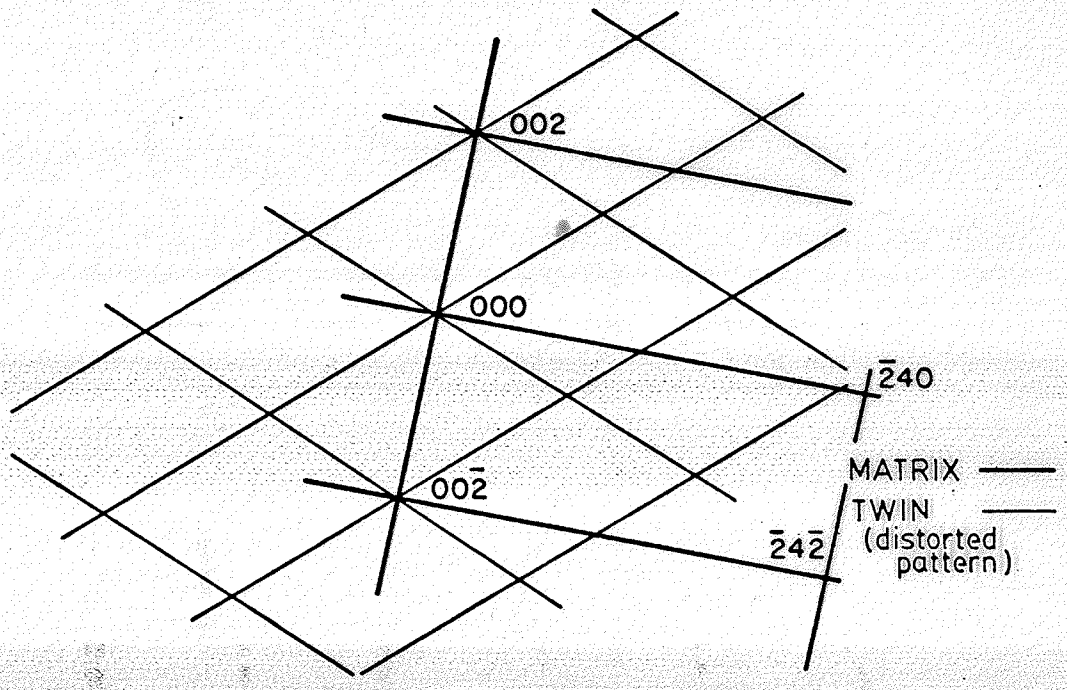
002
000
240
002
242
MATRIX
TWIN
(distorted
pattern)

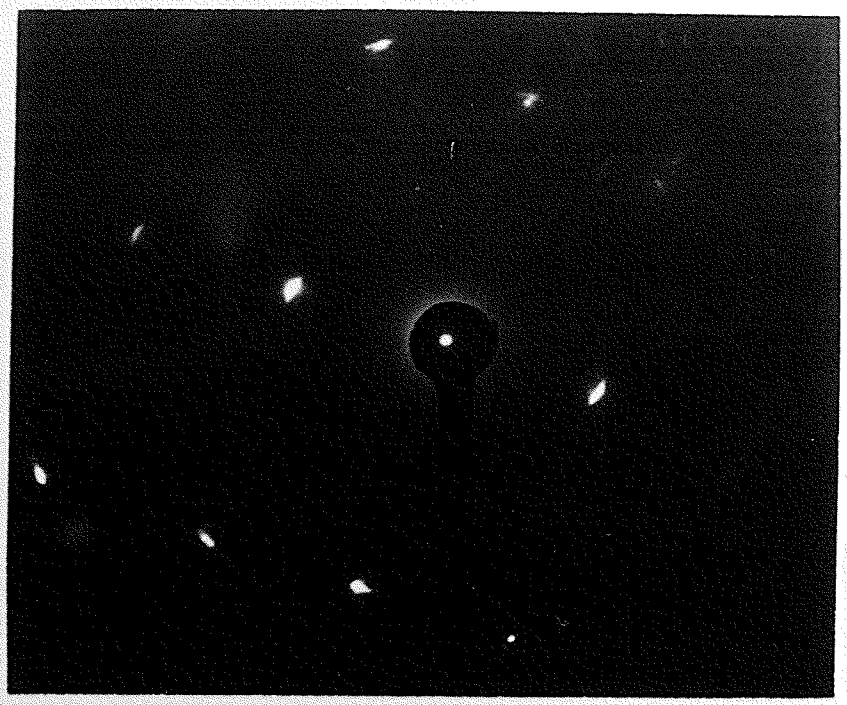

Fig. 103 SADP from fault area of as 60% CR specimen. Pattern matches FCC (112).

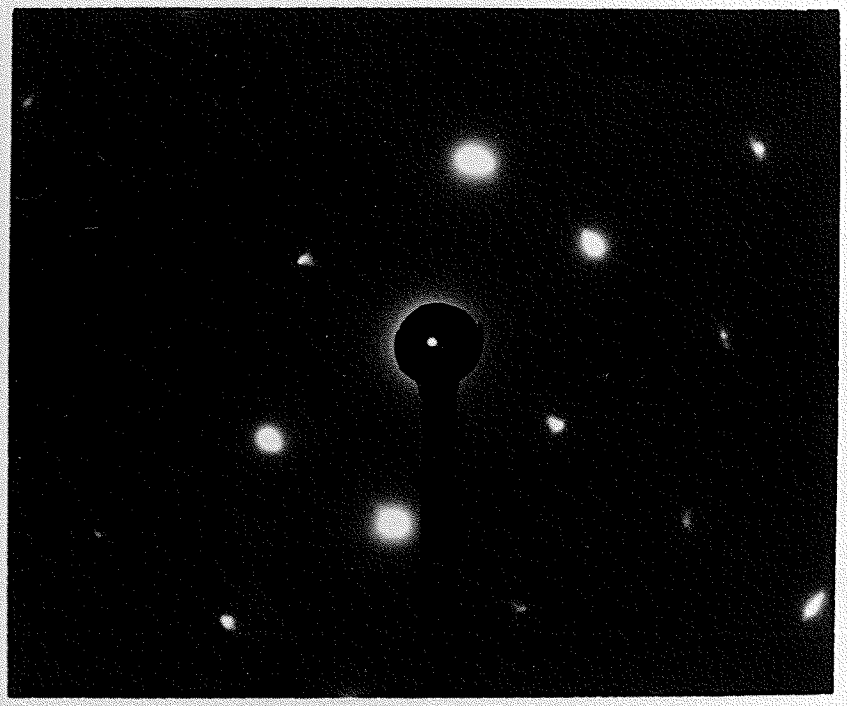

Fig. 104 SADP from same area as Fig. 103 only with 23° tilt. The pattern of the matrix fits (210) FCC.

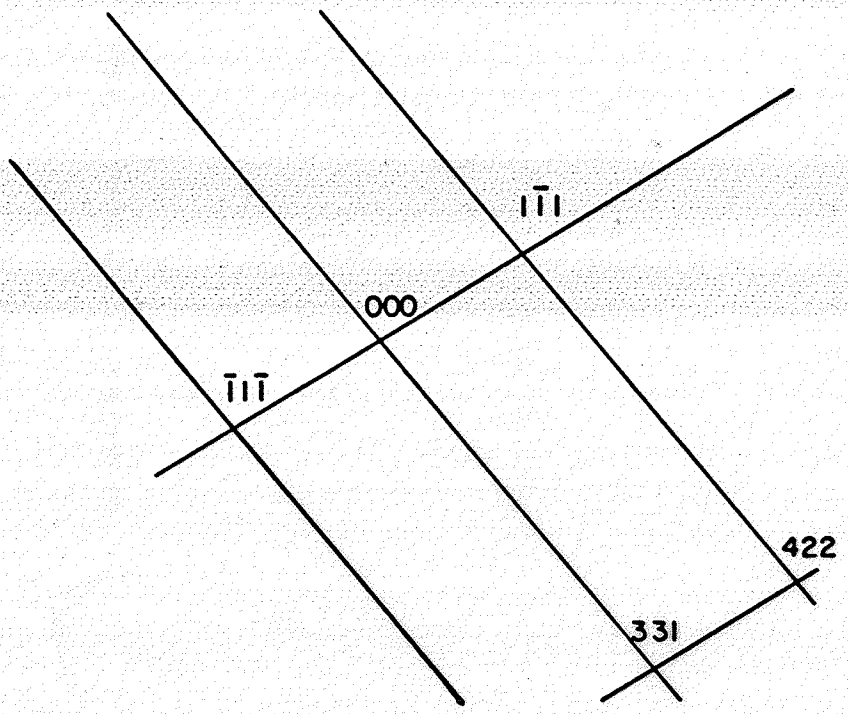
1$\bar{1}$1
000
$\bar{1}$1$\bar{1}$
422
331

Fig. 105 SADP from same area as Fig. 103 only with 38° tilt. The pattern of the matrix fits (321) FCC.

analysis established the fault plane as (111) for the matrix orientations of (210) and (321). Then, with the assumption of ($1\dot{1}1$) twinning, Hirsch's relationships[113] transform the {112} type fault orientation to a matrix orientation. The theoretical angles of this orientation with (210) and (321) should equal the aboserved angles of tilt. However, there are twelve equivalent {112} type planes. The correct one, obtained by trial and error, is ($\bar{1}$,1,2) which transforms to (21,3,$\bar{6}$) matrix. The ideal angles of 24° and 40° with (210) and (321) respectively compare favourably with observed 23° and 38°.

The fault diffraction patterns considered so far were rather of a perfect nature, where symmetry matched a theoretical FCC structure.[117] However, the majority of patterns were not of exact FCC symmetry. About twenty types were observed, half of them only once. Every attempt was made to attach these patterns to some consistent crystal structure, especially the suspected CPH martensite. Nothing was found satisfactory and it remained a puzzlement for some time. Finally it was resolved that these irregular diffraction patterns were FCC, but distorted due to the thiness of the twin bands. Theoretical analysis[116] shows that diffraction patterns can be considered as planes through reciprocal lattice space of a crystal structure. The points in this reciprocal space are actually some distribution of electron diffraction intensity. For crystals in the shape of thin discs or plates, this distribution has the character of spikes which are normal to the plates or discs in real space. When an observed diffraction pattern is the result of intersection with inclined diffraction spikes (that is, plane of disc or plate crystals inclined to electron beam), the effect of tilting is visualized in Figure 106. A perfectly symmetrical pattern can be distorted

(a)

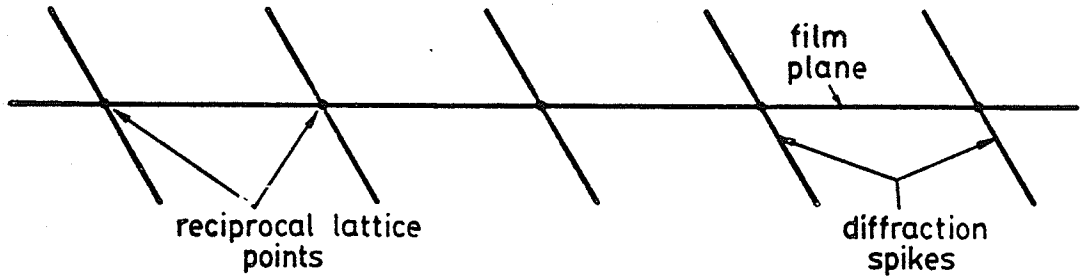

(b)

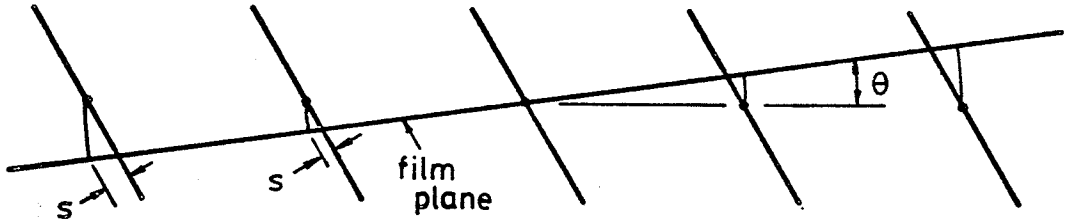

Fig. 106a Electron diffraction by a thin plate or disc of some crystal structure results in an electron distribution of intensity about reciprocal lattice points in the form of spikes. Recorded diffraction patterns on the film plane result from the intersection of Erwald's sphere, which can be considered a plane in electron diffraction, and the diffraction intensity. In this case, the pattern has the perfect ideal symmetry for some plane (hkl), since the film plane intercepts the intensity distribution at the ideal reciprocal lattice points.

Fig. 106b Tilting by an angle θ from (a) gives a diffraction pattern resulting from the intersection of Erwald's sphere and reciprocal spikes of diffraction intensity. Pattern has a distorted symmetry for plane (hkl). The shift in diffraction spots on the film for a rotation of θ is indicated by S.

by such a tilt. In the following, expressions are derived which give this distortion as a translation or shift in the diffraction spots on tilting. By comparing recorded diffraction patterns at relative tilts with theoretical calculated shifts, one can show that anomalous diffraction patterns are due to the thiness of the twin bands.

Consider Figure 107, which demonstrates the relationship between the matrix plane containing the twin (twin plane), the plane of the photographic film (film plane) and its intersection with a diffraction spike (line PS). The problem is to determine the change in the position of intersection point Q with a rotation about the tilt axis. The rotation is best visualized as a rotation of the twin plane, such that its normal remains at a fixed angle α with the tilt axis.

A co-ordinate system is chosen with the x-axis parallel to the tilt axis and with the film plane as the x-z plane. The twin plane can be described by the equation:

$$ux + vy + wz = 0 \qquad (1)$$

where u, v, and w are the direction cosines of the twin normal n_T, and (x,y,z) are the position co-ordinates of any point on the twin plane. Referring to Figure 107, the direction cosines are defined by: $u = \cos \alpha$ (fixed), $v = \cos \beta$, and $w = \cos \gamma$. Consider point P as a point on the twin plane whose co-ordinates are (a,b,c). This now defines the twin plane according to the equation:

$$ua + vb + wc = 0 \qquad (2)$$

The film plane is described by the equation:

$$y = 0 \qquad (3)$$

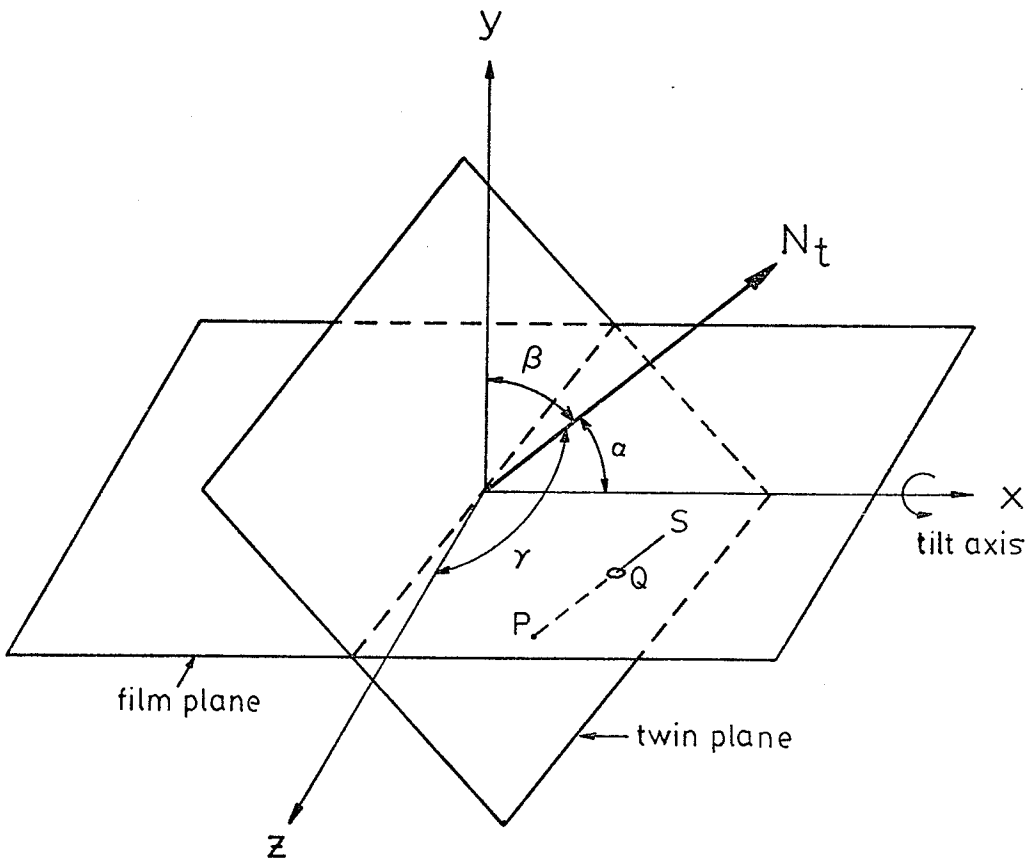

Fig. 107 Relationship between twin plane, film plane, and diffraction spike PS and its intersection with film plane at Q. Twin normal, N_t, has direction cosines of cos α, cos β, cos γ.

The equation of a line through P normal to the twin plane is given by:

$$\frac{x - a}{u} = \frac{y - b}{v} = \frac{z - c}{w}$$

where (x,y,z) is any point on that line. Consider point Q (Qx,Qy,Qz) to be such a point, and which is also a point on the film plane (that is, Qy = 0). Line PQ is now defined by the equation:

$$\frac{Qx - a}{u} = \frac{-b}{v} = \frac{Qz - c}{w} \qquad (4)$$

which yields:

$$Qx = \frac{-ub}{v} + a$$

$$Qz = \frac{-wb}{v} + c$$

$$Qy = 0 \qquad (5)$$

We now have a solution for the position of point Q in terms of the position of point P on the twin plane. Similarly, the position of point P in terms of Q can be determined by noting that P (a,b,c) is simultaneous solution for equations (2) and (4). This yields the following expressions:

$$b = \frac{-uQx - wQz}{\frac{u^2}{v} + \frac{w^2}{v} + v}$$

$$a = \frac{bu}{v} + Qx$$

$$c = \frac{bw}{v} + Qz \qquad (6)$$

Now consider a rotation of the film plane and co-ordinate axes about the tilt axis (x-axis) by an amount Θ as shown in Figure 108. The position of any fixed point (x,y,z) will have new co-ordinates (x',y',z') with respect to the new set of axes X', Y', Z'. For counter-clockwise rotation about

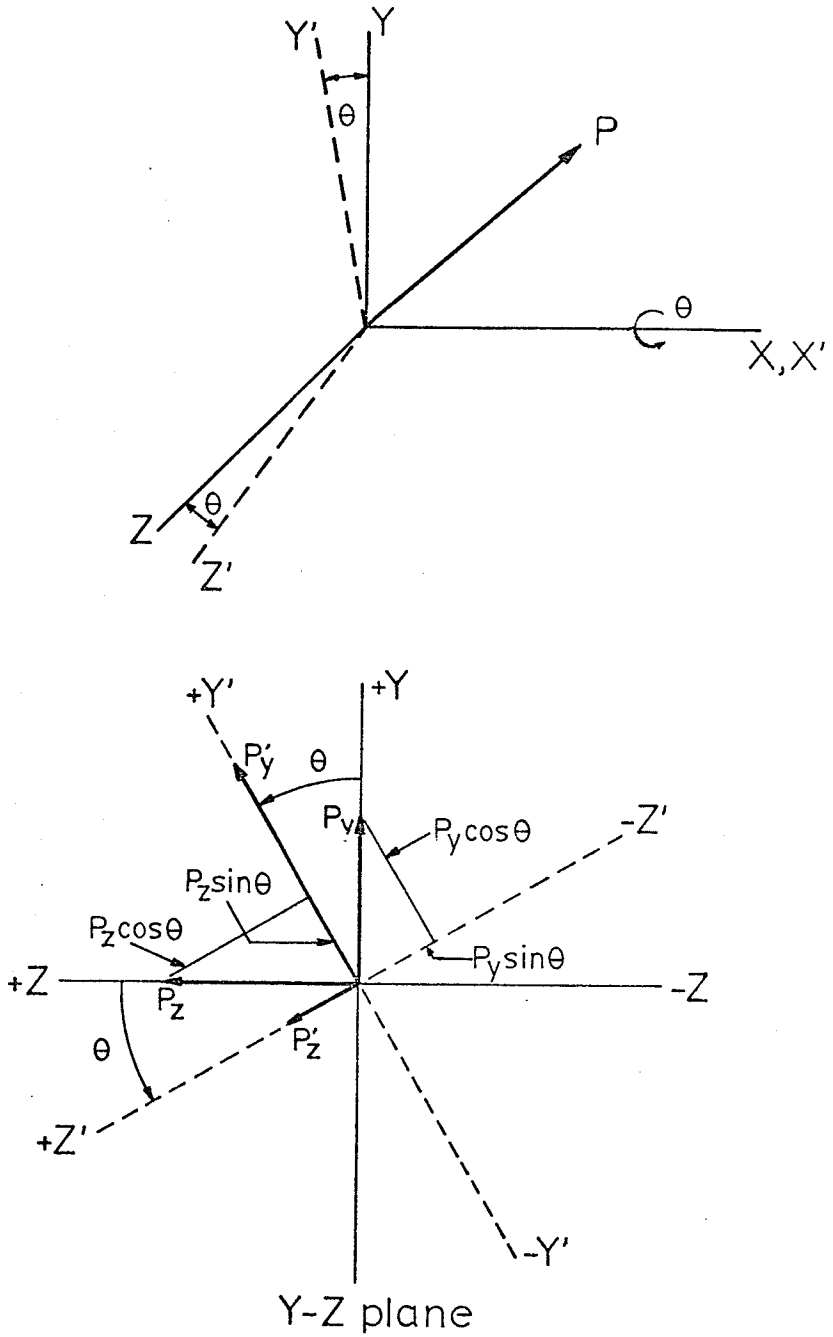

Fig. 108 A rotation of θ about the tilt axis of the film plane and co-ordinate axes is shown. The new co-ordinates of point P in terms of the old set of axes are: $P'_x = P_x$

$$P'_y = P_y \cos\theta + P_z \sin\theta$$

$$P'_z = P_z \cos\theta - P_y \sin\theta$$

the tilt axis, the new co-ordinates of point P can be expressed as:

$$x' = x$$

$$y' = y \cos \Theta + z \sin \Theta$$

$$z' = z \cos \Theta - y \sin \Theta$$

This can be expressed in the form of a transformation matrix, such that:

$$\begin{matrix} x & 1 & 0 & 0 & x' \\ y & 0 & \cos & \sin & = & y' \\ z & 0 & -\sin & \cos & z' \end{matrix}$$

Applying this transform to point P with initial co-ordinates (a,b,c,) we obtain:

$$a' = a$$

$$b' = b \cos \Theta + c \sin \Theta$$

$$c' = -b \sin \Theta + c \cos \Theta \qquad (7)$$

Similarly, the new direction cosine of the twin plane can be expressed as:

$$u' = u$$

$$v' = v \cos \Theta + w \sin \Theta$$

$$w' = -v \sin \Theta + w \cos \Theta \qquad (8)$$

Note that Q is not a fixed point but moves with the film plane and co-ordinate axes to a new position of Q'. Thus its new position (Qx', Qy', Qz') with respect of the axes X', Y', Z' cannot therefore be determined by simple matrix transform. Instead, as a point on the film plane, its co-ordinate $Qy' = 0$, and as a point on the normal to the twin plane through P', it satisfies the following equation for $P'Q'$:

$$\frac{Qx' - a'}{u'} = \frac{-b'}{v'} = \frac{Qz' - c'}{w'}$$

From (7), (8), and (9), we obtain the following expressions for the co-ordinate of point Q':

$$Q'_x = \frac{-u\,(b\cos\Theta + c\sin\Theta)}{(v\cos\Theta + w\sin\Theta)} + a$$

$$Q'_z = \frac{-(-v\sin\Theta + w\cos\Theta)\,(b\cos\Theta + c\sin\Theta)}{(v\sin\Theta + w\sin\Theta)} - b\sin\Theta + c\cos\Theta$$

Where:

$$b = \frac{-u\,Qx - w\,Qz}{\frac{u^2}{v} + \frac{w^2}{v} + v}$$

$$a = \frac{bu}{v} + Qx$$

$$c = \frac{bw}{v} + Qz \qquad (10)$$

Thus for a counter-clockwise rotation of the film plane (that is, co-ordinate axes) or a clockwise rotation of the twin plane, the new position of a diffraction spike and film plane (Q'_x, Q'_z) can be determined from the initial position of this intersection (Qx, Qz) via expression (10). For an opposite rotation, the expression is unchanged. However, a negative value of Θ is used.

The following are examples of how the above expressions were used to identify curious electron diffraction patterns as thin twins. Figures 109 and 110 are patterns from the as cold rolled 5% condition. They are at 23° relative tilt and of the same fault structure area seen in Figure 101. An FCC twin-matrix relationship of (114) matrix // (110) twin has already been shown for Figure 109. (Figure 109 is the same as Figure 102 only at a different projector lens current.) Figure 110 is not a typical symmetrical FCC crystal diffraction pattern and confuses the issue of the crystallographic nature of the fault. This pattern was more commonly observed than any "perfect" symmetrical FCC pattern for similar fault areas in the annealed state and deformed conditions of various degrees.

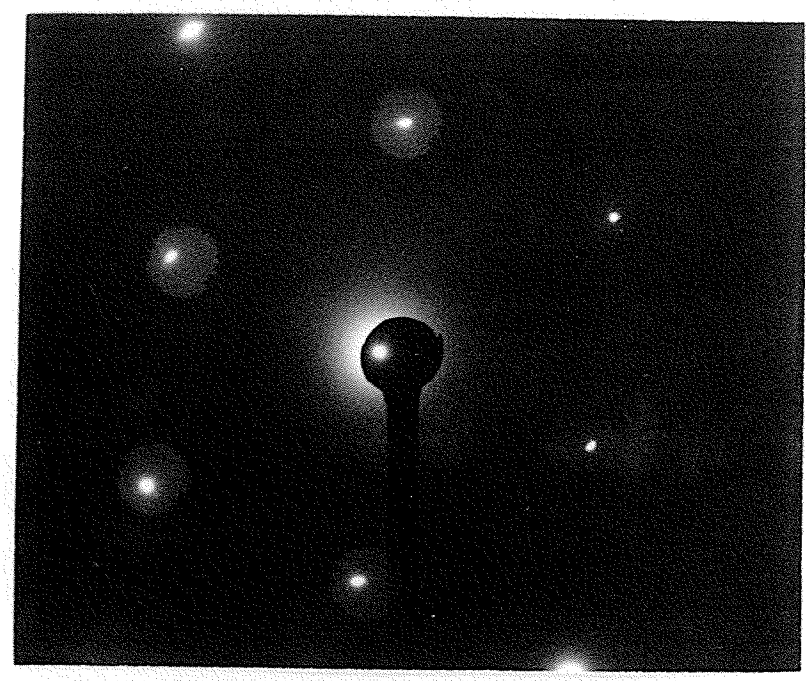

Fig. 109 SADP of fault area seen in Fig. 101. Same pattern as Fig. 102 only at altered projector lens current.

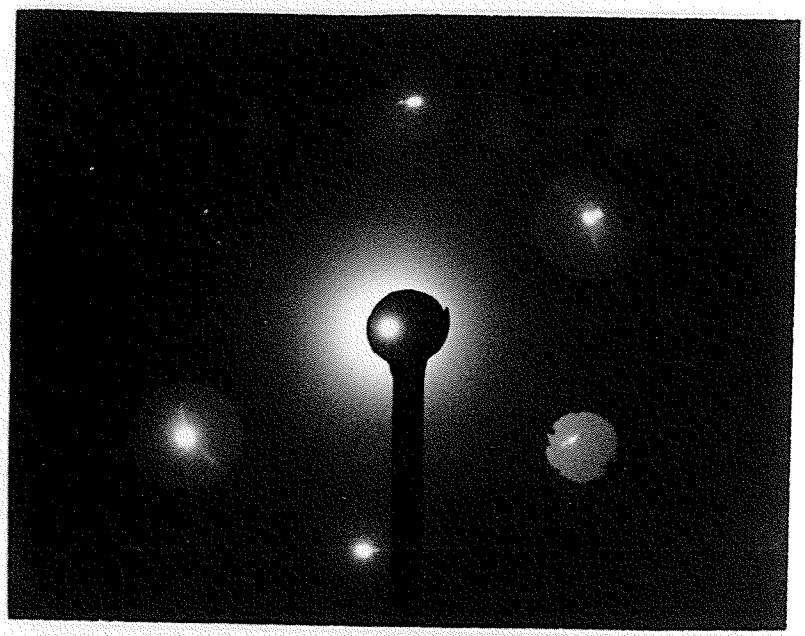

Fig. 110 SADP of same area as Fig. 109, only at relative tilt of 23^{o}.

On the assumption of thin twin bands, theoretical calculations can be made for the shift in position of diffraction pattern spots. By comparing with observed results, it can be determined if Figure 110 is actually a distortion of Figure 109 (that is, distorted (110) FCC pattern). Analysis of the latter establishes a matrix FCC (114) diffraction pattern as the initial film plane. The twin plane is (111) by trace analysis and similarly, the tilt axis is in a $[5,\bar{9},1]$ direction. The relationship of this data to an (x,y,z) co-ordinate system is shown in Figure 111. The z-axis direction is determined from the cross-product of the x and y axes. Now the direction cosines ($\cos\alpha$,$\cos\beta$,$\cos\gamma$) of the twin plane can be determined.

Figure 112 is an overlay showing the position of diffraction spots from the fault area before and after tilting through a clockwise rotation. Consider the two initial points P_1 and P_2. Table I draws a comparison between calculated and observed positions (P_1' and P_2') after rotation. As can be seen, there is a close agreement, a strong argument for the many anomalous diffraction patterns as characteristic of thin twin bands.

Another example is taken from the 60% as cold rolled condition, showing a fault structure in Figure 113. The initial film plane (Fig. 114) corresponds to an FCC matrix (210) electron diffraction pattern and a fault structure pattern without FCC symmetry. With a counter-clockwise tilt of 18° to Figure 115, the band diffraction symmetry is that of the former Figure 110 (that is, distorted FCC (110)). Therefore, the identification of a twin structure rests on showing that the transformation of Figure 114 to Figure 115 is due to the thiness of the twin band.

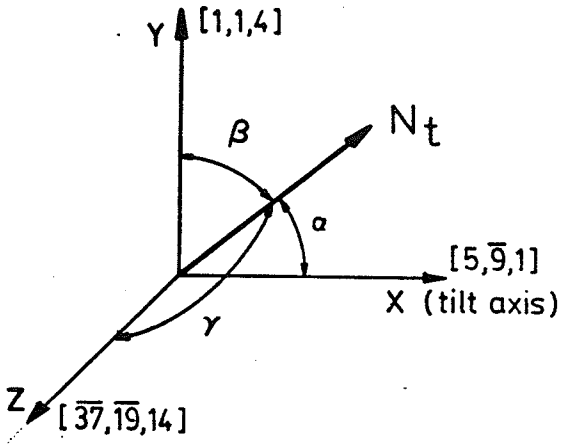

Fig. 111 Relationship of twin plane normal and initial co-ordinate system of Fig. 109.

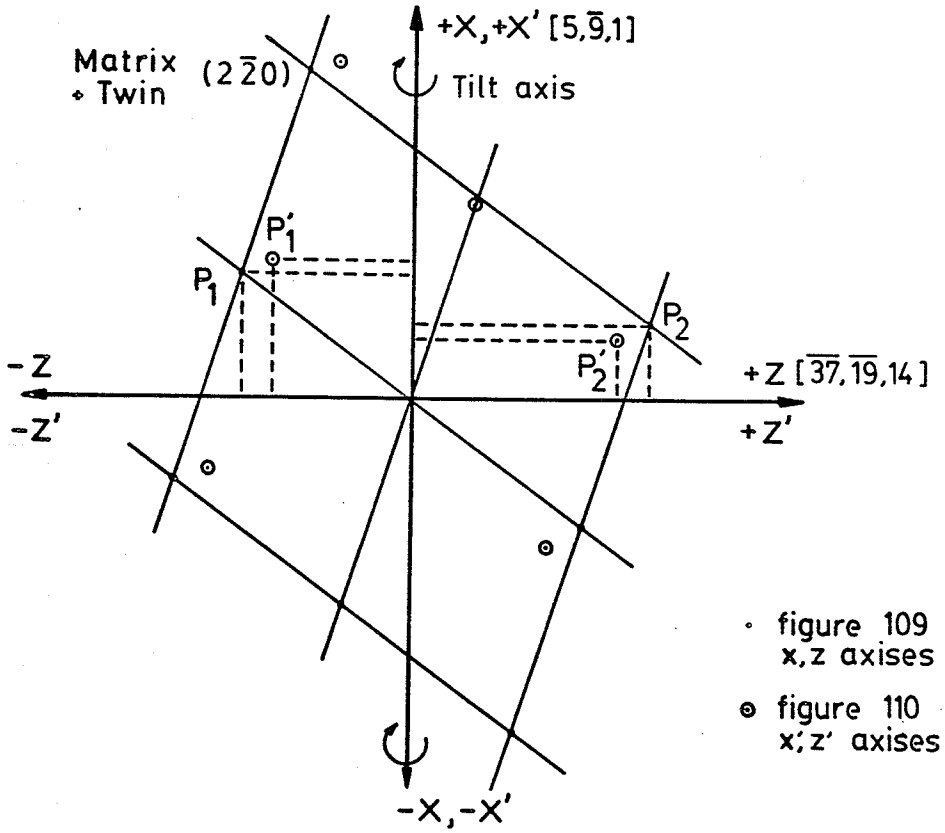

Fig. 112 Superposition of Fig. 109 and 110.

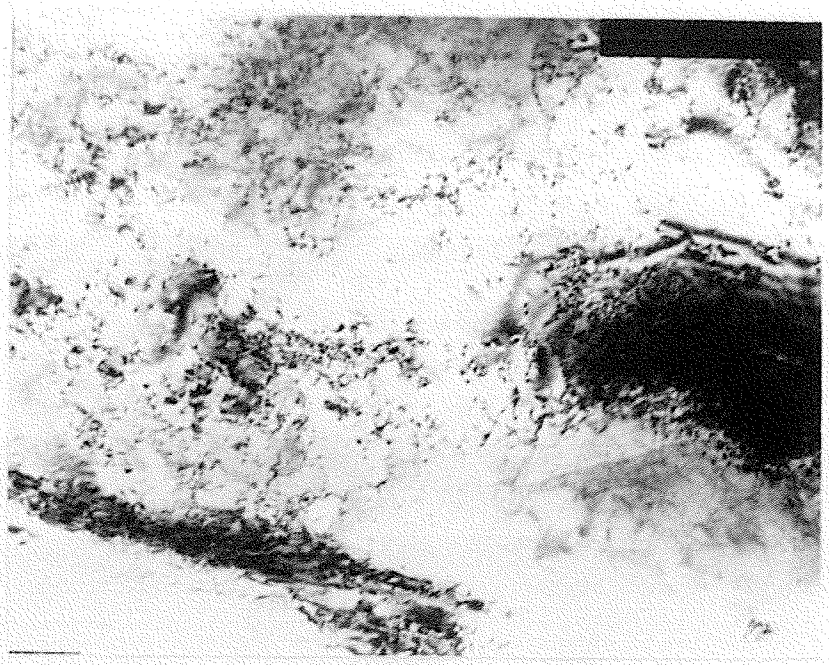

Fig. 113 Brightfield of as 60% CR. Fault structure in lower left-hand corner. (69,500x)

Fig. 114 SADP of fault structure in Fig. 113.

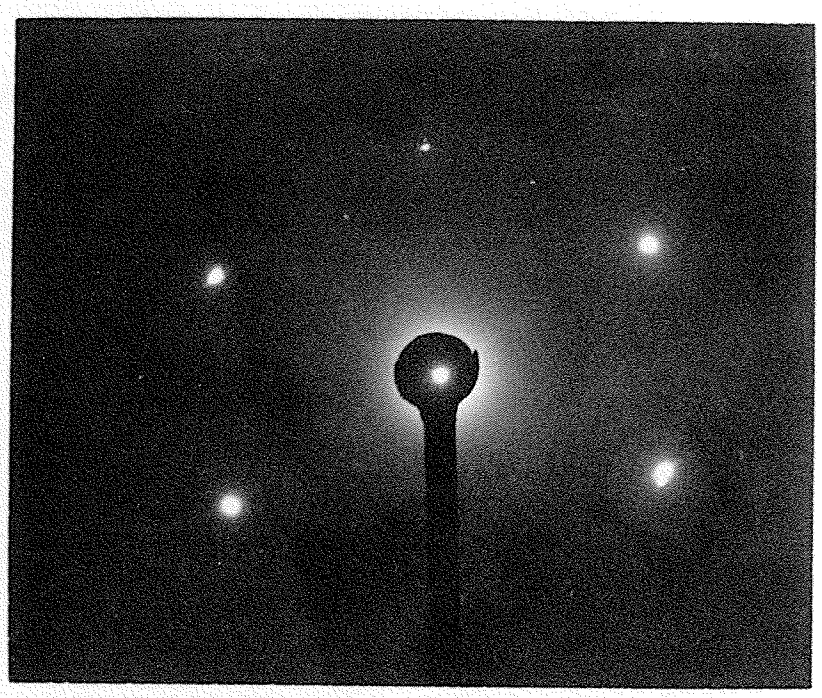

Fig. 115 SADP of same fault structure in Fig. 114 after a tilt of 18°. Symmetry is the same as that of Fig. 110.

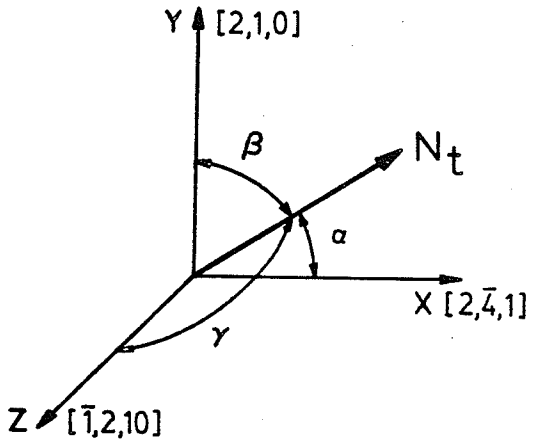

Fig. 116 relationship of twin plane normal with initial co-ordinate system of Fig. 114.

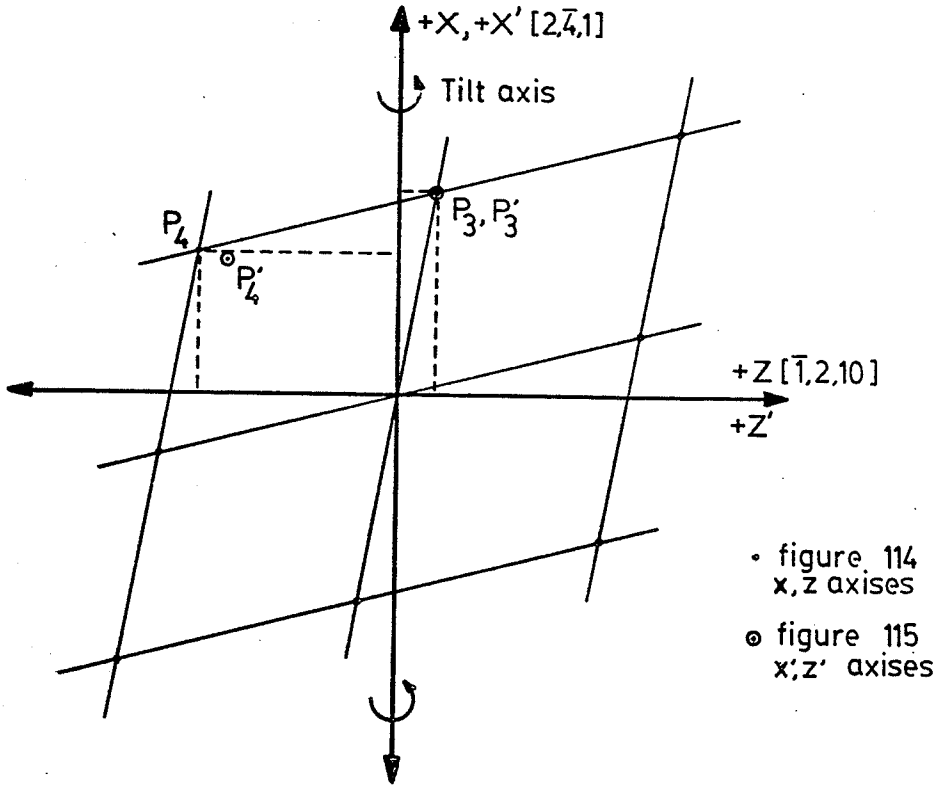

Fig. 117 Superposition of Fig. 114 and 115.

Trace analysis establishes the twinning plane as (111) and the tilt axis as $[2,\bar{4},1]$. From Figure 116, the direction cosines of the twin plane can be determined. Figure 117 is an overlay showing the observed spot shifts with a tilt of 18°. For spots P_3 and P_4, a comparison is drawn between observed and calculated positions in Table I. Again agreement is good.

From these two examples, the general inference is that distorted FCC diffraction symmetry accounts for the majority of observed diffraction patterns and results from thin twin band structure.

TABLE I

INITIAL FILM PLANE Co-ordinates (x-z) axes	ROTATION	FINAL FILM PLANE	
		Observed Co-ordinates (x' - z') axes	Calculated Co-ordinates (x' - z') axes
Figure 109		Figure 110	Figure 110
P_1x = 16.5 P_1z = -22.0	-23°	P_1x' = 18.0 P_1z' = -18.0	P_1x' = 17.7 P_1z' = -18.0
P_2x = 10.0 P_2z = 31.0		P_2x' = 8.0 P_2z' = 27.0	P_2x' = 7.9 P_2z' = 26.1
Figure 114		Figure 115	Figure 115
P_3x = 27.0 P_3z = 4.5	+18°	P_3x' = 27.0 P_3z' = 4.5	P_3x' = 27.2 P_3z' = 3.8
P_4x = 19.0 P_4z = -28.0		P_4x' = 18.0 P_4z' = -23.0	P_4x' = 17.8 P_4z' = -23.3

APPENDIX B

Possible reflections for orthrhombic space groups Pmmn and Pma2:

Pmmn

hkl	No Conditions
0kl	
h0l	
00l	
hk0	h + k = 2n
h00	h = 2n
0k0	k = 2n

Pma2

hkl	No Conditions
0kl	
0k0	
00l	
hk0	
h0l	h = 2n
h00	h = 2n

Figures 118 to 121 are SADP of Ni_3Nb precipitate. Figures 118 to 120 show the observed reflections (210), (010), (120) which are forbidden by space group Pmmn but are allowed by space group Pma2. Figure 121 can be indexed as either Pmmn or Pma2. (100) is forbidden by both and is not present in this pattern.

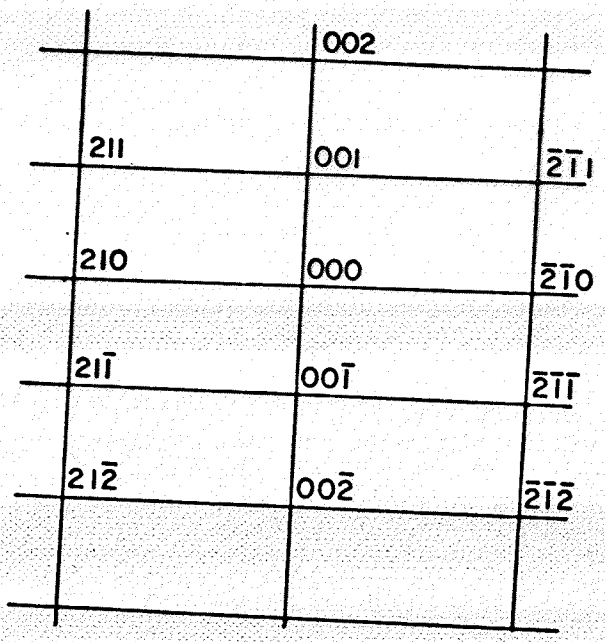
002
211
001
$\bar{2}\bar{1}1$
210
000
$\bar{2}\bar{1}0$
$21\bar{1}$
$00\bar{1}$
$\bar{2}\bar{1}\bar{1}$
$21\bar{2}$
$00\bar{2}$
$\bar{2}\bar{1}\bar{2}$

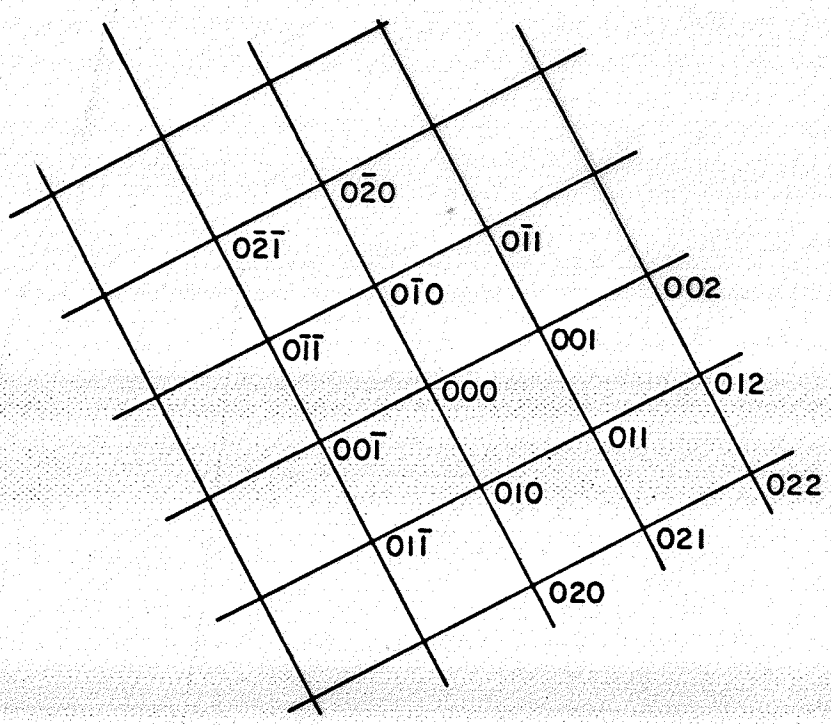
$0\bar{2}0$
$0\bar{2}\bar{1}$
$0\bar{1}1$
$0\bar{1}0$
002
$0\bar{1}\bar{1}$
001
000
012
$00\bar{1}$
011
010
022
$01\bar{1}$
021
020

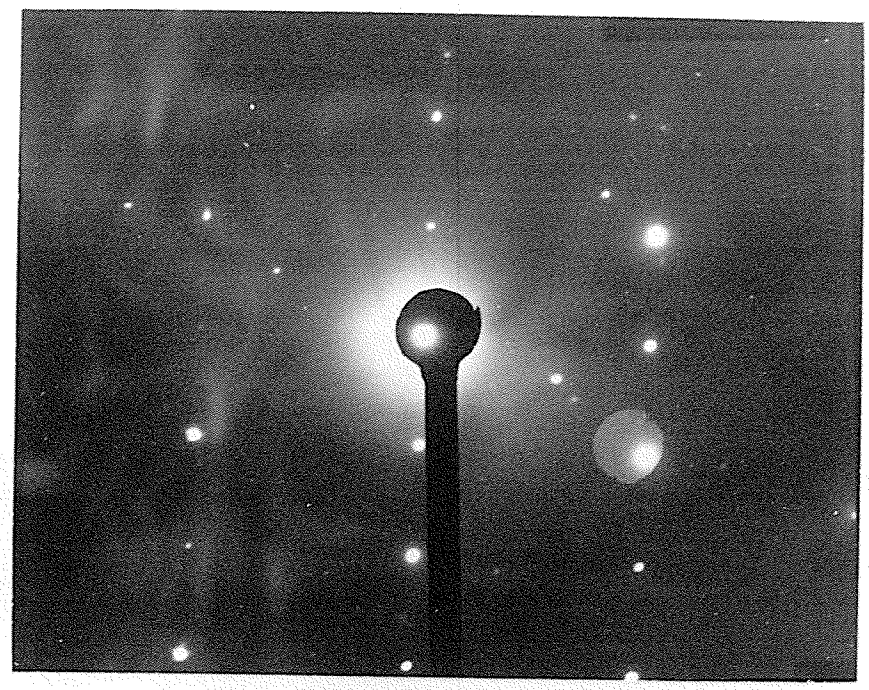

Fig. 118 SADP of Ni_3Nb precipitate. Shows required indexing of (210) which is forbidden by space group Pmmn but allowed by Pma2.

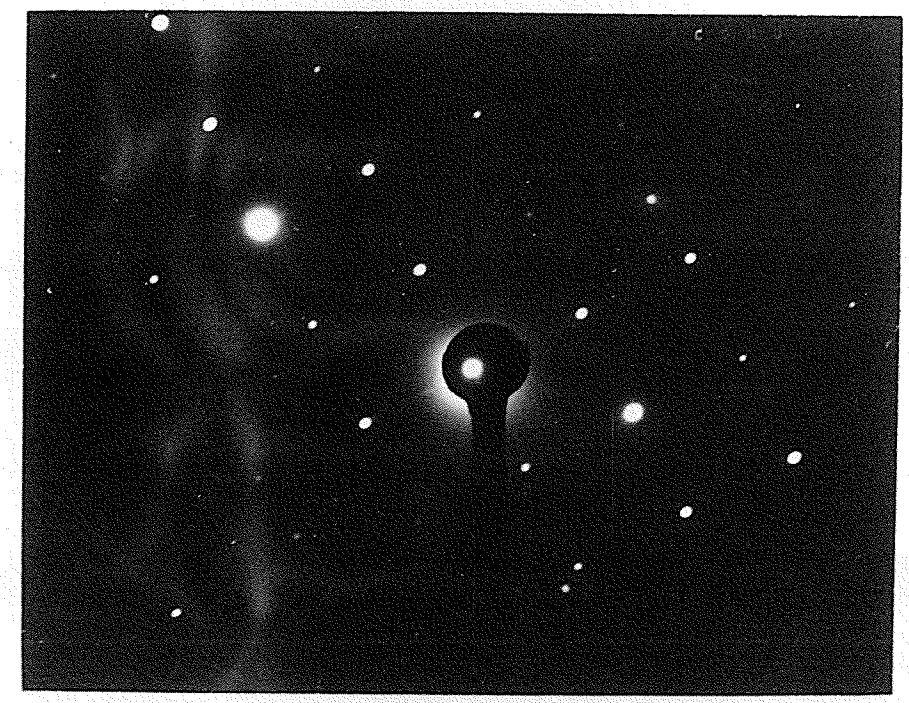

Fig. 119 SADP of Ni_3Nb precipitate. Shows required indexing of (010) which is forbidden by space group Pmmn but allowed by Pma2.

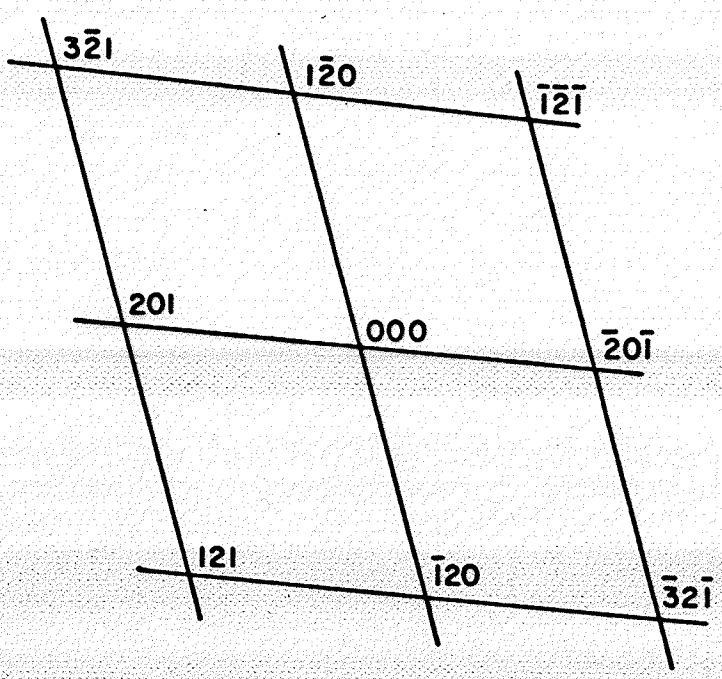
3$\bar{2}$1
1$\bar{2}$0
$\bar{1}\bar{2}\bar{1}$
201
000
$\bar{2}$0$\bar{1}$
121
$\bar{1}$20
$\bar{3}$2$\bar{1}$

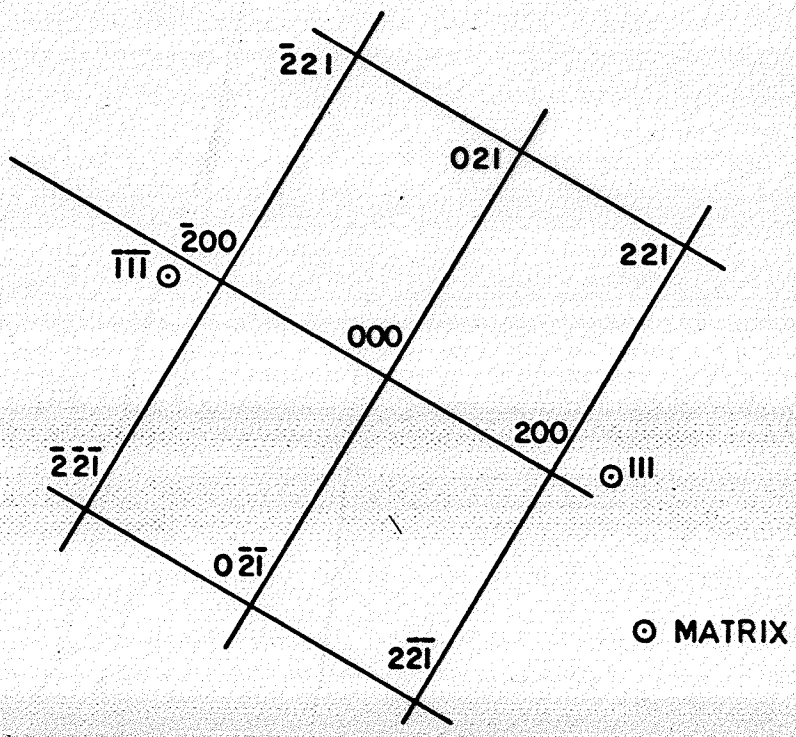
$\bar{2}$21
021
$\bar{2}$00
$\bar{1}\bar{1}\bar{1}$ ⊙
221
000
200
$\bar{2}\bar{2}\bar{1}$
⊙ 111
0$\bar{2}\bar{1}$
2$\bar{2}\bar{1}$
⊙ MATRIX

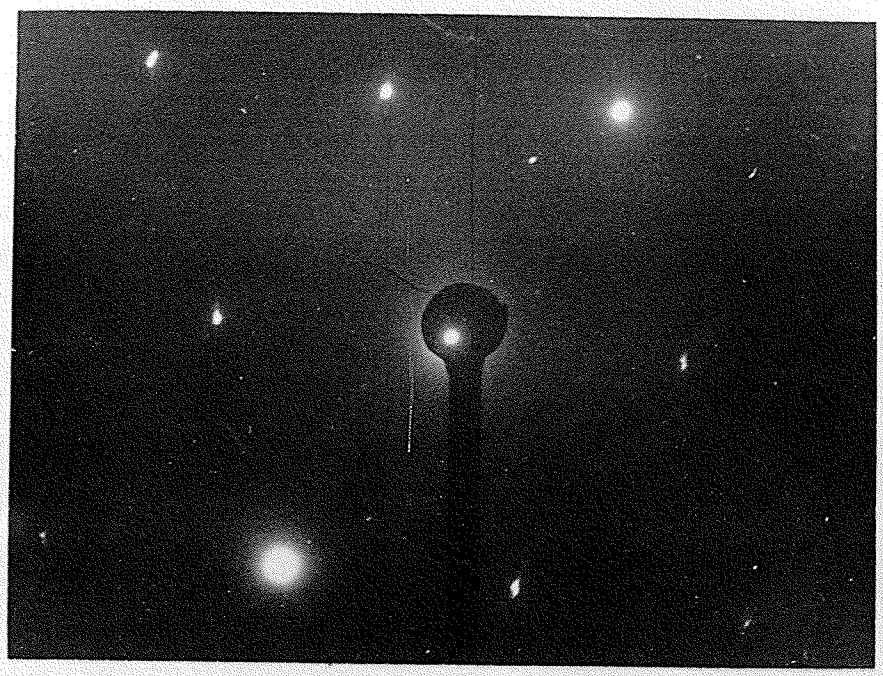

Fig. 120 SADP of Ni_3Nb precipitate. Shows required indexing of (120) which is forbidden by space group Pmmn but allowed by Pma2.

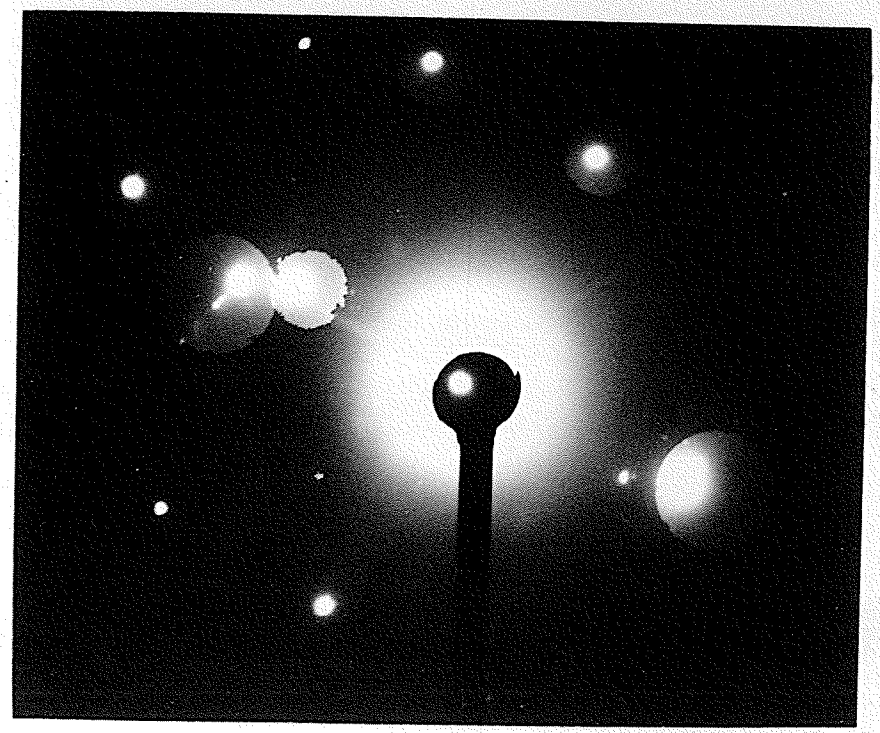

Fig. 121 SADP of Ni_3Nb precipitate. Indexing fits both space group Pmmn and Pma2.

REFERENCES

1 Yearian, J. J. and Moral, F. R., Metals and Alloys, 12, July 1940, p. 54.

2 Decker, D. F. and Dewitt, B. R., Journal of Metals, Feb. 1965, p. 139 - 145.

3 Hess, J. B. and Barret, C. B., Journal of Metals, 4, 1952, p. 645.

4 DeLamotte, E. and Altstetter, C. J., Transaction of AIME, 245, 1969, p. 651.

5 Chung, D. W. and Chaturvedi, M. C., Metal Science Journal, 8, 1974, p. 215 - 221.

6 Pugliese, L. A. and Stroup, J. P., Cobalt, 43, June 1969.

7 Graham, A. H., Transactions of the ASM, 62, 1969.

8 Drapier, J. M., Victour, P., Coutsouradis, D., and Habraken, L., Cobalt, 49, Dec. 1970, p. 171 - 186.

9 Chung, D. W. and Chaturvedi, M. C., Metallography, 8, p. 329 - 336.

10 Chung, D. W. and Chaturvedi, M. C., Metal Science Journal, 6, 1972, p. 134 - 140.

11 Ravindrand, C. and Chaturvedi, M. C., Metallurgical Transactions, 6a, 1975, p. 213 - 217.

12 Cottrell, A. H., Dislocations and Plastic Flow in Crystals, London Oxford University Press, 1953.

13 Friedel, J., Lectures on Dislocations, Gauthier-Villars, 1956.

14 Mackenzie, J. K., thesis, University of Bristol, 1949, referenced in 12.

15 Kelly, A., Strong Solids, London Oxford University Press, 1960.

16 Frank, F. C., Symposium on Plastic Deformation of Crystalline Solids, Office of Technical Services US Dept. of Commerce, 1950, p. 89.

17 Bragg, W. L., Proceedings of the Physics Society, 52, 1940, p. 54.

18 Burgers, J. M., Ibid. (17), p. 23.

19 Hull, D., Introduction to Dislocations, Pergamon Press, New York, 1968.

20 Whelan, M. J., Proceedings of the Royal Society, 249, 1959, p. 114.

21 Howie, A., Direct Observations of Lattice Defects in Crystals, Interscience, New York-London, 1962, p. 283.

22 Howie, A., Proceedings of the European Regional Conference on Electron Microscopy.

23 Swann, P. R., Nutting, J., Journal of the Institute of Metals, 90, 1961, p. 133.

24 Howie, A. and Swann, P. R., Phil. Mag., 6, 1961, p. 1215.

25 McElroy, R. J. and Szkopiah, Z. C., International Metallurgical Reviews, 17, 1975, p. 175 - 202.

26 Swann, P. R., Electron Microscopy and Strength of Crystals, Interscience, Thomas, G. and Washburn, J. (eds.), 1963, p. 131 - 177.

27 Keh, A. and Weissman, Ibid. (26), p. 231.

28 Blewitt, T. H., Eattman, R. R., and Redman, J. K., Applied Physics, 28, 1957, p. 651.

29 Venables, J. A., Deformation Twinning, Metallurgical Society Conferences, 25 Reed-Hill, R. E. et al (eds.), 1963, p. 77 - 110.

30 Westlake, D. G., Deformation Twinning, Ibid. p. 29 - 41.

31 Orowan, E., Dislocations in Metals, AIME, New York, 1954, p. 116.

32 Bell, R. L. and Cahn, R. W., Proceedings of the Royal Society, A239, London, 1957, p. 494 - 521.

33 Fourie, J. J., Weinberge, F., Berwell, F. W. C., Acta Met, 8, 1960, p. 851 - 863.

34 Price, P. B., Proceedings of the Royal Society, A260, 1957, p. 251 - 262.

35 Cabrera, N., Price, P. B., Growth and Perfection of Crystals, Wiley, New York, p. 204.

36 Cottrell, A. H., Bilby, B. A., Phil. Mag., 42, 1951, p. 573.

37 Kelly, A., Nicholson, R. B., Progress in Metal Physics, 10, 1963, p. 151.

38 Christian, J. W., The Theory of Transformation in Metals and Alloys, Pergamon Press, 1965, p. 606.

39 Burke, J., The Kinetics of Phase Transformations in Metals, Pergamon Press, 1965.

40 Martin, J. W., Precipitation Hardening, Pergamon Press, 1968.

41 Kelly, A., Nicholson, R. B., Ibid. (37), p. 154.

42 Martin, J. W., Ibid. (40), p. 21.

43 Nabarro , F. R. N., Proceedings of the Physics Society, 52, 1940, p. 90.

44 Gibbs, J. W., Collected Works, Yale University Press, 1948, p. 105 and p. 252.

45 Burke, J., Ibid. (39), p. 147.

46 Ibid.

47 Volmee, M., Weber, A., Physical Chemistry, 119, 1925, p. 227.

48 Becker, R., Doring, W., Ann. Physics, 29, 1935, p. 719.

49 Kelly, A. Nicholson, R. B., Ibid. (37), p. 178.

50 Vety, J. T., Polmear, J. J., Institute of Metals Journal, 94, 95, p. 41.

51 Ogama, R., Fukutsuks, T., Gagi, Y., Trans of the ISIJ, 12, 1972, p. 410.

52 Krishna-ev, M. R., Le Mag I., Metallography, 2, 1969, p. 253 - 256.

53 Furubayaski, E., Endo, H., Yoshida, H., Material Science and Engineering, 14, 1974, p. 123 - 130.

54 Roberon, J. A., Adair, A. M., Trans of AIME, 245, 1969, p. 1937.

55 Cahn, J. W., Acta Met., 5, 1957, p. 169.

56 Nicholson, R. B., Phase Transformations, ASM, 1968, p. 287.

57 Singhal, L. K., Bhargava S. N., Martin, J. W., Metallography, 5, 1972, p. 31 - 39.

58 Himmel, L. (ed.) Recovery and Recrystallization, 1963, New York.

59 Recrystallization, Textures, and Grain Growth, ASM, Metal Parks, Ohio, 1966.

60 Cahn, R. W., Physical Metallurgy, Amsterdam, 1965, p. 925.

61 McElroy, R. J., Szkopiak, Z. C., Ibid., (25).

62 Reed-Hill, R. E., Physical Metallurgical Principles, D. Van Nostrand Company, Inc., Princeton, New Jersey, 1968.

63 Elroy, R. J., Szkopiak, Z. C., Ibid. (25).

64 Cahn, R. W., Ibid. (60), p. 1148.

65 Cahn, R. W., Ibid. (60), p. 1129.

66 Cahn, R. W., Recrystallization Of Metallic Materials, Haessener, F. Dr. Riederer-Verlaggmbh Stuttgart, (eds), 1970, p. 43 - 80.

67 Hu Hsun, Recovery and Recrystallization of Metals, Himmel (ed), 1963, AIME, p. 311 - 362.

68 Burke, J. E., Turnbull, D., Progress in Metal Physics, 3, 1952, p. 220.

69 Chan, R. W., Proceedings of the Physics Society, 63A, London, 1950, p. 323.

70 Cottrell, A. H., Progress in Metal Physics, 4, 1953, p. 255.

71 Hu, H., Ibid. (67).

72 Hu, H., Textures in Research and Practice, J. Grewen and G. Wassermand (eds), Springer, Berlin, 1969, p. 200.

73 Beck, P. A., Sperry, P. R., Journal of Applied Physics, 21, 1950, p. 150.

74 Hofmann, S., Haessner, F., Recrystallization of Metallic Materials, Ibid. (66), p. 81.

75 Kreye, H., Hornbogen, E., Journal of Material Sciences, 5, 1970, p. 84 - 85.

76 Koster, U., Recrystallization of Metallic Materials, Ibid. (66), p. 215 - 216.

77 Stuwe, H. P., Recrystallization of Metallic Materials, Ibid. (66), p. 21.

78 Zener, G., cited in Smith, C. S., Trans AIME, 175, 1948, p. 15.

79 Ashby, M. F., Harper, J., Lewis, J., Harvard Reprint No. 542, 1967.

80 Kreye, H., Hornbogen, E., Ibid. (75), p. 71.

81 Chung, D. W., Unpublished Data.

82 Powder Diffraction File #17-700, Joint Committee on Powder Diffraction Standards, U.S.A.

83 Troiasia, A. R., Tokich, J. L., Trans AIME, 175, 1948, p. 728.

84 De Lamotte, E., Altstetter, C., Trans AIME, 245, 1969, p. 651.

85 Gaunt, P., Christian, J. W., ACTA Metallurgica, 7, 1959, p. 529.

86 Habraken, L., Journal of the institute of Metals, 87, 1958-59, p. 85.

87 Bollmann, W., ACTA metallurgica, 9, 1961, p. 972.

88 Votava, E., ACTA Metallurgica, 8, 1960, p. 901.

89 Bibring, H. et al., Journal of the Institute of Metals, 87, 1958-59, p. 71.

90 Hess, J. B., Barrett, C. S., Journal of Metals, 87, 1952, p. 645.

91 Houska, C. R. et al., ACTA Metallurgica, 8, 1960, p. 81.

92 Broom, T., Barrett, C. s., ACTA Metallurgica, 1, 1953, p. 305.

93 Nelson, J. O., Alstetter, C. J., Trans of AIME, 230, 1964, p. 1577.

94 Bibring, H., Sebilleau, F., Compt. Rend. 1954, 238, p. 1026.

95 Takeuchi, S., Honma, T., Sce. Rep. Res. Inst. Takoku University Ser. A9, 1957, p. 492.

96 Bilby, B. A., Phil Mag, 44, 1953, p. 247.

97 Basinski, A. S., Christian, J. W., Phil Mag, 44, 1953, p. 791.

98 Seeger, A., Z. Metallk, 44, 1953, p. 247.

99 Graham, A. H., Trans ASM, 62, 1969, p. 930.

100 Graham, A. H., Youngblood, J. L., Met. Trans, 1, 1970, p. 423.

101 Pugliese, L. A., Stroup, J. P., Cobalt, 43, 1963.

102 Sandroch, G. D., Andrews, C. W., NASA Technical Note NASA TND-7051, 1971.

103 Davies, C. K. L., Sator, V., Stevens, R. N., ACTA Met., 21, 1973, p.1343.

104 Venables, J. A., Phil Mag, 7, 1962, p. 42.

105 Malis, M., MSc Thesis, 1971, Dafoe Library, University of Manitoba.

106 Cahn, R. W., Deformation Twinning, Ibid. (29), p. 1 - 28.

107 Cozar, R., Pineau, A., Met. Trans, 4, 1973, p. 47.

108 Kaufman, M., Palty, A. E., Trans of AIME, 221, 1961, p. 1253.

109 Paulions, D. F., Oblak, J. M., Duvall, D. S., Trans of ASM, 62, 1969, p. 611.

110 Kirman, I., Warrington, D. H., Journal of ISI, 205, 1967, p. 1264.

111 Weiner, R. T., Irani, J. J., Trans of ASM, 59, 1966, p. 341.

112 Kirman, I., Journal of ISI, 207, 1969, p. 1612.

113 Kirman, I., Warrington, D. H., Journal of ISI, 99, 1971.

114 Kotval, P. S., Trans of AIME, 242, 1968, p. 1764.

115 Hutchinson, M. M., Metallurgy Report 58, Dept. of Supply Australian Defence Scientific Service Aeronautical Research Laboratories, 1966.

116 Hirsch, P. et al., Electron Microscopy of Thin Crystals, Butterworth, London, 1965.

117 Andrews, K. W. et al., Interpretation of Electron Diffraction Patterns, Hilger, LTD., 1971.

118 Reed-Hill, R. E. Ibid. (62), p. 175.

119 Hull, D., Ibid. (19), p. 21.

120 Read, W. T., Jr., Dislocations in Crystals, McGraw-Hill, New York, 1953, p. 157.

121 Honeycombe, R. W. K., The Deformation of Metals, Edward Arnold Ltd., 1968, p. 202 - 203.

122 Hull, D., Ibid. (19), p. 89.

123 Burke, J., Ibid. (39), p. 102.

124 Reed-Hill, R. E., Ibid. (62), p. 184.

125 Ibid., p. 1 - 5.

126 Shewman, P. G., Transformation in Metals, McGraw-Hill, New York, 1969, p. 107.

127 Hornbogen, E., Praktische metallographie, Special Issue 2, 1970, p. 68 - 79.

128 Hansen, M., Constitution of Binary Diagram, 2nd ed., McGraw-Hill, 1958.

129 ASM, Metals Handbook, 8, 1973, ASM, Ohio, U.S.A.